



Christof Birgel

Measurement of the Burst Behavior of High-Speed Carbon Fiber Rotors with Respect to Safety Containment Design

Master's Thesis

to achieve the university degree of
Diplom-Ingenieur

Master's degree program: Mechanical Engineering

Submitted to

Graz University of Technology

Supervisors:

Dipl.-Ing. Dr.techn. Armin Buchroithner

Ass.Prof. Priv.-Doz. Dipl.-Ing. Dr.techn. Hannes Wegleiter

Institute of Electrical Measurement and Sensor Systems

Graz, December 2019

Affidavit

I declare that I have authored this thesis independently, that I have not used other than the declared sources/resources, and that I have explicitly indicated all material, which has been quoted either literally or by content from the sources used. The text document uploaded to TUGRAZ-online is identical to the present master's thesis.

Date

Signature

Abstract

This work deals with empirical and simulative investigation of rotor damage and burst protection containments of fast-spinning flywheel energy storage systems.

As part of the *FlyGrid* project at the *Graz University of Technology*, a fast spinning flywheel concept will be implemented in a high-speed charging station for electric vehicles. In order to increase the specific energy density of the storage, a carbon fiber composite rotor is used. Due to an intelligent stress optimization of the composite structure, they are able to resist higher centrifugal loads at extreme rotational speeds.

As consequence of a damaged flywheel accumulator, the worst-case scenario leads to an abrupt release of the entire stored energy. Depending on the design and material of the rotor, different fracture behavior can be observed. This bursting behavior has to be investigated in order to determine the forces acting on the housing. If the surrounding containment does not resist the occurring loads, the escaping medium holds a potential hazard.

The aim of this work is to develop a better understanding and guidelines for safe housing design of fast-rotating flywheels. Since there is only little published literature on this subject, empirical rotor bursts were systematically carried out. For this purpose, a specially manufactured test rig was used and adapted to the different requirements and test conditions.

During the first series of tests, rotors made of steel and cast iron were burst at high speeds. These materials have the advantage of well-known isotropic properties and allow repeatable results with defined fragment dynamics. As the released energy has to be absorbed by the housing, a variation of containment rings made of steel, stainless steel and aluminum were applied. By evaluating the most important measurement data, an energy balance for each test was developed. Concerning the rotor, the burst-speed and the fragment behavior were observed and in the terms of the containment, the deformation and friction-related heat input were recorded. The results of these tests provided material data and failure-modes of the investigated housing materials for an adequate finite element modelling. This will subsequently serve as the basis for the simulation of various safety concepts for a Carbon Fiber Reinforced Polymer (CFRP) rotor application.

The last test series relied on failure criteria of carbon fiber rotors. Particular attention was paid to the manufacturing process for the targeted *FlyGrid* flywheel. For this purpose, downscaled rotors were manufactured of circular wound, pre-impregnated carbon fiber *PrePregs*. First dynamic burst tests of specially notched structures made it possible to investigate process-dependent sources of defects, which in turn should lead to improvements of the CFRP manufacturing.

Due to the potential and the increasing use of fast-rotating flywheels, future CFRP burst tests are unavoidable. These tests would make an essential contribution to the understanding of failure scenarios and the resulting impact on the housing. Furthermore, published results could ensure better assessment for safety-relevant measures, which leads to a more attractive application of this energy storage concept.

Kurzfassung

Diese Arbeit beschäftigt sich mit der empirischen und simulationsgestützten Untersuchungen von Rotorschäden und Berstschutzgehäusen schnelldrehender Schwungradspeicher.

Im Zuge des *FlyGrid* Projektes an der *Technischen Universität in Graz* wird ein schnelldrehender Schwungradenergiespeicher in eine Schnellladestation für elektrische Fahrzeuge implementiert. Um die spezifische Energiedichte des Speichers zu steigern wird ein Kohlefaserverbund-Rotor eingesetzt, welcher durch eine intelligente Spannungsoptimierung enormen Fliehkraft-Belastungen bei hohen Drehzahlen standhält.

Im ungünstigsten Fall wird beim Schaden eines solchen Schwungradspeichers die gesamte gespeicherte Energie schlagartig frei. Abhängig von Aufbau und Material des Rotors, können verschiedene Bruchverhalten beobachtet werden. Dieses Berstverhalten gilt es zu untersuchen um die auf das Gehäuse einwirkenden Kräfte zu bestimmen. Denn hält die Einhausung dieser Beanspruchung nicht stand, birgt das austretende Medium ein Gefahrenpotential.

Ziel dieser Arbeit ist es eine Basis für eine sichere Gehäuseauslegung von schnelldrehenden Schwungradspeichern zu entwickeln. Da es diesbezüglich nur wenig veröffentlichte Literatur gibt, wurden systematisch empirische Rotor-Berstversuche durchgeführt. Hierfür kommt ein eigens angefertigter Prüfstand zum Einsatz welcher den unterschiedlichsten Prüfungsbedingungen angepasst wurde.

Im Zuge von ersten Testreihen wurden Rotoren aus Stahl und Grauguss bei hohen Drehzahlen geborsten. Diese Materialien weisen bekannte isotrope Eigenschaften auf und ermöglichen reproduzierbare Versuche mit einer definierten Bruchstückdynamik. Die freiwerdende Energie muss vom Gehäuse aufgenommen werden, wobei Gehäuseeringausführungen aus Stahl, rostfreiem Stahl und Aluminium zum Einsatz kamen. Durch die Auswertung der wichtigsten Messdaten konnte für jeden Versuch eine Energiebilanz erstellt werden. Dabei wurde rotorseitig die Berstdrehzahl und das Bruchstückverhalten und gehäuseseitig die Verformung und der reibungsbedingte Wärmeeintrag erfasst. Die Ergebnisse dieser Versuche lieferten Materialbedatungen und Fehlerkriterien der untersuchten Gehäusematerialien für eine adäquate FEM Modellierung. Diese soll in weiterer Folge als Basis für die Simulation verschiedener Sicherheitskonzepte für eine CFK-Rotor-Anwendung fungieren.

Die letzte Testreihe bezog sich auf Versagenskriterien von Kohlefaser Rotoren. Besonderes Augenmerk lag auf dem Fertigungsverfahren für das geplante *FlyGrid* Schwungrad. Hierfür wurden kleinskalierte Rotoren aus zirkular gewickelten, vorimprägnierten Kohlefaser *PrePregs* hergestellt. Erste dynamische Berstversuche von speziell gekerbten Strukturen ermöglichten die Untersuchen von Prozess abhängigen Fehlerquellen, welche in weiterer Folge zur Verbesserung der CFK-Verarbeitung führen sollen.

Durch das Potential und den immer häufigeren Einsatz schnelldrehender Schwungräder sind CFK-Berstuntersuchungen unumgänglich. Diese leisten einen wesentlichen Beitrag zum Verständnis von Versagensszenarien und die daraus resultieren Einwirkungen auf das Gehäuse. Veröffentlichte Ergebnisse können somit in Zukunft dafür sorgen sicherheitsrelevante Maßnahmen besser beurteilen zu können und eine Nutzung dieses Energiespeicherkonzeptes attraktiver zu gestalten.

Table of Contents

1	Introduction and Motivation	1
1.1	Basics of Flywheel Energy Storage Systems	1
1.2	Housing of Flywheel Energy Storage Systems	2
1.3	Spin Testing as a Strategic Development Tool [1]	3
2	The <i>FlyGrid</i> Project	5
2.1	Introduction	5
2.2	The <i>FlyGrid</i> Rotor	5
2.2.1	CFRP Rotor Manufacturing (<i>FlyGrid</i>)	6
2.2.2	CFRP Rotor Assembly (<i>FlyGrid</i>)	7
3	Theory of CFRP Rotor Failure	9
3.1	Rotor Crash	9
3.2	Rotor Burst	9
3.2.1	Fracture Modes of a Translaminar Isentropic CFRP Rotor	10
3.2.2	Failure Modes of a Unidirectional CFRP	10
3.2.3	Failure Initiation	12
4	Theory of the CFRP Rotor Burst Containment	14
4.1	General Impact on the Containment in Case of a CFRP Rotor Burst	14
4.2	Containment Loads occurring in the Event of Rotor Damage	15
4.3	Analytical Calculation Methods in the Case of a Particle Impact [13]	15
4.4	Containment Concepts for CFRP Rotor Flywheel Systems	18
5	Systematic Rotor Burst Testing	20
5.1	Test Rig Design for Steel Rotor Burst Tests [1]	20
5.2	Introduction of Steel Rotor Flywheel Systems	21
5.3	Down-Scaled Burst Rotor Design	23
5.3.1	Variation of the Impact Energy of Milled Burst Rotor	23
5.3.2	Variation of the Cast Iron Handwheel Impact Energy	26
5.4	Performance of the Previous Burst Tests [1]	27
6	Preparation of the Empirical CFRP Rotor Burst Tests	31
6.1	Test Rig Layout for the CFRP Rotor Burst Tests	31
6.1.1	Test Rig Adaptions	32
6.1.2	System Limitations	32
6.2	Implemented Sensors	33
6.2.1	Rotational Speed	34
6.2.2	Vacuum Pressure	34
6.2.3	Acceleration	34
6.2.4	Temperature	35

6.2.5	Particle Impact Pressure	35
6.3	Down-Scaled CFRP Burst Rotor	40
6.3.1	Manufacturing Process and Stress Distribution of the Basic CFRP Rotor Structure.....	40
6.3.2	Radially Notched CFRP Burst Rotor	43
6.3.3	Circularly Notched CFRP Burst Rotor	44
6.3.4	Circularly and Radially Notched CFRP Rotor	46
7	Results	47
7.1	Results of the Empirical Steel Rotor Burst Tests	47
7.2	Results of the Analytical Calculation Method for Steel Burst Containments	54
7.3	Simulation Results of the Steel Rotor Burst Containments	56
7.3.1	<i>Johnson Cook</i> Results	56
7.3.2	Shear Failure Results.....	58
7.4	Simulation Results of the Cast Iron Handwheel Burst Behavior	60
7.5	Results of the Empirical CFRP Burst Tests.....	62
7.5.1	Results of the Radially Notched CFRP Burst Rotor	63
7.5.2	Results of the Circularly Notched CFRP Burst Rotor	66
7.5.3	Results of the Circularly and Radially Notched CFRP Burst Rotor	67
8	Summary and Outlook	68
9	Bibliography	69

List of Illustrations

Figure 1: System layout of a non-integrated electromechanical Flywheel Energy Storage System [2]	1
Figure 2: Eight most relevant aspects of FESS housing /containment design [1].....	2
Figure 3: Impression of a FESS damage incident, 10.06.2015, Poway, San Diego, USA - Quantum Energy Storage Corporation [3]	3
Figure 4: Projected rotor design of the FlyGrid prototype.....	5
Figure 5: Manufacturing steps of the CFRP Rings.....	6
Figure 6: Two main stages of the Press fitting procedure	7
Figure 7: Used equations and assumptions for the analytic strength calculation [9]	7
Figure 8: Showcase of a superposed stress curve in a downsized press fitted CFRP ring	8
Figure 9: Dropped and crashed rotor from Boeing [10]	9
Figure 10: Delamination, caused by an over speed test, ETH Zürich 1996 [11]	9
Figure 11: Crack propagation path and stress-direction [12].....	10
Figure 12: Failure of a unidirectional layer, because of σ_{II}^+ Strain [8]	10
Figure 13: Over speed Tests at 1400 m/s outer tangential speed of the rotor [10].....	11
Figure 14: Break due to transversal tensile stress [8].....	11
Figure 15: Break due to transversal compression [8]	11
Figure 16: Break due to transversal longitudinal shear [8]	12
Figure 17: Break due to transverse transverse shear [8]	12
Figure 18: Impact variation a) Particle impact, b) Fragments with intact structure, c) Unwinding processes with different direction of rotation, d) Rotor Crash by contact of the intact rotor with the containment	14
Figure 19: Particle movement (left) and the impact pressure depending on the containment gap (right) [13].....	17
Figure 20: Generated particle-stream (orange)	18
Figure 21: Comparison of all three models [13]	18
Figure 22: Schematic illustration of a rotating liner	19
Figure 23: Schematic idea of a particle guidance [15]	19
Figure 24: Cross section of the burst test rig including measurement technology [1].....	20
Figure 25: Test-Rig with the major components including the periphery. The control desk (left) can be moved away from the rig when burst tests are conducted. [1]	21
Figure 26: Different flywheel-shapes with the linked Shape-factors [17]	22
Figure 27: Lockheed Martin Burst-Flywheel [32]	22
Figure 28: Milled flywheel structure.....	23
Figure 29: Gray cast iron hand wheel	23
Figure 30: Volume element of a solid rotating disc [4].....	24
Figure 31: Illustrated stress situation in the notched cross section of the milled flywheel [4] (left), Burst fragments and the remaining hub of the milled flywheel (right).....	25
Figure 32: Reassembled cast iron hand wheel fractures after a burst test (left), Different notch-depth and the influenced burst speed (right)	26
Figure 33: Observed abrasion marks at the outer surface.....	26
Figure 34: Samples of cast iron handwheel martial prepared for a notch bar test.....	27
Figure 35: Documentation and reconstruction [1]	28
Figure 36: 3D scanning of burst containments (left) including results before (middle) and after (right) the burst [1].....	28

Figure 37: Survey of the containment deformation [1]	29
Figure 38: Determination of plastic deformation work of the burst containment [1]	29
Figure 39: Temperature increase after the rotor burst (left), Distribution of 15 temperature sensors at the containment surface [1]	30
Figure 40: Cross-section of the Test Rig with the CFRP rotor burst adaptations (rotation speed restrictions in brackets)	31
Figure 41: Sensor attachments of the system	33
Figure 42: Schematic function of a tube pressure gauge [19]	34
Figure 43: Three different Particle Pressure Sensors: Design and Function	36
Figure 44: Mounted strain gauges at the single bending beam load cell (left) and the disc load cell (right).	37
Figure 45: Curve of the diagonal voltage depending on R_x ; a) Circuit, b) Characteristic [24]	38
Figure 46: Diagonal voltage U_d for different bridge arrangements. The unmarked resistors have the value R_0 ; those marked with + have the value $R_0 + \Delta R$ and those marked with - have the value $R_0 - \Delta R$ [24]	39
Figure 47: Manufacturing steps and dimensions of the unnotched burst rotor	40
Figure 48: Calculated thermal radial residual stresses of the CFRP burst rotor	41
Figure 49: Cured and turned CFRP burst rotor	41
Figure 50: Calculated mechanical and thermal superimposed radial stresses of the CFRP burst rotor	42
Figure 51: Geometry of the radially notched rotor design	43
Figure 52: Evaluated radial stresses at 17.000 rpm and a notch depth diameter of 60 mm	44
Figure 53: Geometry of the circularly notched rotor	45
Figure 54: Evaluated radial stresses at 28,000 rpm with a notch diameter ϕ_k of 100 mm and a remaining bar height of 10 mm	45
Figure 55: Geometry of the circularly and radially notched rotor	46
Figure 56: Variation overview classified by the test series 1-13 a) and 14 -22 b)	47
Figure 57: Clamping situation used for the first 13 samples	48
Figure 58: Overview of the measured deformation Energy (left) and two cracked samples (right)	48
Figure 59: Average energy balance based on the first 13 intact containment samples	50
Figure 60: Improved clamping design used for the samples 16 to 24	51
Figure 61: Energy balances of the tested containments No. 14 - 22 compared to 100% of kinetic input of the rotor	53
Figure 62: Radial and tangential velocity at the fragment impact	54
Figure 63: Deformation of the containment and the simplified distribution of the radial speed	54
Figure 64: Schematic influence of high strain rates and rised temperatures	56
Figure 65: Reproduction of a burst containment by simulation with a Johnson Cook failure model	58
Figure 66: Implemented Stress Strain Curve of Aluminum	58
Figure 67: Reconstruction of a completely destroyed containment by implementing a shear failure	59
Figure 68: Simulation process of a cast iron hand wheel burst behavior (ABAQUS)	60
Figure 69: Result of the simulation with the plastic strain behavior of GJS 700 and a plastic strain fail at 0.008 compared to observed fragment sectors	61
Figure 70: Energy ratio of the fragments depending on the released segment size (left), Geometry of the cirkular ring (right)	61
Figure 71: Thermal residual cracks (left) and the resulting burst appearance (right)	63
Figure 72: Close-up of the wavy carbon fiber structure (One fracture surface of the CFRP burst rotor #02)	64

Figure 73: Schematic influence of the preload and the winding diameter on buckling appearance 65
Figure 74: Circular crack on the groove bottom..... 66
Figure 75: Rotor damage due to released circumferential material (left) and remaining debris after the test (right)..... 66
Figure 76: Destroyed rotor structure (left), and the remaining fragments in the burst chamber (right)... 67
Figure 77: Conical shape of the fracture surface (red) 67

1 Introduction and Motivation

1.1 Basics of Flywheel Energy Storage Systems

The increasing need for electric power and the consumer demand for quickly available large amounts of energy (e.g. fast charging of e-cars) presents us with different challenges. In addition to the development and research of new energy sources, it is also necessary to improve distribution and storage. One approach to realize short-term storage is the Flywheel Energy Storage System (FESS). Compared to conventional chemical energy storage, like batteries, a FESS can realize higher energy delivery rates without chemical aging, and significantly higher cycle life [1]. One typical layout of a FESS is illustrated in Figure 1.

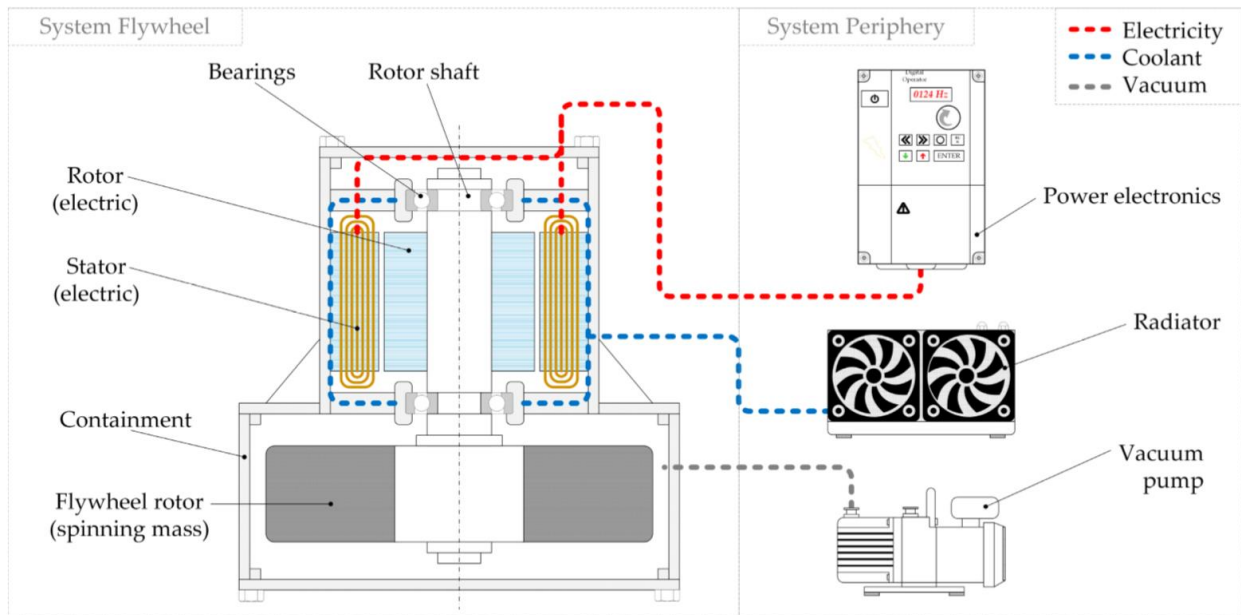


Figure 1: System layout of a non-integrated electromechanical Flywheel Energy Storage System [2]

The principle is based on a spinning mass, where the stored kinetic energy E_{kin} is a function of its moment of inertia I and the rotor speed squared ω^2 .

$$E_{kin} = \frac{I * \omega^2}{2} \quad (1)$$

To increase the energy density and to optimize the packaging of such systems, rotors are operated at ever increasing rotational speeds. These high-speed applications demand extremely high material strength of the rotor to resist the occurring centrifugal stresses. This circumstance leads to the use of Carbon Fiber Reinforced Polymers (CFRP), or other high-strength composites as rotor materials.

1.2 Housing of Flywheel Energy Storage Systems

The design of the housing for a Flywheel Energy Storage System (FESS) has three main tasks. It acts as an interface between the rotating parts and the stationary environment, it provides the air tightness for a vacuum atmosphere and mostly relevant for this investigation, it protects the surroundings against rupture of rotor debris during a possible failure.

Figure 2 shows the eight most relevant aspects of FESS housing design. Besides the aspect of safety (which always needs to be attributed with highest priority), image (appearance) and cost, the FESS housing design must be carried out considering the following criteria.

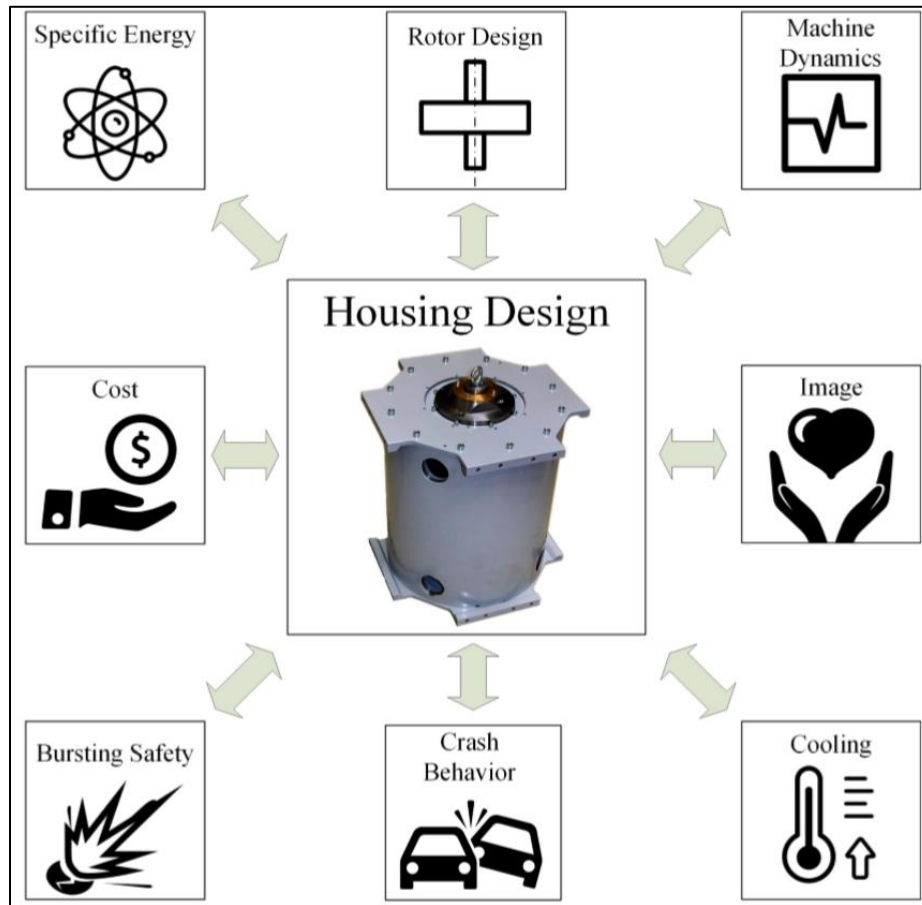


Figure 2: Eight most relevant aspects of FESS housing /containment design [1]

- **Lightweight:** The high specific (kinetic) energy of the FESS-rotor is reduced to a fraction at system level, mainly due to the high weight of the housing.
- **Desired machine dynamics:** Positive influence on rotor dynamics and acoustics due to housing structure and material properties is required (e.g., specific stiffness and damping).
- **Suitability for cooling system:** A proper cooling circuit for the electric motor-generator and the bearing system must be easily integrated in the housing.
- **Low cost:** Low-cost materials and efficient manufacturing processes (suitable for serial production) must be selected for the burst containment [1].

As mentioned, it is absolutely imperative to design safe containments for FESS. In the worst case, so called rotor burst, the entire stored kinetic energy is released within milliseconds, in the form of fragments, particles or delaminated layers of the spinning structure, moving at speeds above 1000 m/s. The extent of damage can be presumed based on Figure 3, which shows an “explosion” of a 560 MJ flywheel of the *Quantum Energy Storage* power plant in San Diego, USA [3].



Figure 3: Impression of a FESS damage incident, 10.06.2015, Poway, San Diego, USA - Quantum Energy Storage Corporation [3]

1.3 Spin Testing as a Strategic Development Tool [1]

To design appropriate containment structures, it is essential to understand the burst mechanisms of the rotor. The number of published results of burst tests of FESS is not sufficient enough to allow a statistically significant qualitative analysis. Furthermore, the requirements and ambient conditions for the different tests vary significantly, making it impossible to derive generally valid, proper design guidelines. Some companies offer industrialized spin rigs / spin pits for sale, or they offer spin services for rent. However, despite the seemingly large offer of test sites and equipment, the available facilities do not serve the purpose as a strategic development tool for various reasons:

- **Availability:** Time slots for spin tests need to be booked in advance. Availability highly depends on order situation of spin testing company.
- **Cost:** Depending on rotor size and desired data, a single spin test costs in the range of 1000 ~ 5000 € (Price depends on rotor’s size, material, burst speed and required preconditioning (balancing, heating etc.) and may well exceed 5000 € in some cases. Information is based on personal experience with European companies offering spin tests.). The purchase price of the Schenck ROTEC “Centrio 100” spin pit, for instance, is 550,000 €.
- **Flexibility:** In order to gain deep scientific insight into the complex rotor-housing system a highly customizable test rig design regarding measurement equipment and vacuum feedthrough hardware is required.

- **Balancing-Quality:** Most commercially available spin pits require an extremely accurate balancing of test rotors and do not allow burst testing of cheap rotors with low balancing quality.

As a consequence, in FESS rotor development spin services are usually only used for a single design validation and not as a strategic development tool during the entire design process. On the other hand, a statistically significant number of tests would be ideal to validate numerical models and fully exploit the energy storage potential of the rotor material. This is why an own low-cost test rig for spin testing was designed in previous work by [4], [5] and [6].

The goal of the empirical investigation lies in the determination of an analytic relation between the kinetic energy of the rotor (or rotor fragments) and the energy absorption ability of the burst containment/housing while retaining structural integrity, as well as validation of numerical models in the long run. Ultimately, the developed methods will allow the design of safe, yet light-weight housing for high-speed rotating machines.

2 The FlyGrid Project

2.1 Introduction

The *FlyGrid* Project, led by the *Institute of Electrical Measurement and Sensor Systems* at the *Technical University of Graz*, is developing a “fast spinning” Flywheel Energy Storage System. The prototype of the energy storage unit will be implemented in a fast charging system for electric vehicles and will enable peak shaving to stabilize the power grid.

Flywheel energy storage systems generally follow either of two possible design strategies:

- a) low-speed flywheel systems that operate under 10.000 rpm,
- b) high-speed variants that can approach 100.000 rpm.

The maximum speed limit, at which the flywheel rotor can operate, is determined by the tensile strength of the material it is made from. As the rpms increase and hoop stresses within the rotor exceed the tensile strength limits of the material, the structure will break apart. Early cast iron Flywheels (e.g.) used on early steam engines, were far too weak for the high rpm use. Better performing alloys made of magnesium, titanium, aluminum and steel were developed offering up to 20 times more tensile strength. Composites like glass fiber and carbon fiber reinforced polymers (CFRP) pushed flywheel tensile strength even further, easily doubling capability of high performance metals [7].

Due to the mechanical advantages of reinforced polymers, the projected *FlyGrid* rotor will be made of circular wound CFRP.

2.2 The FlyGrid Rotor

The possible failure modes and safety related issues of high-speed rotors made of CFRP are highly dependent on the design and manufacturing process. Therefore, it is important to know that composites materials reinforced by continuous fibers are strongly anisotropic. In case of a unidirectional CFRP, the fibers are embedded in only one direction and reach, depending on the volume ratio of used polymer to carbon fiber, a tensile strength of up to 3,000 MPa. On the other hand, the obtained mechanical stress limits in matrix strength dominated directions are very low (approximately tensile strength values of 60 MPa). Exceeding these values has to be prevented by an intelligent manufacturing design.

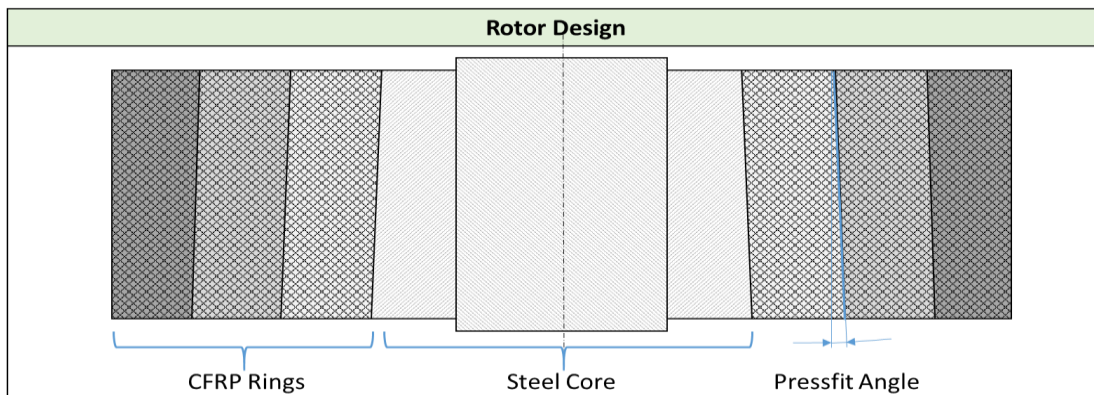


Figure 4: Projected rotor design of the FlyGrid prototype

The *FlyGrid* rotor consists out of two main parts. The inner shaft made of steel (Steel Core) and a number of outer pressfitted CFRP rings, as illustrated at Figure 4.

2.2.1 CFRP Rotor Manufacturing (*FlyGird*)

The wall thickness of the CFRP rings are limited because of thermal reactions, which take place during the curing process and to the transversal isentropic shrinking behavior of the wound composite structure. Due to the thermal reactions, a too thick ring may exceed the critical temperature by an internal exothermic process and burn the polymer core. Furthermore, temperature profiles, which lead to thermal residual stresses, are related to the wall thickness. This effect is superimposed by transversal isotropic thermal shrinking and expansion behavior of the composite. Due to the not yet completely formed matrix strength during the hardening process at high temperatures, these residual stresses can lead to pre-damage of the laminate [8].

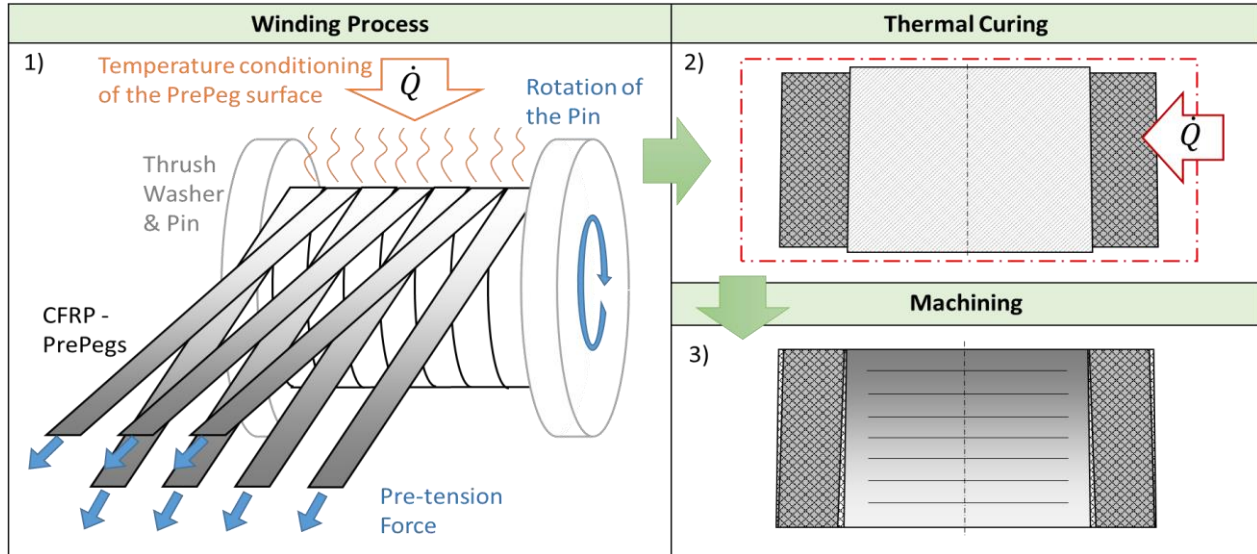


Figure 5: Manufacturing steps of the CFRP Rings

- 1) The CFRP rings are made out of several parallel 12.5 mm wide circularly wound *PrePregs*. The used *PrePregs* are flexible bands of 0.2 mm strong unidirectional composites in an uncured stage. As shown in Figure 5, this band-shaped semi-finished material is guided side by side and rolled on a cylindrical pin. To avoid air inclusions between the layers, the *PrePreg* surface has to be heated up properly and the strips need to be kept at tension. The axial dimension is limited to a left and a right thrush washer.
- 2) After the winding process, the whole structure including the steel pin is tempered to harden the polymeric matrix. The thermal expansion of the composite and the thermal shrinking of the steel during final cool down should create a sufficient gap between the different materials to separate the parts. To compensate further deviations of surface qualities and form-tolerances, the pin has a slightly angled conical shape, which ensures the removal of the core without damaging the CFRP ring.
- 3) The next manufacturing step is the machining procedure. The surfaces for the later press fitted concentric CFRP rings has to be precisely turned to guarantee a sufficient accuracy of the fitted parts.

2.2.2 CFRP Rotor Assembly (FlyGrid)

As mentioned before, the different rings are connected by a press fit, which is illustrated in Figure 6. On the one hand, this fitting process provides the connection of the different layers and on the other hand, it allows a pre-tensioned radial pressure profile, as it is demonstrated in Figure 8. To reduce friction during the fitting process, the interference surfaces are covered with liquid cold curing resin. The fitting pressure has to be obtained until the curing time of this resin is over.

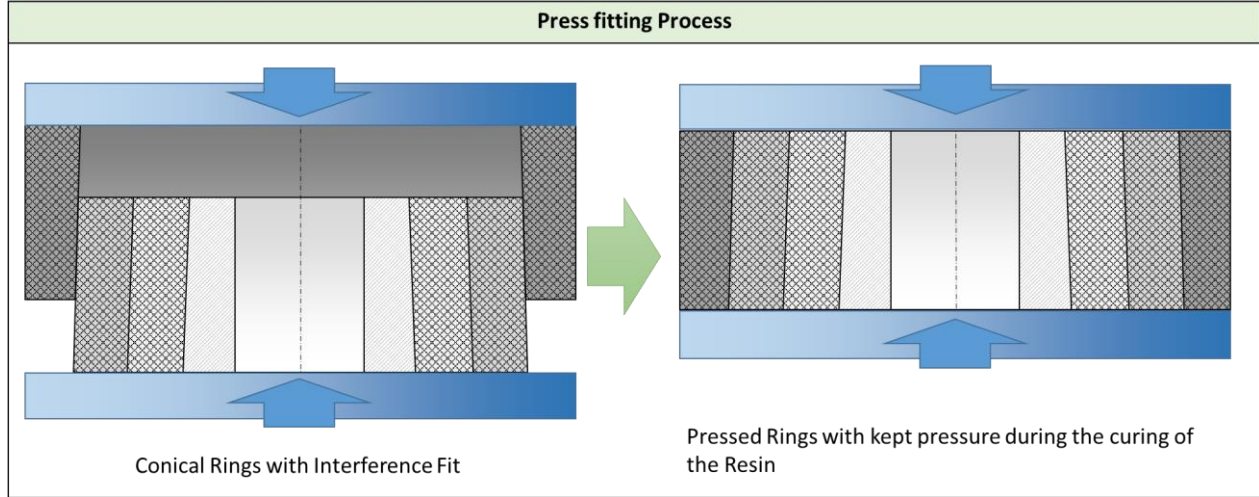


Figure 6: Two main stages of the Press fitting procedure

Due to the centrifugal forces, depending on the rotation speed, the occurring diameter-displacement results in positive radial stresses. These stresses have to be obtained by the relatively “weak” polymer matrix of the composite. To avoid a collapse of the structure, the press-fit design must provide a permanent radial pressure (negative stress), also at a high rotational speed.

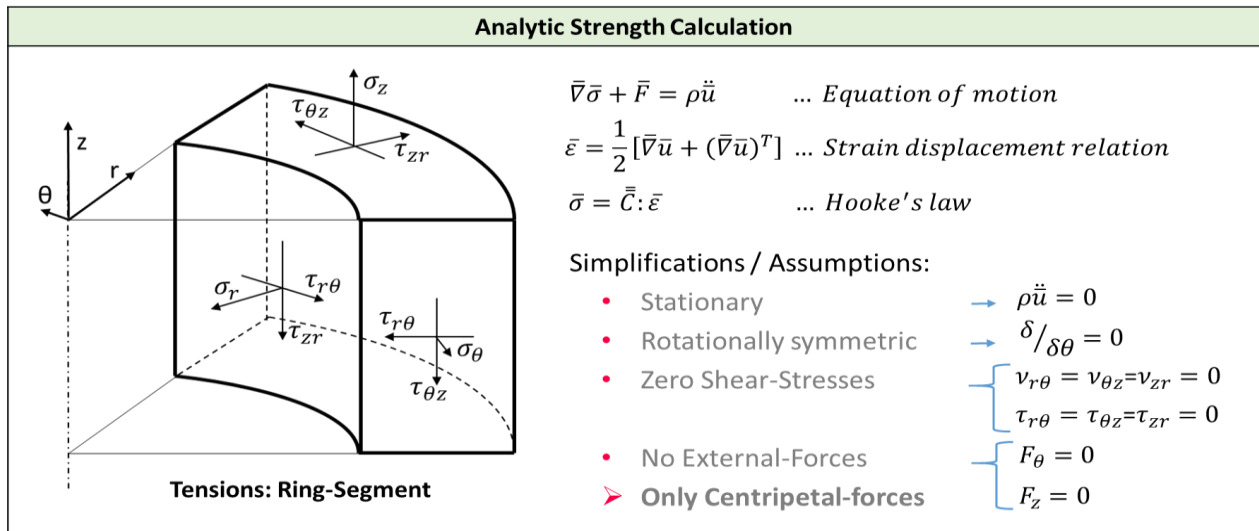


Figure 7: Used equations and assumptions for the analytic strength calculation [9]

As shown in Figure 7, the three main equations are the equation of motion (behavior of motion as a function of time), the strain displacement relation (deformation in terms of relative displacement of particles in the structure excluding rigid-body motion) and the Hooke’s law (describing the proportional

relation between force and extension). Due to the listed assumptions and simplifications expressed in cylindrical coordinates, the solvable equations lead to a stress profile depending rotation speed [9].

If the radially press fit pressure superimposes these stresses, the radial tensile stresses should be reduced, or avoided.

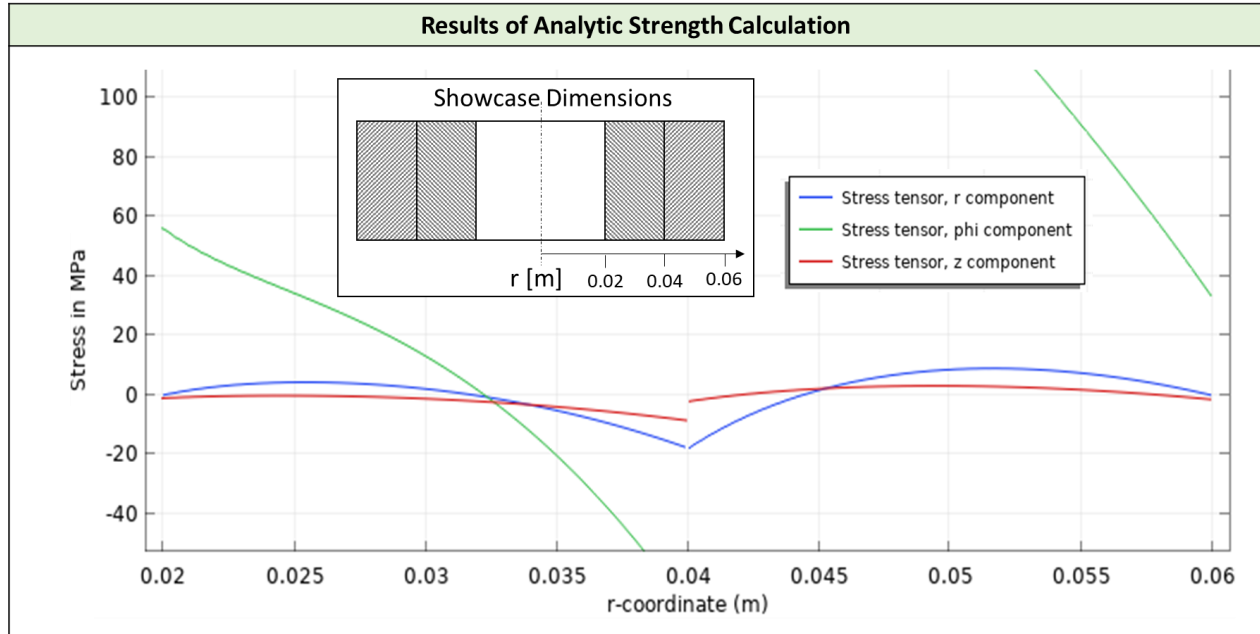


Figure 8: Showcase of a superposed stress curve in a downsized press fitted CFRP ring

The positive effect is illustrated in an example of a two-ring press-fitted spinning sample and follows the previous mentioned simplifications for a transversal isotropic material behavior and the resulting strength calculations. Figure 8 demonstrates the effect of an interference fit. The stress tensor in radial direction (blue curve) is elevated, due to centrifugal forces and lowered because of the press fit pressure.

3 Theory of CFRP Rotor Failure

In general, there are two types of rotor failure modes, *Rotor Crash* and *Rotor Burst*.

3.1 Rotor Crash

In the event of a rotor crash, the spinning rotor touches the inside of the housing. At the time of failure, the rotating structure may still be intact. This situation can be caused, for example, by a bearing breakdown or a collapsing shaft. If emergency operating systems, like secondary bearings also fail, the contact between the outer surface of the rotor and the inner surface of the containment can cause considerable damage. So called “Drop down tests”, where the shaft is released from its bearings at high speeds, are designed to evaluate these scenarios. Figure 9 shows a drop down test of a downscaled prototype of a *Boeing Phantom Works FESS Rotor*, which was released at 41,000 rpm [10]. The damage shows a fine particle abrasion of the outer carbon fiber rim. Due to high “impact time” to slow down the rotating mass, the extent of damage is not that serious. However, the housing must be able to avoid any kind of environment pollution by the fine carbon fiber particles.



Figure 9: Dropped and crashed rotor from Boeing [10]

3.2 Rotor Burst

This means a failure of the entire rotor structure by different fracture modes. These modes strongly depend on the material behavior and the manufacturing process. Figure 10 shows a possible delamination failure, due to interlaminar crack propagation.

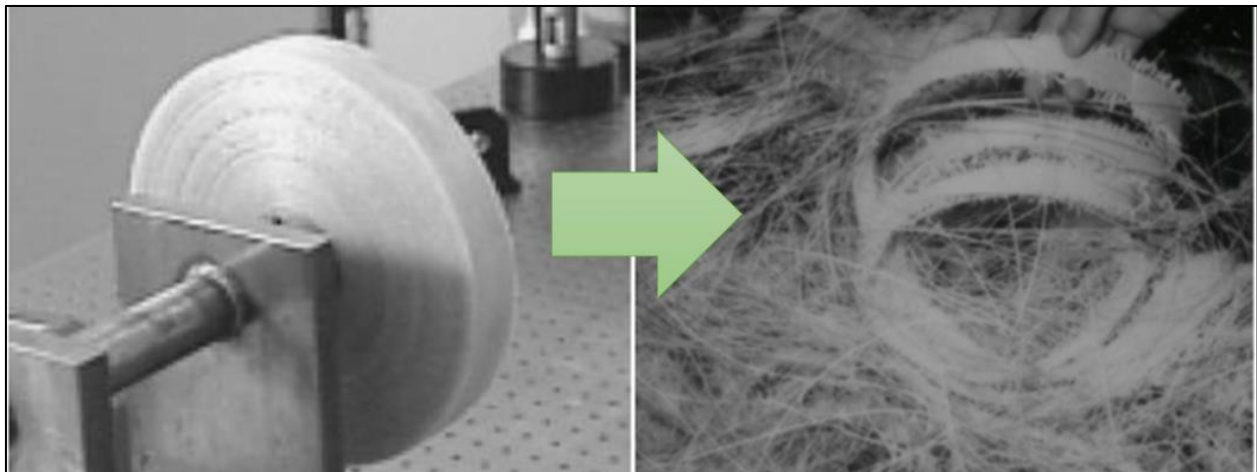


Figure 10: Delamination, caused by an over speed test, ETH Zürich 1996 [11]

Because of the very short time in which the stored energy is released, rotor burst situations are extremely dangerous. This is particularly hazardous if the housing is not able to withstand the burst-forces. There is a fine line between the need of a stronger containment for operation of the rotor on its strength limit, and an operation at high safety factors, without exploiting the possible material properties. Even if the

calculations include higher safety factors, there is always the possibility of defects, which can be caused by an unfortunate chain of events. However, every material failure starts with a crack.

3.2.1 Fracture Modes of a Translaminar Isentropic CFRP Rotor

Cracks within the material are classified by the forces, which extend the crack, such as tension, shear and the torsional forces. Figure 11 illustrates the two main crack propagations in radial and circular direction.

Interlaminar crack growth occurs between the wound fibers. They are driven by an opening through radial stresses (σ_r) and axial stresses (σ_z), as well as shear stresses caused by acceleration and deceleration of the rotor. Especially wound CFRP rings have a low resistance to this kind of cracking, which can be avoided by a properly designed interference fit.

Translaminar crack propagation occurs radial orientated and requires breaking fibers. Due to a high resistance of the composite in fiber-direction, a radial crack in a perfect manufactured CFRP presume very high transversal stresses (σ_θ) [12].

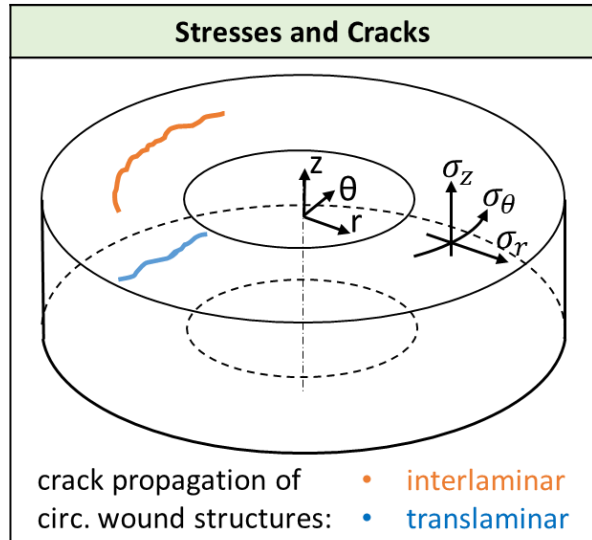


Figure 11: Crack propagation path and stress-direction [12]

3.2.2 Failure Modes of a Unidirectional CFRP

The stress within a wound and press fitted CFRP rotor is dominated by the centrifugal force (during FESS operation) and by the interference pressure. Thermal residual stresses and moisture may effect force strain reduction within the CFRP, but tend to have only a small influence [12]. The occurring stresses can cause a variation of fracture modes and can lead to different related damage consequences, which are explained below.

a) Fiber Failure

The rupture or breakage of the fiber is called *fiber failure*, according to Figure 12. This has to be imagined not as a breakage of a single filament, but as an abrupt simultaneous failure of fiber bundles consisting of hundreds of fibers [8]. In the case of a circularly wound rotor, the failure is caused by high tensile stress $\sigma_\theta^+ = \sigma_{||}^+$. This will not only lead to a resulting decrease in stiffness, but more likely to an entire translaminar fracture over a whole “press fit ring”. This damage could lead to large fragments being released from the rotor. However, real world over-speed tests, recording to the *Flysafe Project* [12] or the *Boing Flywheel* [10], have revealed a particle-like disintegration of the rotor structure, shown in Figure 13. This behavior can be caused by sudden stress relieve of the fiber bundles and a brittle reaction of the polymer, with the consequence of a total loss of fiber matrix adhesion.

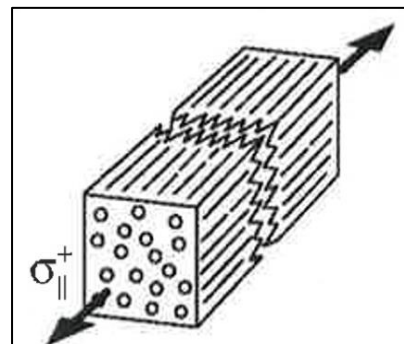


Figure 12: Failure of a unidirectional layer, because of $\sigma_{||}^+$ Strain [8]

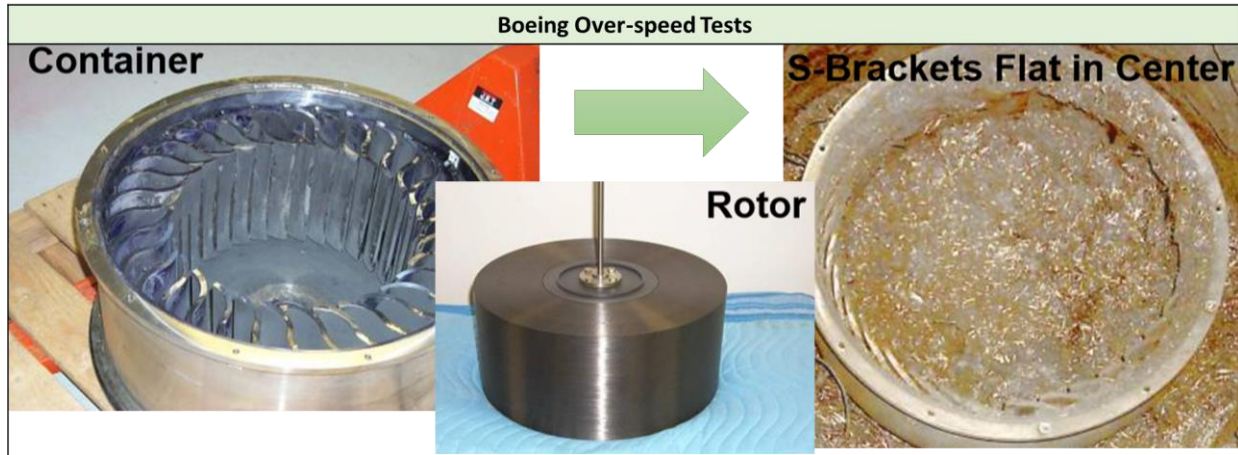


Figure 13: Over speed Tests at 1400 m/s outer tangential speed of the rotor [10]

b) Inter-Fiber Failure

These failure modes depend on the matrix polymer and their fiber connection. The occurring fracture behavior can be distinguished by the mechanical exposure.

Transversal Tensile Stress:

Due to the projected structure, this tensile stress will appear in the radial direction of the rotor. If only transversal tensile stress $\sigma_{\perp}^+ = \sigma_r^+$ occurs, the plane of action and the fracture plane will be the same and match the values of the fracture resistance in this plane, as shown in Figure 14 [8]. This kind of failure can be seen as a consequence of a radial displacement, due to high centrifugal forces, or caused by thermal residual stresses. A specific form of this interfere failure is the delamination of the wound layers, which can be observed according to Figure 10 as result of uncontrolled curing, conditioning process during manufacturing, or too high fiber content of the composite.

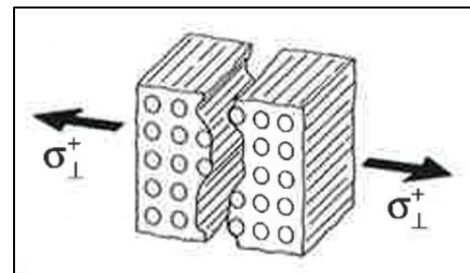


Figure 14: Break due to transversal tensile stress [8]

Transversal Compression σ_{\perp}^- :

A transversely compressed sample breaks in an inclined plane to the plan of action. Due to a normally orientated high compressing resistance, the breakage results in a shear failure as it is shown in Figure 15 [8]. This is an important aspect related to the interference fit, which can cause high radial interface pressure $\sigma_r^- = \sigma_{\perp}^-$. It is likely that such a defect will occur in the form of a conical material breakout at the press-fitted edges, which must be prevented.

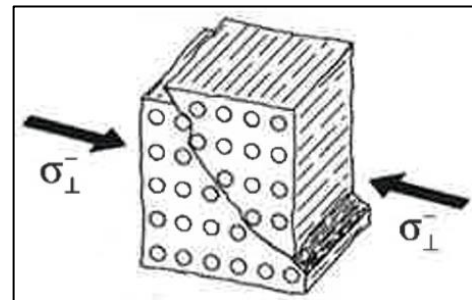


Figure 15: Break due to transversal compression [8]

Transversal Longitudinal Shear:

Shear strain relies on a balance of two parallel inverse oriented pairs of forces, the longitudinal transversal τ_{ll} and the transversal longitudinal shear τ_{ll} . Based on the very high shear resistance in the longitudinal transversal direction, the break plane matches with the transversal longitudinal plane of action, illustrated in Figure 16 [8]. Due to the circular wound rotor structure, this strain appears during acceleration or deceleration. According to the relatively high shear resistance of the composite in this direction, the occurring shear loads do not reach the material limit values by far and are therefore neglected.

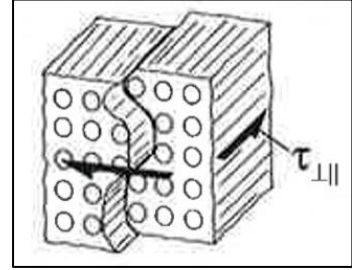


Figure 16: Break due to transversal longitudinal shear [8]

Transversal Transversal Shear:

The break plane caused by transversal transversal shear strains $\tau_{\perp\perp}$ does not match with the plane of acting of the occurring strains (Figure 17). The break lies at a 45° inclined plane, resulting from the weaker resistance to the main transverse tension [8]. This shear failure occurs during the press-fitting procedure, caused by the surface friction of the interference faces. The possible fracture mode will be the same as mentioned previously due to transverse compression at the press-fitted edges and must be avoided as well.

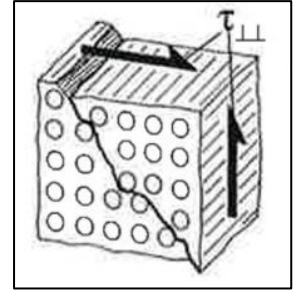


Figure 17: Break due to transverse transverse shear [8]

3.2.3 Failure Initiation

Based on an appropriate rotor design, the rotational speed limits can be calculated by a simple equation depending on the maximal occurring circumferential stress σ_{θ} , described by the rotational speed ω , the CFRP density ρ and the outer radius r [9].

$$\sigma_{\theta} = \rho\omega^2r^2 \quad (2)$$

The calculation for the outer tangential speed v_{θ} leads to a speed limit of 1400 m/s (Figure 13), with the maximum strain σ_{θ} of about 3100 MPa, as demonstrated in the following equation:

$$v_{\theta} = r\omega = \sqrt{\frac{\sigma_{\theta}}{\rho}} = \sqrt{\frac{3100 * 10^6}{1600}} = 1391 \text{ m/s} \quad (3)$$

These relations drive further development for stronger, more resistant fibers and composites.

However, in most cases, the source of critical defects, which may cause total failures of the rotor, is the result of different influences and events. These are related to manufacturing, assembly, transportation and operation processes. The influences and their consequences are listed below [12]:

- **An unlikely critical failure** that probably causes a rotor burst with serious effects on the environments due to fiber damage. This includes cut or broken fibers as consequence of the machining processes. These failures lead to inhomogeneous hoop stresses and thus to stress concentrations, which may cause translaminar as well as interlaminar crack propagation.
- **A production error**, which is likely to be detected during the quality control process. These defects are related to:
 - Contamination-like particles wrapped during filament winding
 - Wrong curing cycles
 - Incorrect material temperature during processing
 - Winding errors due to inaccurate fiber pre-tension and embedded air inclusion
 - Damage during assembly
- **A possible operating error**, caused by:
 - Transport damage due to impact loads
 - Overspeed operation due to a motor control error
 - Vacuum loss during the operation. Based on viscous dissipation, the increase of the pressure at high-speed rotation will heat up the surface due to gas friction processes and can lead to a weakened outer CFRP layer.

4 Theory of the CFRP Rotor Burst Containment

4.1 General Impact on the Containment in Case of a CFRP Rotor Burst

To configure an appropriate containment, it is important to estimate the impact parameters. As explained in chapter 3, there are several different failure possibilities, which can lead to different fracture appearances. These are supposed to occur in combination and generate the impact on the safety housing. Figure 18 gives a short overview of possible impact variation.

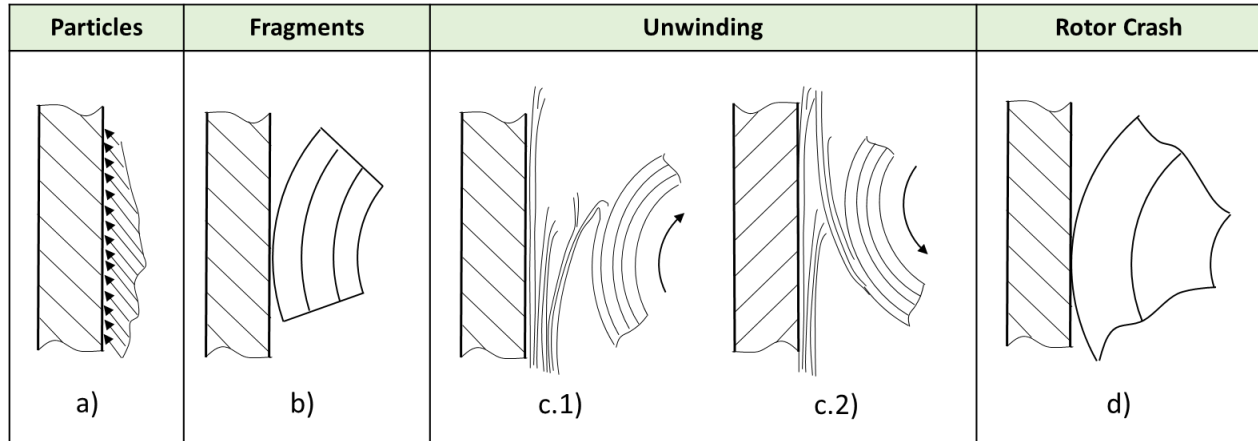


Figure 18: Impact variation a) Particle impact, b) Fragments with intact structure, c) Unwinding processes with different direction of rotation, d) Rotor Crash by contact of the intact rotor with the containment

a) Particle Impact

The so-called “rapid disassembly” is based on the consideration of a total disintegration of the whole rotor structure into small particles. This impact likely occurs due to abrupt fiber failure. This is caused by excessive circumferential tensile strain of the composite.

Three main calculation approaches can be used to calculate the particle impact on the inner containment walls:

- Gas Pressure Model
- Impulse Model
- Particle Ring Model

Due to a generated “particle stream”, the containment experiences severe radial wall pressure and an axial pressure on the top and bottom plate based on accumulation and deviation processes of the stream. The resulting torque depends on the radial distance between the outer surface of the rotor and the inner surface of the containment.

b) Fragment Impact

If a translaminar crack propagates over a certain number of layers without reaching the circumferential stress limits, it may cause a separation of large rotor fragments. Due to the mass and movement of the released fragments, they have a high translation energy, which leads to strong local impact forces in radial and tangential direction. The fragment dynamic is comparable to the burst impact of a rotor made of isotropic material behavior.

c) Unwinding

Unwinding of the rotors coiled up CFRP layers is caused by delamination processes, which is a special case of rotor failure due to transversal tensile stress. Therefore, the coiling orientation compared to the direction of rotation will lead to different impact appearances, illustrated in Figure 18. However, the impact load will result in a relatively small uniform radial and tangential wall pressure.

d) Rotor Crash

Presuming that the rotor is still intact, the radial impact on the containment (compared to a rotor break) should be very small. This situation can be caused, as mentioned in Section 3.1, by a bearing breakdown or a collapsing shaft. The situation becomes dangerous when radial impact reactions build up and lead to total destruction of the carbon fiber structure of the rotor.

4.2 Containment Loads occurring in the Event of Rotor Damage

To avoid a housing failure and protrusion of rotor fragments, which could cause serious damage, or in the worst case scenario, harm surrounding people, the containment has to resist the occurring burst forces. In the case of rotor failure, the housing has to absorb three main acting forces.

- **Radial Pressure:** Induced by the radial translation depending on the debris appearance (shape, angular dimensions, mass), or by circular movement along the containment wall, which causes secondary centrifugal forces.

Big fragments lead to high local pressure values at the impact zone, in contrast to the particle impact that theoretically generates a mostly uniform pressure distribution.

According to the “pipe formula”, the radial pressure results in high circumferential stresses that the containment has to be able to resist.

In contrast to burst behaviors of rotors made from isotropic materials, it is one main challenge to estimate the resulting axial forces on the lid and the bottom of the cylindrical housing, to avoid axial lift-off of these parts.

- **Torque:** Caused by friction-related contact forces at high values of a relative motion between rotor debris and the inner containment walls.

If the housing is designed as a “rigid body”, this momentum leads to high attachment loads, which have to be sustained.

4.3 Analytical Calculation Methods in the Case of a Particle Impact [13]

The following methods were developed in course of the EU project *FLYSAFE* in 1999 [14]. Measurements of the acting radial and axial forces on the surrounding containment, caused by a carbon fiber rotor over-speed test, led to three main theories used to calculate the resulting impact. Each of these theories is based on an occurring “particle stream”, as mentioned previously and was developed by *Reimund Grothaus* (EAST-4D CARBON TECHNOLOGY GMBH). Unfortunately, the used pressure distributions of the experiments have not been published.

a) Gas Pressure Model (GPM)

The model assumes that the created particles can be described as a high-pressure gas. Therefore, the energy of the gas E_{Gas} equals the resulting pressure p_{GPM} times the volume capacity of the burst chamber $V_{Chamber}$.

$$E_{Gas} = p_{GPM} * V_{Chamber} \quad (4)$$

Furthermore, it is postulated that the kinetic energy of the rotating carbon fiber structure E_{kin} is proportionally reduced by a correction factor k_{GPM} (approximately 30%) to obtain the energy of the gas E_{Gas} , as resulting impact of carbon fiber particles to the containment.

$$E_{Gas} = k_{GPM} * E_{kin} \quad (5)$$

This value is relatively small, since the main part of the fiber particles continues to a circular movement. Implementing the friction coefficient μ (approximately 0.05), it is possible to develop the desired relationships for the wall pressure depending force on the cover and the friction based torque.

b) Impulse Model

The impulse model assumes that at the occurring failure, the fiber composite transforms instantly into many small pieces, which are no longer held on a circular path and move tangentially outward. The particles from the outermost surface primarily impact the containment wall. Particles from inner layers follow with a temporal offset.

If the impulse and the time dependence of the incoming particles can be determined, the resulting force and pressure can be calculated:

$$p_{IMP} = \frac{\rho * \omega^2}{2} * \frac{d_a^4}{D^4} * (D^2 - d_a^2) \quad (6)$$

p_{IMP} ... Impact pressure [Pa]

ρ ... Density of the CFRP composite [kg/m³]

ω ... Angular velocity [rad/s]

d_a ... Outer diameter of the Flywheel [m]

D ... Inner diameter of the containment wall [m]

Figure 19 illustrates the influence of the gap between the outer rotor and the inner wall surface of the containment as a function of the ratio of rotor diameter d_a to a variable inner containment diameter D .

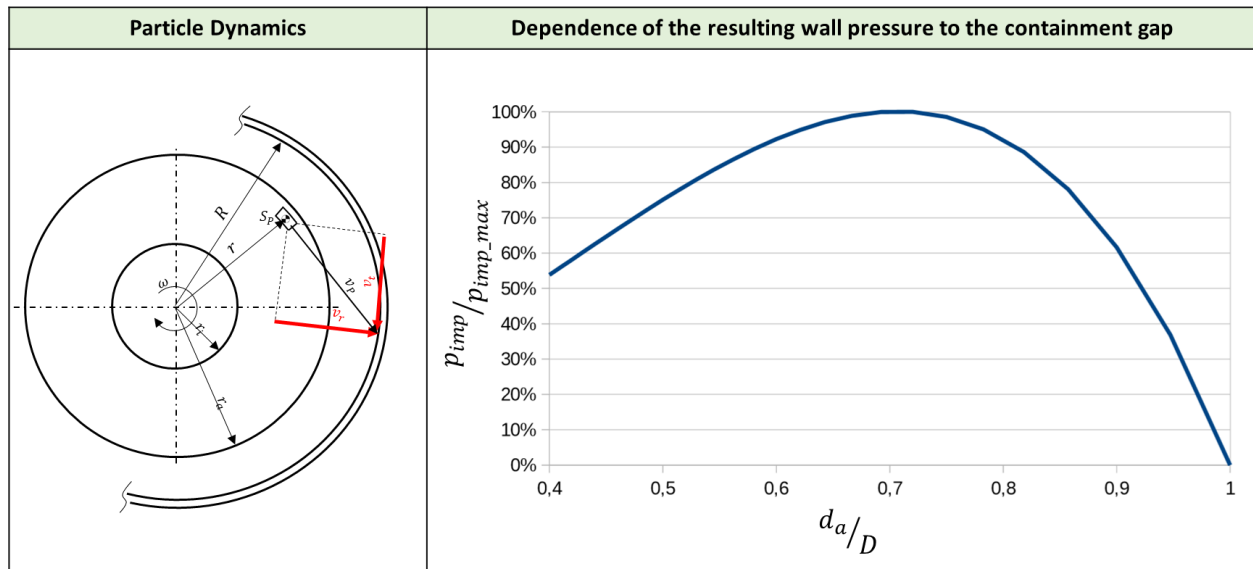


Figure 19: Particle movement (left) and the impact pressure depending on the containment gap (right) [13]

If there is only a tiny gap, the outer particles will generate very little pressure on the wall due to the short distance and the flat impact angle, in contrast to the inner one, which reaches far higher impact values. Certainly, the particles from the inner layers will not be able to transfer their full impulse energy to the wall because of collisions with other moving particles.

At a diameter ratio of 72%, the pieces reach the highest pressure values, provided they are able to move freely.

For a small gap, the equation (6) gives the correct pressure of the first impact, but the maximum load from the whole rotor will be much higher. Therefore, the model leads to more accurate/exact pressures in cases where the distance between the containment and the rotor is bigger. To obtain better results for smaller gap dimensions, the effect of a tangential moving “particle stream” on the inside of the housing is considered. Because this tangential movement also causes centrifugal forces, which have to be contained by the housing structure. Consequently, the last method, the *particle ring model*, has been developed.

c) Particle Ring Model

If the gap between the bursting ring and the housing is small, almost immediately after failure the fiber particles will rotate as a “ring” forced to the containment wall, as is illustrated in Figure 20. It is expected that the greatest compression on the housing occurs when all released particles have reached the wall and are now part of a “circulating particle stream”. This particle stream exerts its pressure like a liquid through the rotation. Therefore, in the past, this model was also known as the “*liquid ring model*”.

In contrast to the previously described *impulse model*, the maximum generated impulse pressure does not occur at the moment of the first impact of particles from the outer layers, but rather at the time when all particles have reached the “particle ring” (build-up of debris) on the containment wall.

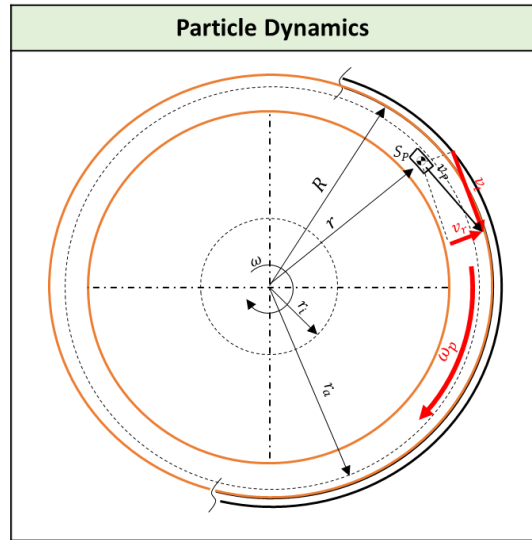


Figure 20: Generated particle-stream (orange)

d) Model Comparison

According to Figure 21, it can be seen that for a narrow gap, the wall pressure reaches a maximum for the calculation with the *gas pressure* and the *particle ring model*. If the dimension of the inner chamber diameter D increases to a lower ratio d_a/D of approximately 0.86, the wall pressure of the circular particle stream is still greater than the maximum impact pressure. From this point on, further decreasing the ratio d_a/D results in a higher pressure, than the particle ring pressure. Therefore, it is always recommended to use both models to assess the load on the housing. The values of the gas pressure model are also interesting at narrow containment gaps, which mostly match the results of the particle ring model. For larger diameter ratios, the gas model results are always about 50% less than the other two more complex models.

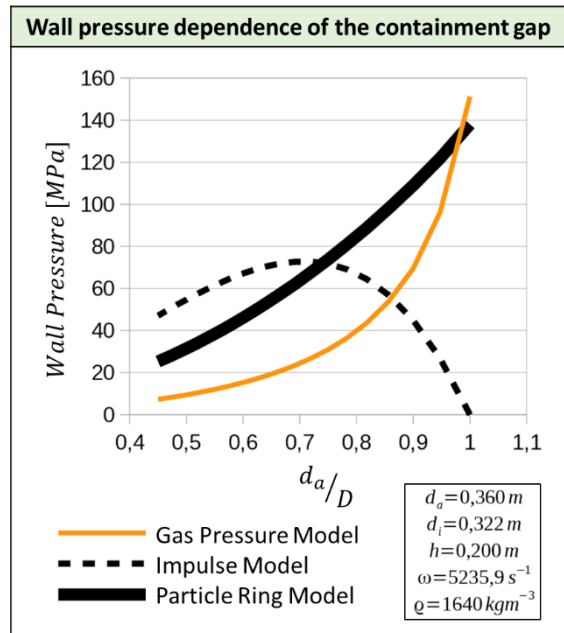


Figure 21: Comparison of all three models [13]

4.4 Containment Concepts for CFRP Rotor Flywheel Systems

In general, the idea of a safe housing design is to absorb or resist the energy released by the rotor, according to the law of energy-conservation. This can be realized by absorbing processes like structural deformation, by energy transfer to a freely rotating ring (which starts to spin due to tangential forces) by pressure chambers that sustain or guide the generated particle stream and, of course, by a combination of these measures. Some design suggestions to absorb or resist the acting loads are listed below:

a) "S-Brackets" by Boeing Phantom Works (2012)

Based on an executed flywheel project by Boeing [10], the company has developed and tested the absorbing effects of vertical "S-brackets" made of ductile steel, which are circularly attached to the inner surface of the containment, illustrated in Figure 13 / Chapter 3.2.2. In case of a total destruction of the flywheel, the energy of the particles is transferred into deformation work to flatten the S-Brackets along the wall. This means that the needed deformation work for manufacturing the brackets nearly equals the energy, which can be absorbed, neglecting effects due to rapid deformation rates such as strain hardening and temperature softening (Explained in more detail in section 7.3.1 and Figure 64). The deceleration of fragments and particles is able to reduce radial and axial pressure maxima, as well as the induced torque on the housing, due to a strong kinetic energy absorption of the deformed containment structure.

b) Rotating Liner

In case of a narrow containment gap design, the major part of the impact force is oriented in tangential direction. Friction between the further rotating debris and the housing induces a high momentum to the surrounding structure. To reduce this torque, a freely "rotating liner" is mounted between the outer main housing structure and the flywheel, as illustrated in Figure 22. Due to acceleration of the ring by the tangential forces, a part of the released energy is transferred into the movement of the rotating liner. According to calculations by FESS expert Frank Täubner [14], this implementation leads to rest torque values of only 10% of the induced momentum. In comparison to the S-Brackets, the Rotating Liner does not reduce the acting pressure on the containment walls.

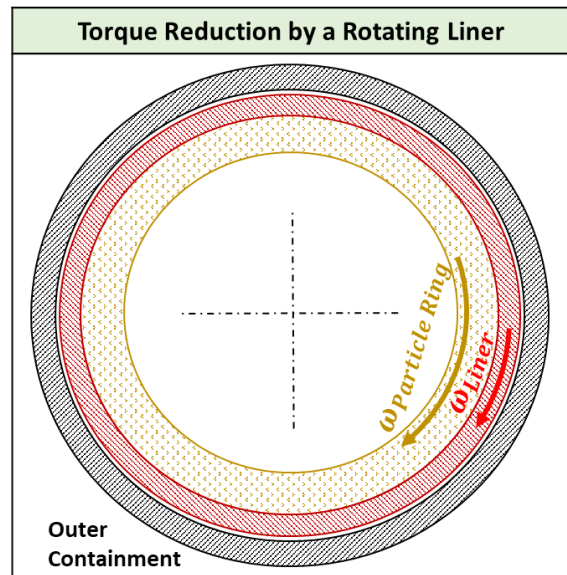


Figure 22: Schematic illustration of a rotating liner

c) Particle Stream Guidance

If a composite rotor failure generates a particle stream, the radial impact accumulation leads to a deviation into the axial direction. To mitigate axial pressure on bottom and top surfaces, the burst related particle stream has to be deflected back to the center, as shown in Figure 23. Such systems (patent application publication [15]) prevent the main housing structure from axial pressure, but they do not avoid the axial forces. The resulting force by guided streams has to be obtained by the imbedded ring. Implementation of these additional design measures will not bring the desired weight savings.

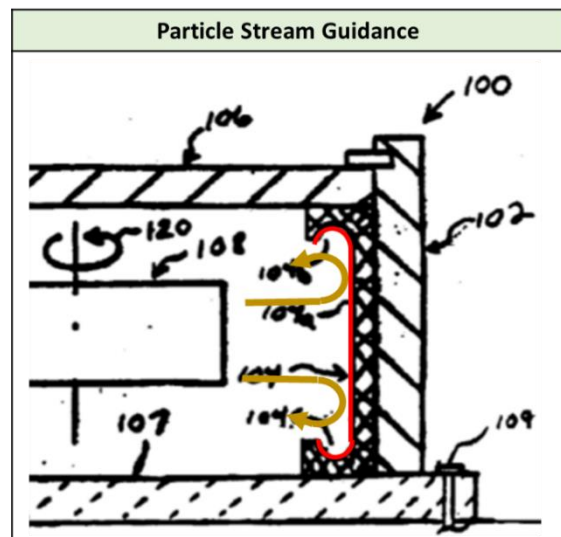


Figure 23: Schematic idea of a particle guidance [15]

5 Systematic Rotor Burst Testing

5.1 Test Rig Design for Steel Rotor Burst Tests [1]

As mentioned in section 1.3 an own low-cost test rig for spin testing was designed in previous work by [4], [5] and [6]. The goal of the empirical investigation lies in the determination of an analytic relation between the kinetic energy of the rotor (or rotor fragments) and the energy absorption ability of the burst containment/housing while retaining structural integrity, as well as validation of numerical models in the long run.

The specialized test rig design, shown in Figure 24, can be divided into four main modules, which are described below.

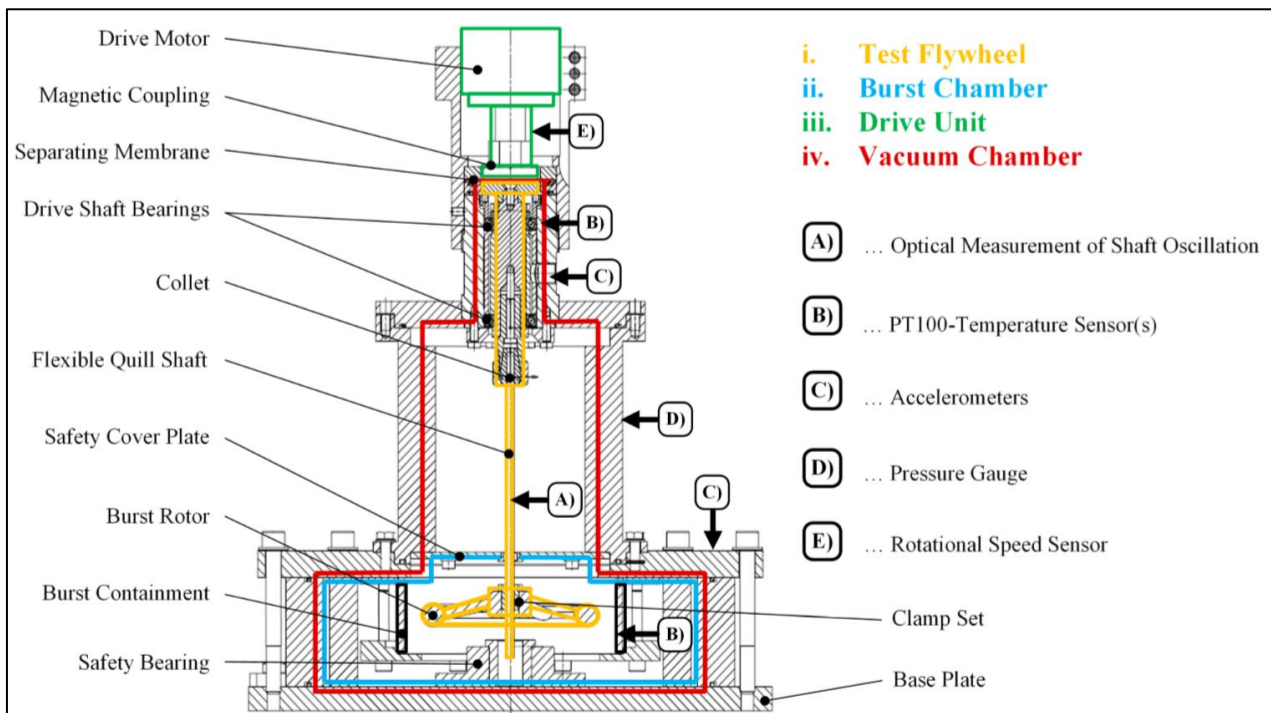


Figure 24: Cross section of the burst test rig including measurement technology [1]

i. Test Flywheel (orange)

The *test flywheel*, which will be deliberately destroyed during the burst test, is fixed on a flexible, cantilevered *quill shaft* via a clamp set. On the one hand, resonance frequency and the influence of imbalance forces are mitigated, on the other hand, peak forces during rotor burst can hardly be transmitted to the spindle bearings and drive unit. The flexible, 6 mm thick quill shaft is fed through a safety cover plate, to avoid the entering of rotor debris towards the bearings system

ii. Burst Chamber (blue)

The burst chamber accommodates the burst containment under investigation. In the current configuration, these test specimens are cylindrical metal parts with a fitted key to avoid rotation during fragment impact. The exact geometry of the burst containments are listed in Section 7.1. The outer walls of the test rig's burst chamber are made of 30 mm solid steel. The safety bearing (a sliding bearing made

from Polyoxymethylene—POM), which limits excessive oscillation and plastic deformation of the quill shaft during resonance run-through, is fixed in the center of the base plate.

iii. Drive Unit (green)

The electric motor (asynchronous machine and variable frequency drive by the company *Mechatron*) provides a maximum power of 2.2 kW and 42,000 rpm. The torque is transmitted to the shaft via disc magnetic coupling, which allows hermetical sealing of the burst chamber from the environment.

iv. Vacuum Chamber (red)

Evacuating the burst chamber is mostly necessary to reduce the aerodynamic drag of the test flywheel and to avoid influences of the burst tests by viscous damping and gas friction effects. The pressure level can be lowered to around 0.5 mbar by using a simple two-stage rotary vane pump.

A photograph of the final setup including data acquisition and periphery is shown in Figure 25.

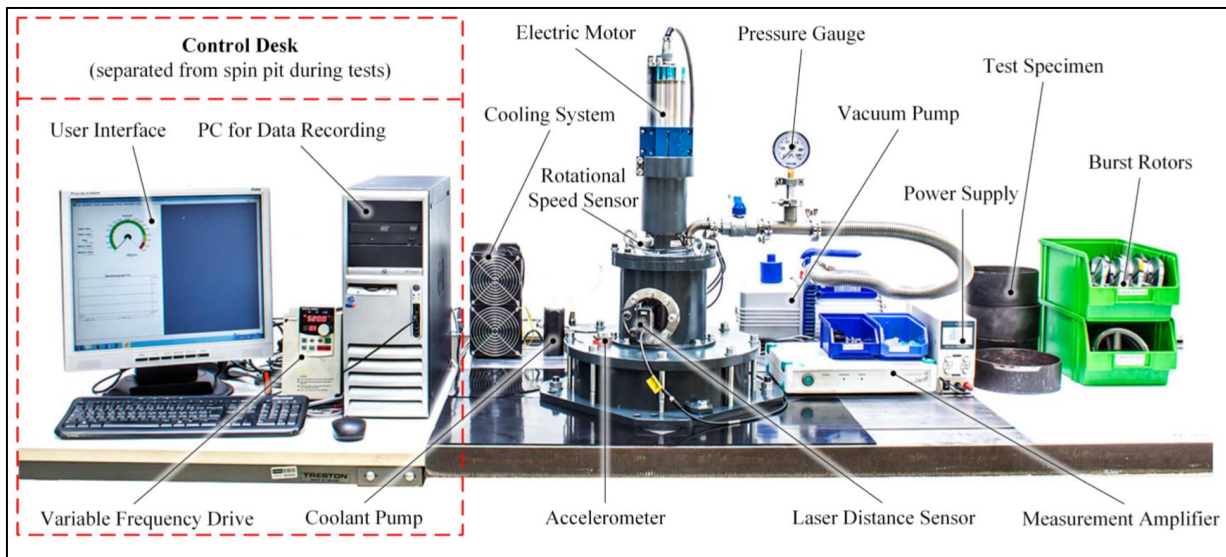


Figure 25: Test-Rig with the major components including the periphery. The control desk (left) can be moved away from the rig when burst tests are conducted. [1]

5.2 Introduction of Steel Rotor Flywheel Systems

Even today, flywheels with high energy content are manufactured from isotropic materials like steel and cast iron. To reach improved levels of specific energy, some rotors are made of high-strength laminated steel. Compared to anisotropic materials such as e.g. tangential isotropic CFRP, the specific strength (σ_{max}/ρ) of steel is far lower, because of its high density ρ , but it is possible to achieve higher shape-factors K of up to 0.95 [16].

Figure 26 gives an overview of different rotor shapes and their shape factor K to calculate the mass related specific energy density E/m of a rotating system. Equation (7) illustrates the relationship between stored energy, rotor material and shape.

$$\frac{E}{m} = K * \frac{\sigma_{max}}{\rho} \quad (7)$$

- $E...$ Stored Energy [J]
- $m...$ Mass [kg]
- $K...$ Shape-factor [1]
- $\sigma_{max}...$ Max. strength [N/m²]
- $\rho...$ Density [kg/m³]

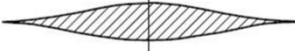
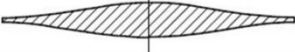


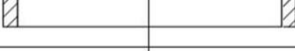

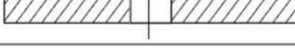
Description	Shape	Shape-factor
Ideal disc design with equal strength		1,00
Real disc design with equal strength		0,70-0,90
Cone shaped disc		0,70-0,85
Disc with equal thickness		0,606
Thin ring		0,50
Disc with outer ring		0,40-0,50
Thick ring		0,303

Figure 26: Different flywheel-shapes with the linked Shape-factors [17]

Another big advantage of steel rotors are the lower costs for material and manufacturing compared to CFRP structures. This applies especially to stationary applications as there is less importance on low mass and compact size.

In the case of the *FlyGrid* project, the simple isotropic material behavior of steel and cast iron is used for predictable impact geometries and energies to verify different containment structures in a rotor burst series.

Burst Behavior of Steel Rotors:

Flywheels made of isotropic materials show the characteristic that they usually burst into a few, equally sized fragments. The classic burst case is a three-sector burst, also called “tri-burst”. However, this means that the fragments have a very high amount of energy and, therefore, an enormous destruction power [17].

Figure 27 shows a classic isotropic tri-burst behavior of a steel rotor. It was part of a study by *Lockheed Martin* in 1972, which dealt with a flywheel application as a mobile energy storage in cars.

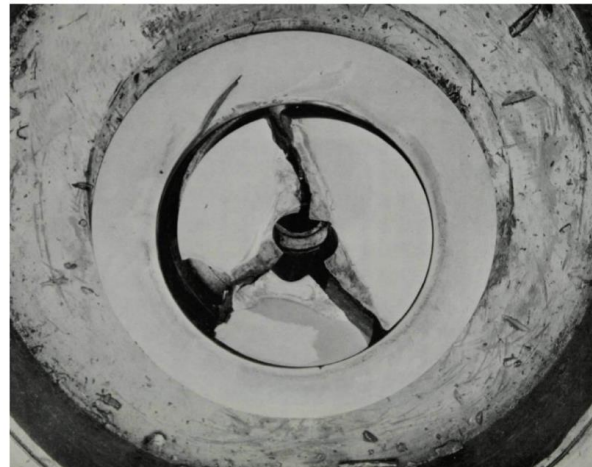


Figure 27: Lockheed Martin Burst-Flywheel [32]

5.3 Down-Scaled Burst Rotor Design

The general task of a *test flywheel* used in the special test rig is to reach the structural and material limits of a rotor until it bursts. Rings and solid discs show a special fragment bursting in big segments. For our case, we used two different types of burst flywheels, which are shown in Figure 28 and Figure 29.



Figure 28: Milled flywheel structure

The **milled flywheel** structure is specifically designed for an easy predictable burst speed and a more realistic fracture behavior. It is made from C45E and the burst speed depends on the notch design and reaches 28,600 rpm.

Advantages:

- Burst fragments match with the strength calculation
- Predictable burst rotation speed based on material tests
- Defined fragment energy and kinetic behavior

Disadvantage:

- Expensive production

The **cast iron hand wheel** is a highly economic off-the-shelf item, which reduces the testing costs enormously. Without notches, the gray cast iron structure reaches burst speeds of up to 30,600 rpm.

Advantage:

- Cheap purchased item
- Easily available
- Brittle burst behavior

Disadvantage:

- Strongly varying burst rotation speed
- No easily predictable impact behavior



Figure 29: Gray cast iron hand wheel

5.3.1 Variation of the Impact Energy of Milled Burst Rotor

In order to be able to determine the occurring stresses in a component, the acting forces /stresses must be considered. For rotating components, the centrifugal force must be identified in addition to the external acting forces.

Equation (8) shows the general equation for the centrifugal force for a solid rotating disc [18].

$$F_{\omega} = \int_{r_1}^R r * \omega^2 * dm \quad (8)$$

F_{ω} ... Centrifugal force [N]

r_1 ... Inner radius of the disc [m]

R ... Outer radius of the disc [m]

r ... Variable [m]

ω ... Angular speed [rad/s]

dm ... Infinitesimal small mass element [kg]

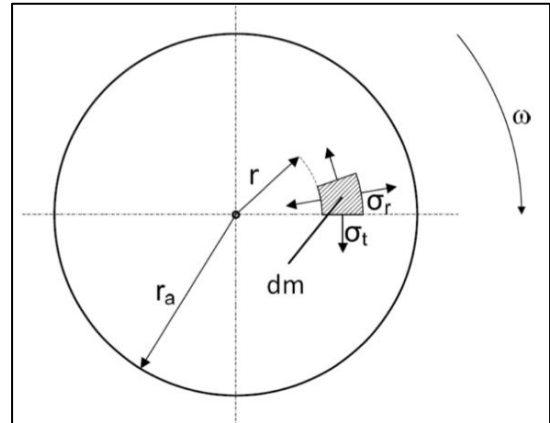


Figure 30: Volume element of a solid rotating disc [4]

Figure 30 illustrates a rotating solid disc. Due to the centrifugal force, the stress situation in the radial and tangential direction can be described.

Based on the geometrical data from the milled burst rotor, the maximum of the appearing stresses can be calculated. Therefore, the general equation of the centrifugal force (9) is adapted to the defined measurements.

$$F_{\omega} = \int_{r_1}^R r^2 * \omega^2 * s * \rho * \hat{\alpha} * dr \quad (9)$$

F_{ω} ... Centrifugal force [N]

r_1 ... Inner radius of the disc [m]

R ... Outer radius of the disc [m]

r ... Variable [m]

ω ... Angular speed [rad/s]

s ... Height of the segment [m]

ρ ... Density of the material [kg/m³]

$\hat{\alpha}$... Segment angular [rad]

dr ... Infinitesimal small radius element [m]

The acting centrifugal force of one segment, related to the cross section surface of the notch leads to the resulting stress (Equation (10)), which the material has to resist.

$$\sigma_r = \frac{F_\omega}{A} \quad (10)$$

σ_r ... Radial stress in the notch [N/m²]

F_ω ... Centrifugal force [N]

A ... Cross section normal to the notch [m²]

Compared to the actual strength of material, as is determined by a tensile test, the calculation leads to the predicted burst speed depending on the height of the notched cross section.

Figure 31 (left) illustrates three different exponentially rising lines. Each of them describe the acting stress related to the rotation speed for different notch root heights. The horizontal line shows the tensile strength level of the material tests. The rotational speed at the intersecting lines mark the estimated burst speed.

The empirically tested burst speeds of 28,690 rpm equal the calculated speed with a small deviation of plus/minus 80 rpm.

Figure 31 (right) shows the three burst segments and the remaining hub after an over speed test. The measured burst speed was 28,638 rpm and matches with the simplified calculation.

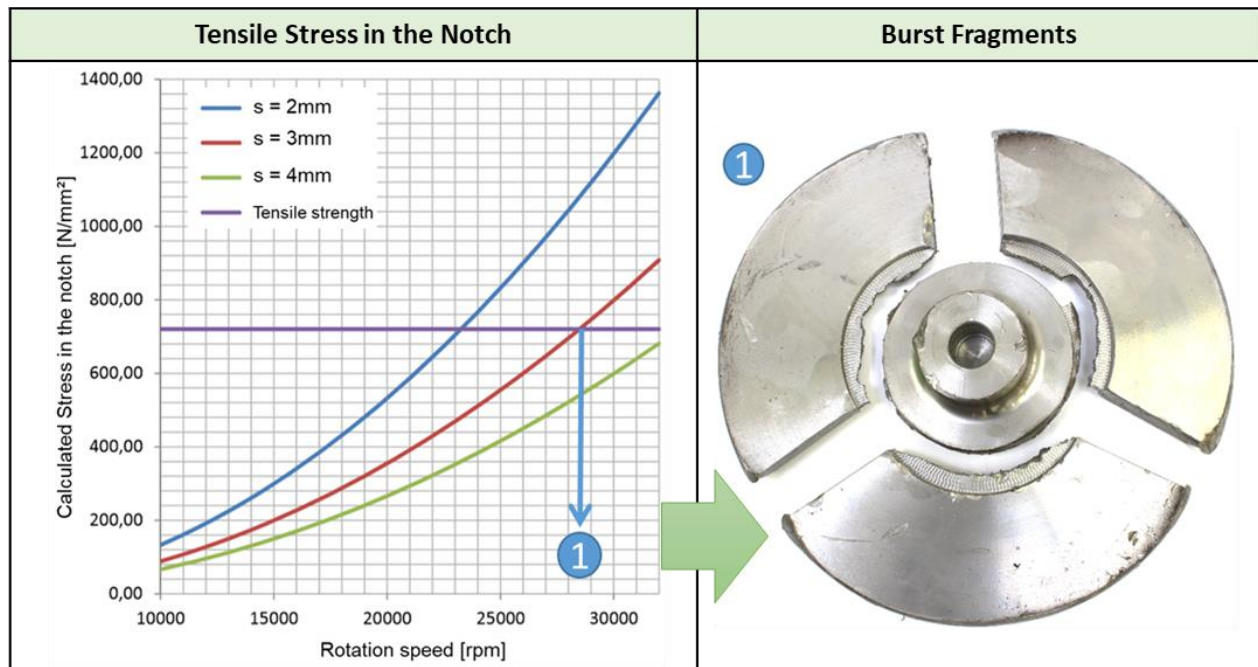


Figure 31: Illustrated stress situation in the notched cross section of the milled flywheel [4] (left), Burst fragments and the remaining hub of the milled flywheel (right)

5.3.2 Variation of the Cast Iron Handwheel Impact Energy

Due to the complexity of the cast iron hand wheel structure and the undefined material behavior, the burst speed was investigated during the empirical test series.

Cast iron handwheels that do not require further preparation or weakening through notches can reach rotational speeds up to 31,000 rpm. To vary the impact energy for a further classification of the tested containments, it is important to generate different impact energies, which are related to the kinetic energy of the rotor at the moment of an occurring failure. Therefore, different notches were added to the structures to realize varying burst speeds. Figure 32 demonstrates the relation between the notching depth and the failure speed. The first fracture illustration shows a 3.5 mm diameter drilled hole with 5 mm depth, which led to a rotor burst at 29,431 rpm, the one below has a through bore with the same diameter at the same position and led to failure at 22,630 rpm.

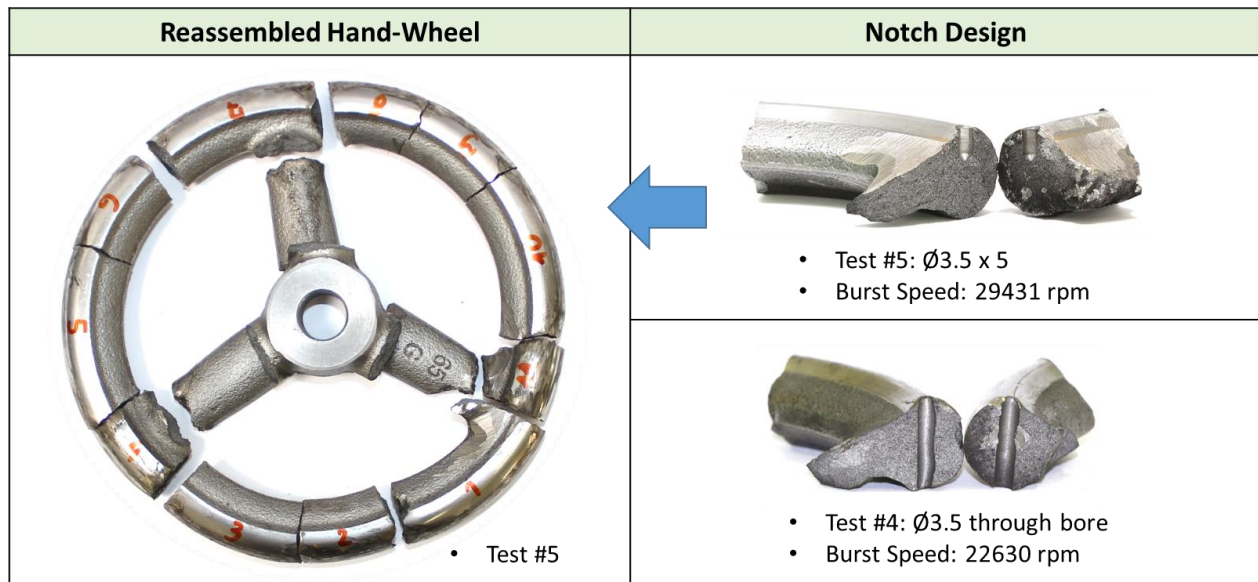


Figure 32: Reassembled cast iron hand wheel fractures after a burst test (left), Different notch-depth and the influenced burst speed (right)

In further research done on the failure mechanism of the hand wheel, the fractures were classified in a pre- and post-occurring damage. Based on an abrasion observation at the outer surface, shown in Figure 33. If an abrasive track runs over a break, it is assumed that the damage did not occur until a contact with the containment. If two fragments have different marks, the fracture will have occurred before an impact.

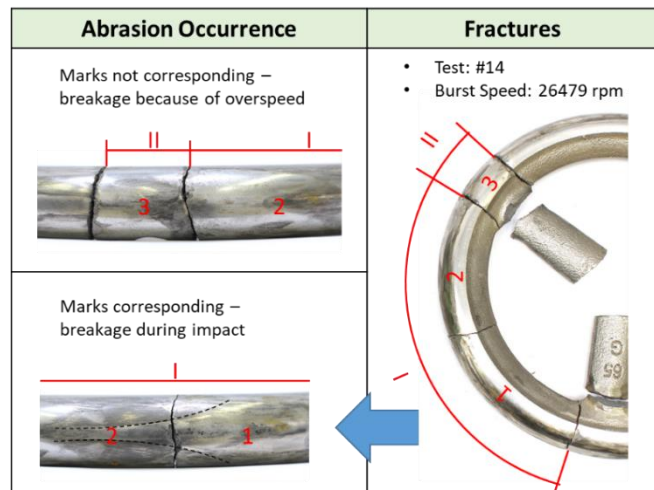


Figure 33: Observed abrasion marks at the outer surface

To consider the fracture energy of the rotor material in the energy balance, the notch bar impact value of was measured.



Figure 34: Samples of cast iron handwheel material prepared for a notch bar test

Figure 34 shows the tested samples, which are cut out of the hand wheel structure. The average value of the absorbed energy is about 0.0701 J/mm^2 . Based on this measurement, the fracture energy varies depending on the number of breaks (from 200 to 300 J per burst), which represent only a very small part of the overall stored kinetic energy.

5.4 Performance of the Previous Burst Tests [1]

Using the test rig and the test flywheels described in Chapters 5.1 and 5.3 respectively, the actual burst test (i.e., accelerating the specimen to rotational speeds, at which the centripetal stresses exceed the material's tensile strength) takes around 10 s. This value may vary depending on balancing quality and moment of inertia of the test flywheel (and related resonances). During the acceleration process, rotational speed, radial acceleration of bearing seats and oscillation of the quill shaft are monitored and recorded (for instrumentation, see Figure 24). Data processing and analysis, on the other hand, are far more time consuming and consist of the three main steps described below.

1. Documentation and Reconstruction

The process starts with an in-situ photo documentation, after which the rotor fragments are re-assembled and matched with the impact marks of the containment. As previously explained, this procedure is used in the case of the grey cast iron hand wheels and does not necessarily apply to all other possible test flywheels. Through investigation of skid marks on rotor and housing (also mentioned in Section 5.3.2), and in some cases color marks, allow identification of rotor crack initiation. By applying this technique, it can be determined whether the rotor fragments were formed due to centripetal forces or broke again during impact. The structure of the process and some examples are illustrated in Figure 35.

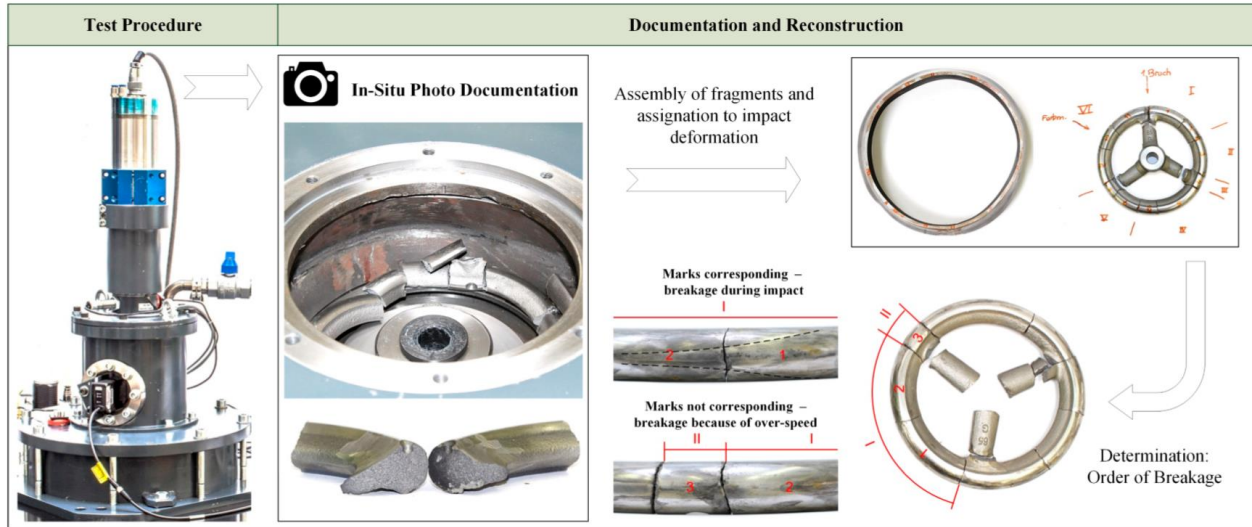


Figure 35: Documentation and reconstruction [1]

2. Evaluation of the deformation work

The plastic deformation work, which is introduced in the burst containment, is a measure for its ability to absorb energy. The desired approach is based on a measurement of the enlargement of the surface area due to this plastic deformation. If the containment was punctured or broken through, there is no possibility to deduce the energy, which was absorbed, since part of the fragment's kinetic energy was absorbed during impact in the spin pit. In all other cases, the plastic deformation work is determined by comparison of the containment geometry before and after impact, as shown in Figure 36.

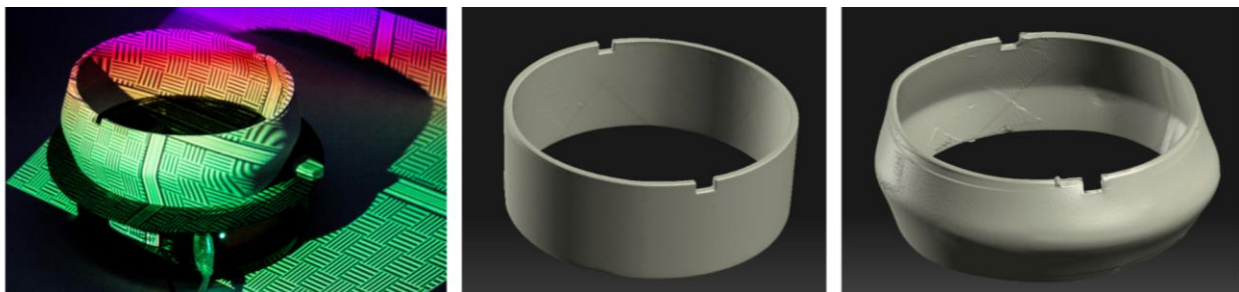


Figure 36: 3D scanning of burst containments (left) including results before (middle) and after (right) the burst [1]

The enlargement compared to the undeformed housing surface defines a plastic strain ratio. With a stress-strain diagram of the containment material, the plastic deformation work can then be calculated as the area under the “ $\sigma\varepsilon$ -curve” as shown in Figure 38 (right).

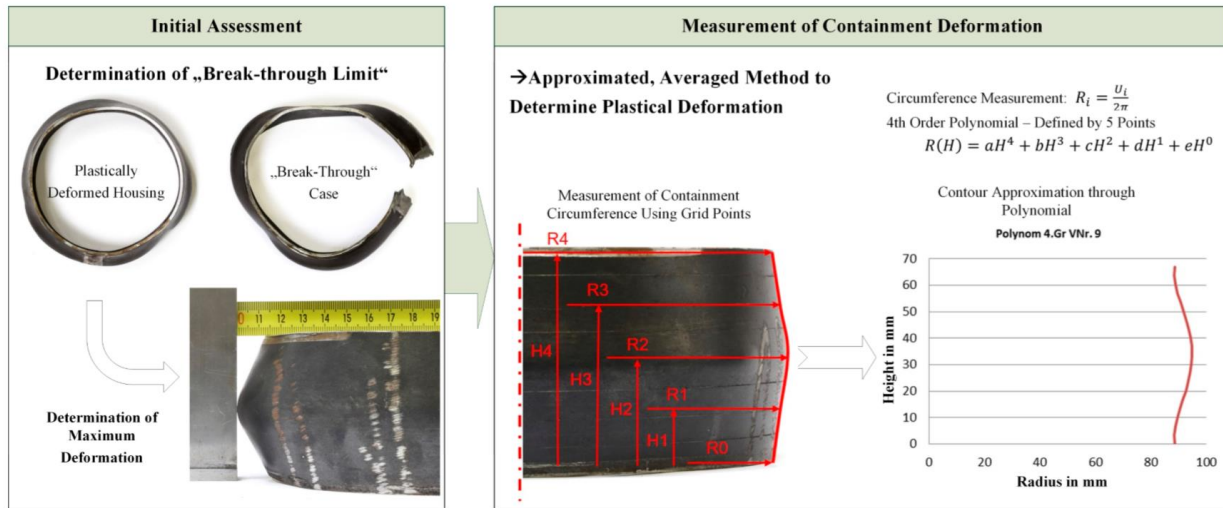


Figure 37: Survey of the containment deformation [1]

The measurement was determined in two different ways:

- **Analytically** by measuring the circumference of the containments at different heights and interpolating the contour by a polynomial of fourth order. This polynomial describes two edges of a finite decimal small truncated cone shell whose lateral areas are summed up (Described in Figure 37, right and in Figure 38, left)
- **Numerically** by comparing the 3D-scanned surface with the initial, undeformed cylinder. The surface area can be determined using automated functions of commercial CAD software such as *CATIA*, *Siemens NX*, or *Autodesk Inventor* (compare Figure 36).

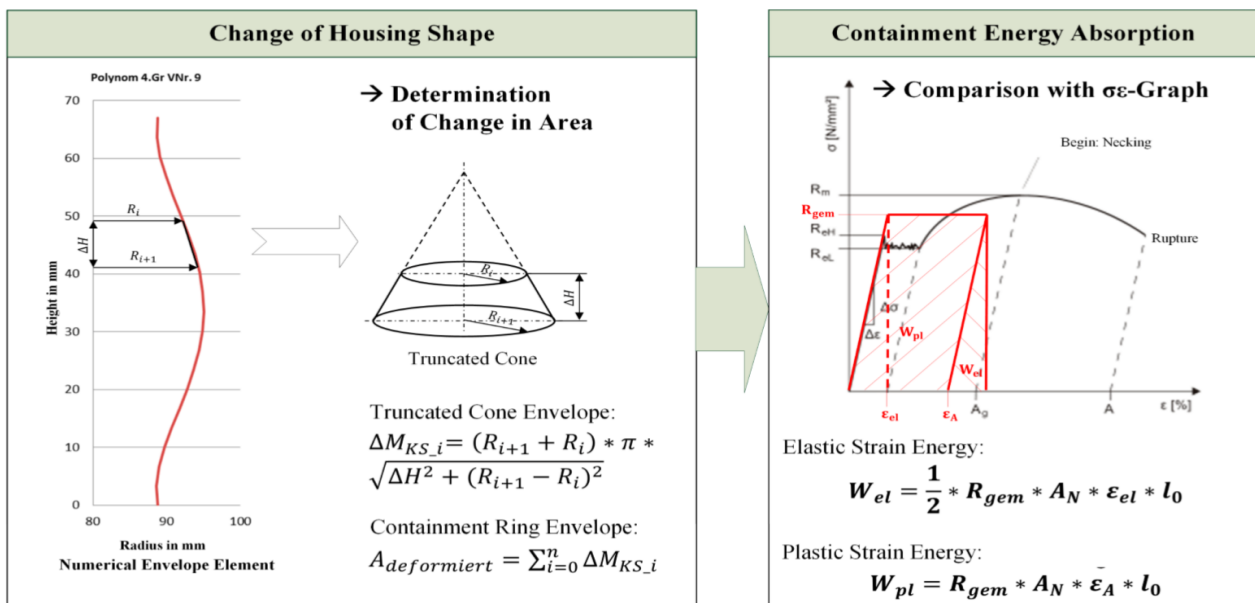


Figure 38: Determination of plastic deformation work of the burst containment [1]

3. Evaluation of the Thermal Energy

Every process involving friction (due to contact or deformation) causes temperature rise in the involved elements. A part of this heat dissipation was measured as temperature entry in the housing by applying temperature sensors to the housing. Figure 39 gives an example of the detected temperature increase of the sensor row 2.1 to 2.4, which demonstrates a heat distribution of an axial cross section of the containment.

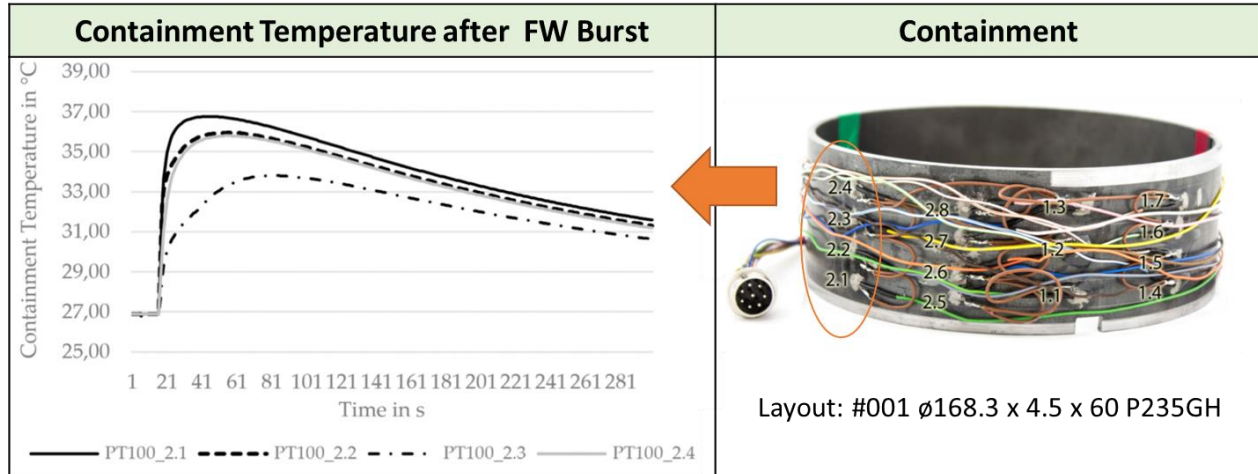


Figure 39: Temperature increase after the rotor burst (left), Distribution of 15 temperature sensors at the containment surface [1]

The maximum temperature increase of around 10 °C is reached immediately after impact and then the temperatures slowly drop again due to heat conduction. Since the actual spin pit is evacuated, there is no convective cooling of the burst containment and radiation can be neglected at these low temperatures. Hence, the energy transformed into heat E_t can be calculated via:

$$E_t = m_h * c_p * \Delta t \quad (11)$$

E_t ... Thermal energy of the containment

m_h ... Mass of the burst containment

c_p ... Specific heat capacity

Δt ... Maximum temperature difference

6 Preparation of the Empirical CFRP Rotor Burst Tests

The following empirical test series are primarily intended for use as a development tool for safe flywheel systems with CFRP rotors. Furthermore, they serve to test the winding process of the carbon fiber, as the manufacturing process of the rotor is a new challenge for the *FlyGrid* carbon fiber specialist (*Secar Technology GmbH*). Therefore, the first rotor bursts were executed by using the in house test rig. Due to little experience concerning CFRP bursting, several adaptations to the test rig were made to ensure safe over-speed testing. Based on the test bench restrictions regarding burst chamber size and the maximum rotation speed, the rotors had to be scaled down and specially modified to allow composite failure at relatively low speeds.

6.1 Test Rig Layout for the CFRP Rotor Burst Tests

Figure 40 shows the cross-section of the used test bench including the construction changes (in bold) and the system limitations.

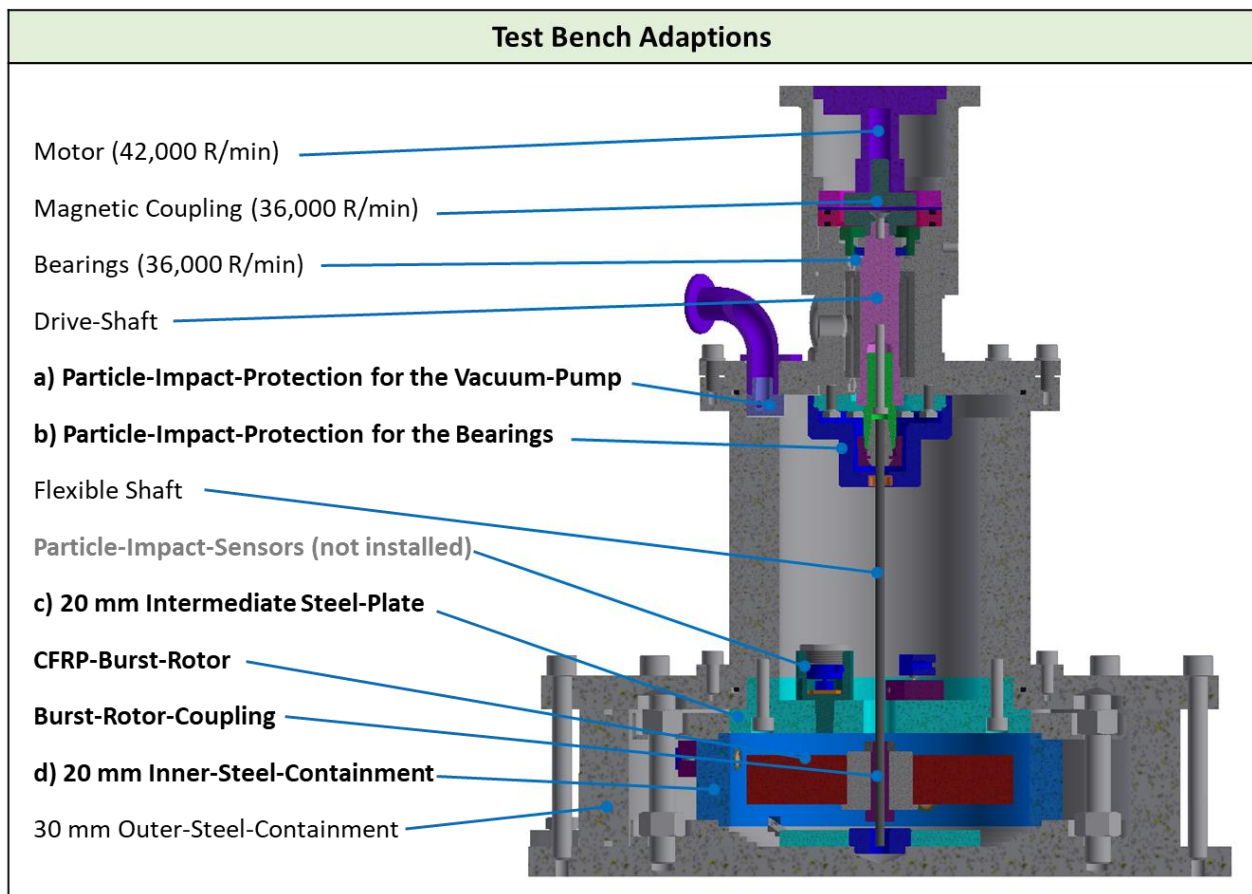


Figure 40: Cross-section of the Test Rig with the CFRP rotor burst adaptations (rotation speed restrictions in brackets)

6.1.1 Test Rig Adaptions

a) Particle-Impact-Protection for the Vacuum-Pump

This attachment was designed to avoid direct inlet of an occurring particle stream into the extraction socket of the vacuum pump, realized by a stainless steel plug, which guides the airstream through small radial holes.

b) Particle-Impact-Protection for the Bearings

It must be ensured that the unsealed precision bearings of the drive shaft are not contaminated by composite particles. Therefore, a protective cap encapsulates the drive shaft from the burst chamber, with its opening for the flexible shaft sealed by a radial shaft seal ring (RSSR). The marked side of the RSSR faces upwards to use the self-enforcing sealing effect in case of a pressure increase on the burst chamber side and allow a proper evacuation of the drive shaft surrounding.

c) Intermediate Steel-Plate

To withstand occurring axial pressures, a massive 20 mm steel plate replaced the original 4 mm intermediate plate.

d) Inner-Steel-Containment

As the existing clamping installation (Figure 60) from the steel rotor burst tests is used, a pipe with 20 mm wall thickness was adapted to form the inner burst ring, with the possibility to attach further particle pressure sensors without weakening the structure.

6.1.2 System Limitations

The used test rig leads to several restrictions in relation to the possible rotation speed limits of the used mechanical parts and the existing chamber size.

Speed Limits:

The electric motor and the corresponding frequency-inverter reach a maximum rotation speed of 42,000 rpm, but the actual operating speed is limited by the installed machine elements of the drive train, such as the magnetic clutch and the bearings. According to the manufacturer, the clutch is able to resist centrifugal forces at speeds up to 26,000 rpm, which is restricted by the relatively weak structure of the glued magnetic inlays. The grease lubricated precision bearings reach their maximum speeds at 32,000 rpm, according to the data sheet. Both of these values assume a continuous operation. However, personal experience and the overall safe enclosure construction of the test rig, led to short-term over-load operational speeds of up to 36,000 rpm, without damaging the system.

Chamber Size:

The main restriction for the maximum rotor size is linked to the 300 mm clear span and the 80 mm height of the outer containment ring. To guarantee maximum safety, a second inner containment was implemented. To enable additional sensor attachments by providing enough surrounding volume, this inner ring is significantly smaller and leads to a maximum test rotor dimensions of 180 mm in diameter and 60 mm in height.

Based on these restrictions, the challenge was to develop a small-scale rotor design that allows CFRP failure occurrence at low rotational speeds.

6.2 Implemented Sensors

Figure 41 illustrates the used sensor attachments for condition monitoring tasks during the operation, as well as for burst related values like burst speed, accelerations and wall pressures.

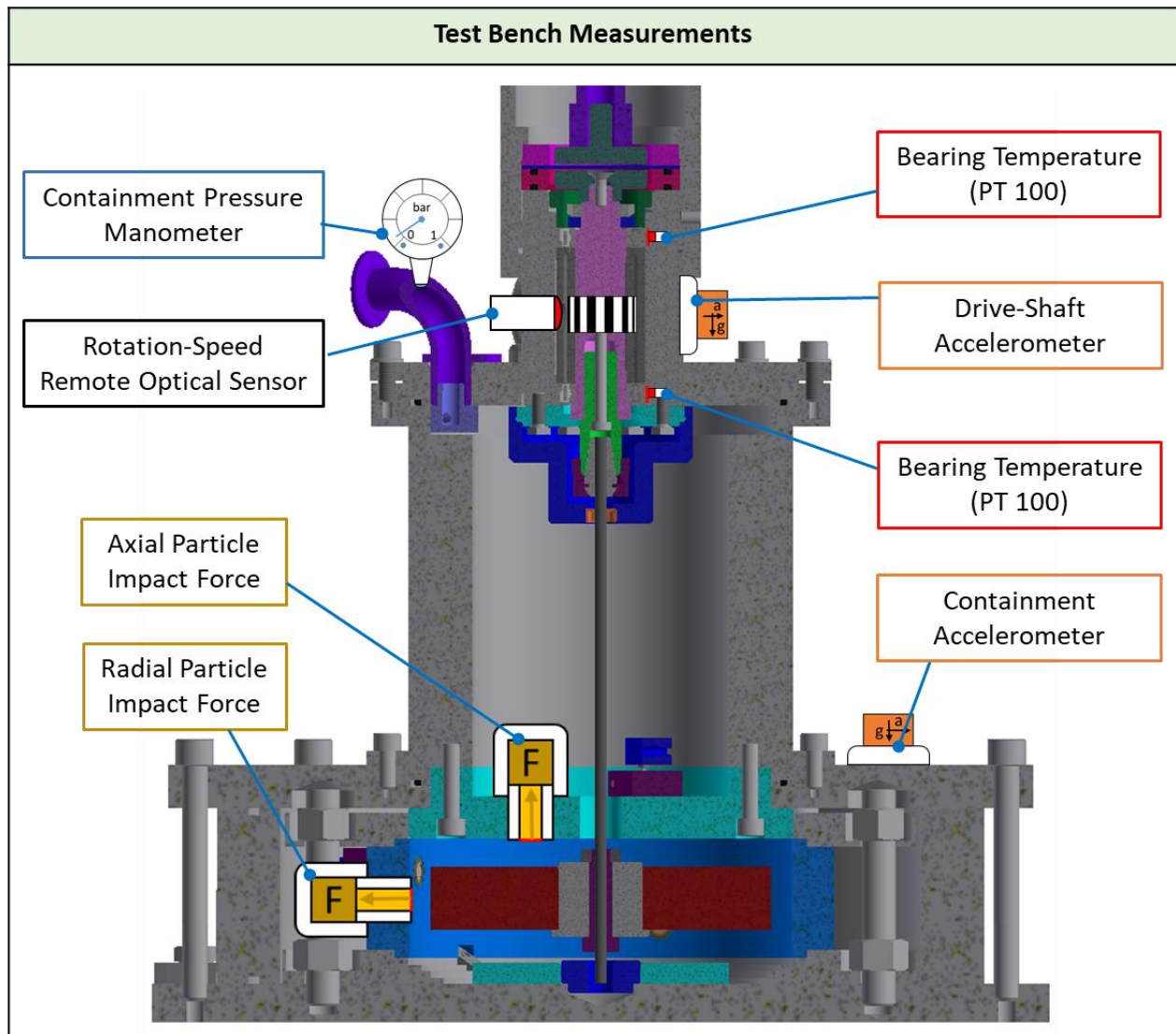


Figure 41: Sensor attachments of the system

6.2.1 Rotational Speed

As a main indicator for the impact related energies, the rotation speed at the moment of burst has to be detected.

The speed was measured using a Remote Optical Sensor (ROS) by *Monarch Instruments*. This sensor emits a visible red LED light, which is reflected by a mark on the outer surface of the drive shaft. Depending on the number of attached marks partitioning the circumference, the counted detection leads to a time averaged rotation speed [4].

Speed Range: 1 – 250,000 rpm (using only one mark)

Power Requirement: 3 – 15 Vdc @ 40 mA

6.2.2 Vacuum Pressure

To lower the air-friction based influences, the containment has to be evacuated.

Therefore, a bourdon tube pressure gauge from the company *VACOM* indicated the generated negative pressure. These types of manometer are used for the measurement of relative pressures. Bourdon tubes are radially formed tubes with an oval cross-section, as illustrated in Figure 42. The pressure of the measuring medium acts on the tube and produces a motion in the non-clamped end of the tube. This motion is the measure of the pressure and is indicated via the movement [19].

Type: RFM-CU-S-0-KF16

Pressure Range: 10 to 1020 mbar

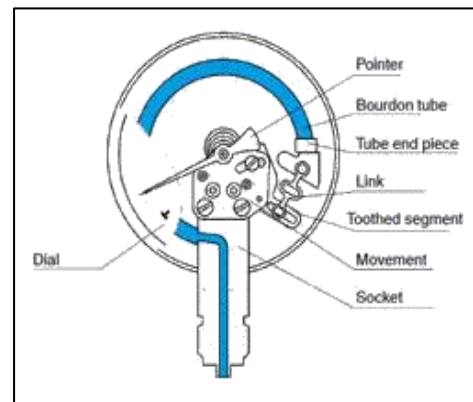


Figure 42: Schematic function of a tube pressure gauge [19]

6.2.3 Acceleration

Radial acceleration values were monitored and recorded at the position of the drive shaft and at the top plate of the main burst chamber. These values were used to estimate radial bearing forces during the operation time. The evaluation of the generated acceleration curves led to the "exact" impact time. In the event that the impact is not clearly evident from the velocity profile (generated by the ROS), this time was used to determine the achieved bursting speed.

The used model, MWS 4301, is an accelerometer based on capacitive technology. It relies on a change in electrical capacitance in response to acceleration. Accelerometers utilize the properties of an opposed plate capacitor for which the distance between the plates varies proportionally to applied acceleration, thus altering capacitance [20] [4].

Range: 5 to 1000g

Power Requirement: 9 to 30 Vdc

6.2.4 Temperature

PT 100 temperature sensors were used to monitor the bearing temperature. If a bearing heats up significantly during the experiment, this is a clear indication that the bearing is not working properly. In order to avoid bearing damage, the temperatures were monitored during the entire operation [4].

PT 100 are platinum resistance thermometers. The principle of operation is to measure the temperature dependent resistance of a platinum element. The used type PT100 has a resistance of 100 ohms at 0 °C and 138.4 ohms at 100 °C.

Type: PTF C (2.0 mm x 2.3 mm)

Temperature range: -50 to 600 °C

Self-heating coefficient in air: 0.5 °C/mW

6.2.5 Particle Impact Pressure

According to chapter 4.3, the developed impact models are relying on a burst observation, where the maximum particle impact forces are measured using distributed hardened steel balls, which indent the surface in case of an impacting force (information from a conversation with FESS specialist *Frank Täubner*). How this experiment exactly was executed and which values were generated is not postulated. Most likely the principle corresponds to the *Brinell Hardness Test*. This test generally uses a steel ball, which is pressed into a surface under a constant load. The diameter of the obtained circular indentation, in combination with the attached force, is related to the hardness of the tested material [21].

The main problem of this measurement principle is that it only records the maximal impact peak. To obtain a time dependent pressure distribution, the idea was to use load cells in combination with an impact receiving cylindrical punch. The measured force compared to the size of the impact surface should lead to the time variable impact pressure. Of course, dynamic effects of fast moving parts (e.g. mass inertia) have to be taken into account to obtain accurate results. Therefore, three different sensors were developed and manufactured, as illustrated in Figure 43. The sensors were not implemented during the held tests series. In further experiments, they should be equally distributed over the circumference of the inner containment ring (to record radial pressure) and to the intermediate top plate (to record axial pressure). To gain experience, according to the burst behavior of the composite.

The further explained CFRP rotor designs, in combination with the inner burst chamber dimensions and the maximum operation speed of 36,000 rpm, lead to an impact pressure of 46 bar in radial and axial direction calculated with the Gas Pressure Model. To increase the probability of reusing the sensor systems, the sensors must be able to withstand twice the calculated pressure. For this purpose, the impact surfaces of the punches were adapted to the capacities of the load cells used. Further design measures and load cell selections are due to the installation space restrictions, which do not allow more than 40 mm radial projection of the screwed-in sensors.

Load Cells:

A load cell is a force sensing module - a carefully designed metal structure, with sensitive elements called "strain gauges" mounted in precise locations on the structure. The further explained load cells are designed to measure a specific force, and ignore other forces being applied. The electrical signal output by the load cell is very small and requires specialized amplification. Load cells are designed to measure force in one direction. They will often measure force in other directions, but the sensor sensitivity will be different, since parts of the load cell operating under compression are now in tension, and vice versa [22].

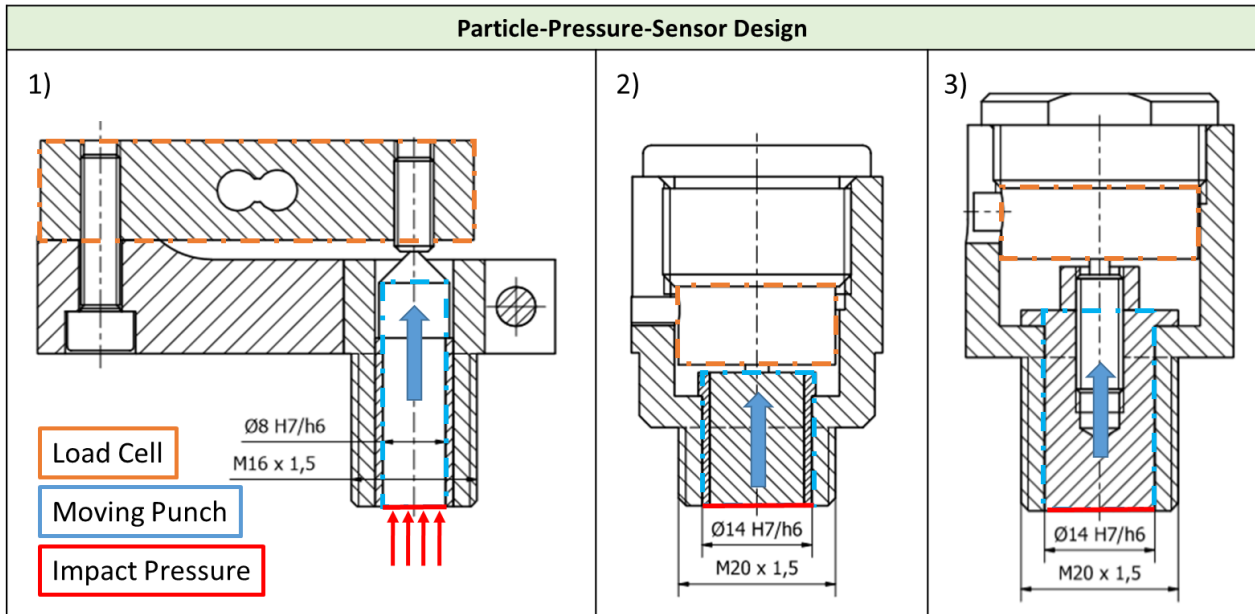


Figure 43: Three different Particle Pressure Sensors: Design and Function

According to Figure 43 the three different sensor types are described below.

1) Single Bending Beam Load Cell

The first Particle Pressure Sensor design uses a single ended bending beam (Figure 43/left). It is mounted by bolting down the end of the load cell where the wires are attached and applying force on the other end in one predetermined direction. Where exactly the force is applied is not critical, as this load cell measures a shearing effect on the beam, not the bending of the beam [22]. Due to a small capacity of only 50 kg, the moving punch has to be relatively thin to reduce the impact surface. Compared to the other two designs, a wide but narrow structure is needed, but the load cells are very cheap and easily available items.

Load Cell Type: CZL635

Capacity: 50 kg

Impact Pressure Maximum: 117 bar (including 20% safety overload)

2) & 3) Disc Load Cell

Both of the other designs (Figure 43/ right and middle) use a disc shaped strain gauge load cell. Different dimensions of the load cells in combination with standard metric thread geometries led to the two different sensor layouts. The principle of both load cells are the same. One end of the cylindrical cells is curved inwards and on the other end, there is an elevation in the form of a button. Force applied to the button causes a change in the measured resistance [23]. Compared to the illustration, the button is facing down. Based on the relatively high capacity of the load cells and the calculated impact pressure, the impact surface is nearly four times bigger than the beam cell construction. This allows the sensor a wider coverage of the inner containment surface by a simultaneous decrease of resolution.

Load Cell Type: 2) TAS606 & 3) CZL204E

Capacity: 200 kg

Impact Pressure Maximum: 153 bar (including 20 % possible overload)

Strain Gauge Attachment on the used Load Cells:

Both load cell types are equipped with four strain gauges. The principle of strain gauges is based on the change in electric resistance due to stretching or compression of an electrical conductor. When the load cells used are loaded, two of the strain gauges are stretched (resistance increase + / Figure 44 orange) and the other two are compressed (resistance decrease - / Figure 44 blue). The resistance change is a measurement of the load F and is measured by a "Wheatstone Measurement Bridge".

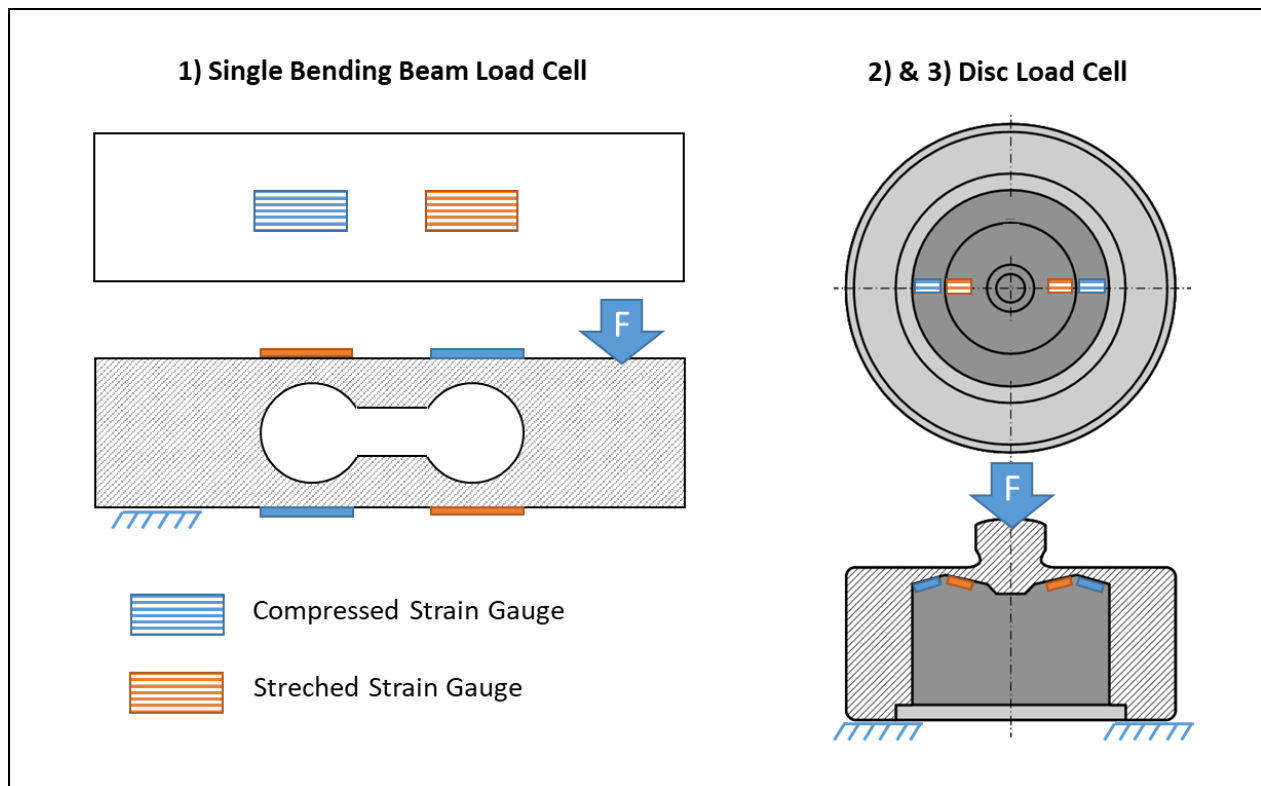


Figure 44: Mounted strain gauges at the single bending beam load cell (left) and the disc load cell (right).

Measuring Principle of the used “Wheatstone Measurement Bridge” [24]:

The bridge circuit was initially used to measure a resistance containing the four resistors R (in our case represented by the strain gauges), which form a voltage divider in pairs and are connected to the bridge supply voltage U_0 .

If resistances are to be measured only near an operating point, a “Deflection Resistance Measuring Bridge” can be used. In this case the bridge is designed to be balanced at a certain value of the resistor of interest. In case of small changes of the resistance value the diagonal voltage U_d displace a value “proportional” to the force.

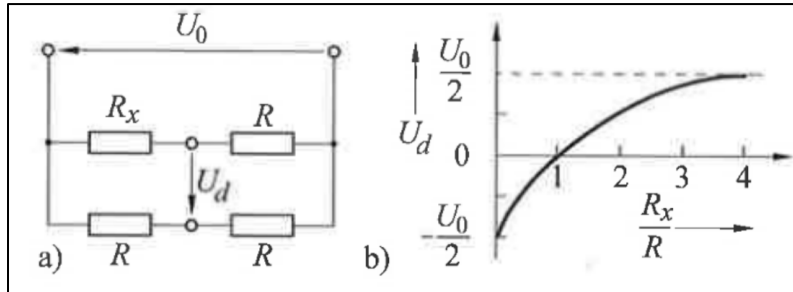


Figure 45: Curve of the diagonal voltage depending on R_x ; a) Circuit, b) Characteristic [24]

The bridge shown in the Figure 45 consists of a variable resistor R_x and three equal resistors R . First of all, it is considered which values the diagonal voltage U_d

$$U_d = U_0 \left(\frac{1}{2} - \frac{R}{R + R_x} \right) = \frac{U_0 R_x - R}{2 R_x + R} \quad (12)$$

assumes as a function of R_x . The following pairs of values result:

$$R_x = 0 : \quad U_d = -\frac{U_0}{2},$$

$$R_x = R : \quad U_d = 0,$$

$$R_x \rightarrow \infty : \quad U_d = +\frac{U_0}{2}.$$

The characteristic curve thus runs curved and the sensitivity dU_d/dR_x is not constant even near the operating point $R_x=R$. However, the height of the diagonal voltage can always be taken as a measure of the detuning of the bridge. It depends not only on the size of the resistors, but also on their arrangement (Figure 46).

In this measurement setup, the bridge contains four equal resistors R_0 and is supplied with a constant voltage U_0 . For the configurations shown in the Figure 46, the size of the resistors concerned is then changed by ΔR and the diagonal voltage that is produced is calculated. The different configurations are called quarter- (Figure 46 a & b), half- (Figure 46 c) and full-bridge (Figure 46 d), depending on whether 1 resistor, 2 or all 4 resistors are variable.

For the bridge of line **a** with $R_1 = R_3 = R_4 = R_0$ and $R_2 = R_0 + \Delta R$ the equation U_d results to

$$U_d = U_0 \frac{(R_0 + \Delta R)R_0 - R_0R_0}{(2R_0 + \Delta R)2R_0} = U_0 \frac{\Delta R}{4R_0 + 2\Delta R}. \quad (13)$$

Here in the denominator ΔR can be neglected compared to R_0 for small resistance changes, so the equation changes to

$$U_d \approx \frac{U_0 \Delta R}{4 R_0}. \quad (14)$$

The diagonal voltage is therefore not exactly proportional to the resistance change ΔR related to the initial resistance R_0 , but only approximately proportional to it.

With the half-bridge arrangement in **c**, no neglect is necessary in the denominator, here the output voltage is exactly linearly proportional to $\Delta R/R_0$.

Arrangement **d** shows the full-bridge made up of four variable resistors with four times the sensitivity of a quarter bridge. The diagonal voltage increases exactly with $\Delta R/R_0$.

Another advantage of the half- and full-bridge over the quarter-bridge is the compensation of temperature-based influences. With increasing temperature, the electrical resistance of the strain gauge increases. When using a half- or full-bridge, these influences can be self-compensated by a special arrangement as shown in Figure 46 c & d.

In our case, a full-bridge with arrangement **d** is used to take advantage of the previously mentioned benefits of high sensitivity, the linear increase of the diagonal voltage with $\Delta R/R_0$ and the self-compensating of temperature influences.

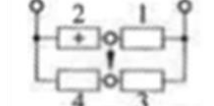
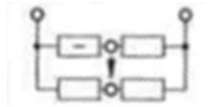
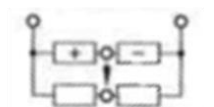
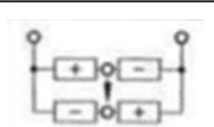
a		$U_d \approx + \frac{U_0 \Delta R}{4 R_0}$
b		$U_d \approx - \frac{U_0 \Delta R}{4 R_0}$
c		$U_d = \frac{U_0 \Delta R}{2 R_0}$
d		$U_d = U_0 \frac{\Delta R}{R_0}$

Figure 46: Diagonal voltage U_d for different bridge arrangements. The unmarked resistors have the value R_0 ; those marked with + have the value $R_0 + \Delta R$ and those marked with - have the value $R_0 - \Delta R$ [24]

6.3 Down-Scaled CFRP Burst Rotor

To gain first experiences with CFRP rotor failure, appropriate rotor-to-fail designs were needed. The main challenge was to create a burst rotor according to the defined test rig restrictions and the composite behavior by implementing the decided manufacturing procedure of the *FlyGrid* prototype. Due to the relatively small dimensions and rotational speeds, it was unlikely to generate an over-speed-failure by a translaminal perpendicular fiber breakage. Therefore, the first attempts relied on radial weakening of the structure by using occurring thermal residual stresses in combination with radial and circumferential notches.

6.3.1 Manufacturing Process and Stress Distribution of the Basic CFRP Rotor Structure

For a better understanding of the further described thermal tension situations, Figure 47 shows the manufacturing procedure of the unnotched burst rotors. Therefore, the same winding mechanism and process was used as for the *FlyGrid* rotor in order to evaluate the process on a small scale and to detect difficulties in advance.

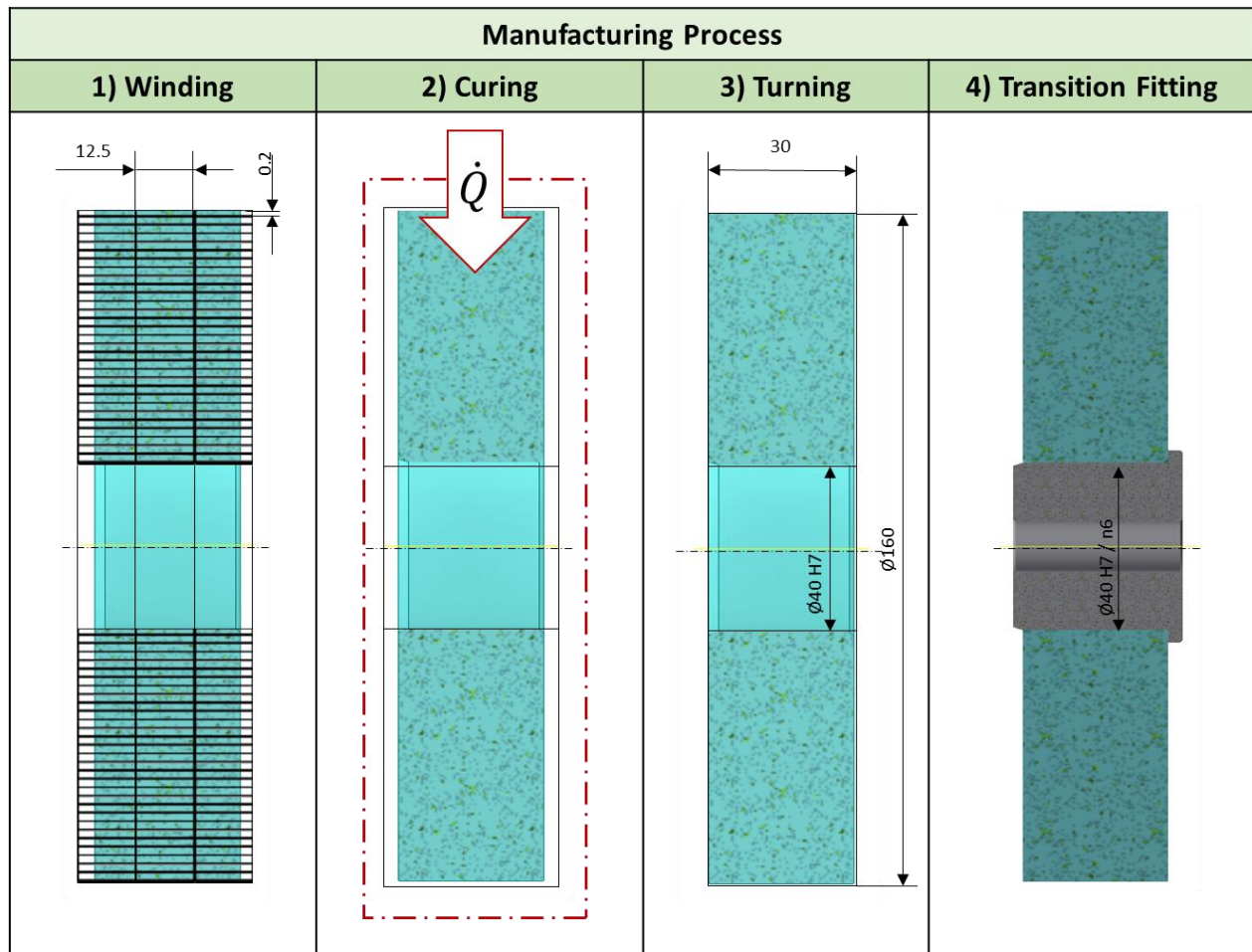


Figure 47: Manufacturing steps and dimensions of the unnotched burst rotor

- 1) **Winding** of the blank Flywheel by using a pin with an outer diameter of 38 mm. As illustrated in Figure 5, the parallel guided *PrePregs* are rolled by thermal-conditioning of their surface under retention of the fiber pre-stressing.

- 2) **Curing** the structure to receive a solid CFRP disc. The maximal rotor height of three times 12.5 mm wide *PrePregs* is based on the exothermic critical polymer mass to surface ratio. The planned press-fit rings of the *FryGrid* rotor have a maximum ring thickness of about 40 mm for the same reasons. A lower radial expansion also causes lower thermal residual stresses.

In the case of the burst rotors, we are taking advantage of these thermal stresses to induce a radial tensile stress that weakens the matrix structure. The curve, shown in Figure 48, is the result of a residual stress calculation, which demonstrates the strong influence of the transversal isotropic composite behavior due to its different thermal expansion coefficients. Transverse isotropy is a special case of orthotropy. The isotropic plane is normal to the longitudinal direction of the fiber. Isotropic means that perpendicular to an isotropic plane there is an infinite amount of planes of symmetry. In this plane there are no more preferred directions. On all sections normal to the isotropic plane, there are the same properties [8]. In the case of a circular wound rotor of unidirectional *PrePregs*, the main directions with different thermal material properties are normally oriented to the translaminar and interlaminar planes.

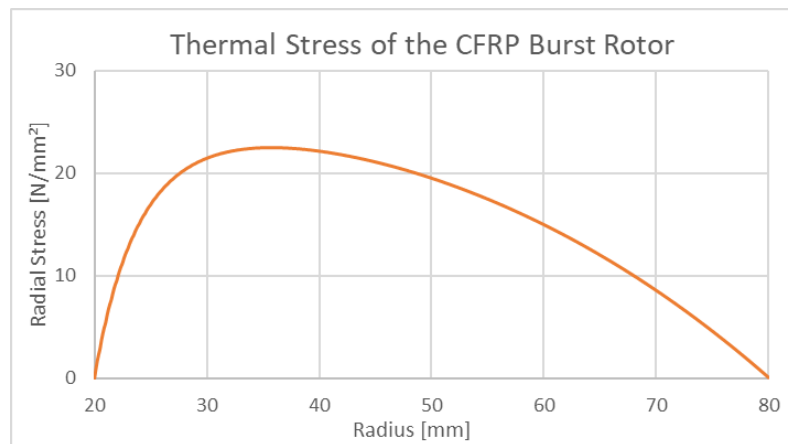


Figure 48: Calculated thermal radial residual stresses of the CFRP burst rotor

- 3) **Turning** of the cured rotor to obtain higher balancing quality and a proper fitting surface for further assembly steps. The final dimensions of the solid wound unidirectional composite ring are 180 mm outer diameter, 40 mm inner diameter and 30 mm height (Figure 49).



Figure 49: Cured and turned CFRP burst rotor

- 4) **Transition Fitting** of the inner aluminum hub. The clutch, which links the flexible shaft to the rotor, has an outer diameter of 12mm. To close the gap between the inner surface of the carbon ring and the outer surface of the clutch, an aluminium hub is pressed and glued in a transition tolerated fit to guarantee the connection even at high rotation speeds, without causing problems according to a strong interference fit.

According to the data sheets of the PrePregs used, the tolerable radial tensile stress limit is 50 MPa. Superimposing the thermal residual stresses with the radial stresses caused by centrifugal forces showed that the influence of the mechanical stresses is too small to reach the limits of the matrix. Figure 50 illustrated the resulting thermal superimposed radial stress levels at 28,000 and 32,000 rpm. The calculated maximum of nearly 30 MPa is far below the 50 MPa limit. Furthermore, the difference between the pure mechanical stresses is very small and leads to the perception that even at higher rotational speeds up to 36,000 rpm, an interlaminar crack cannot be initiated.

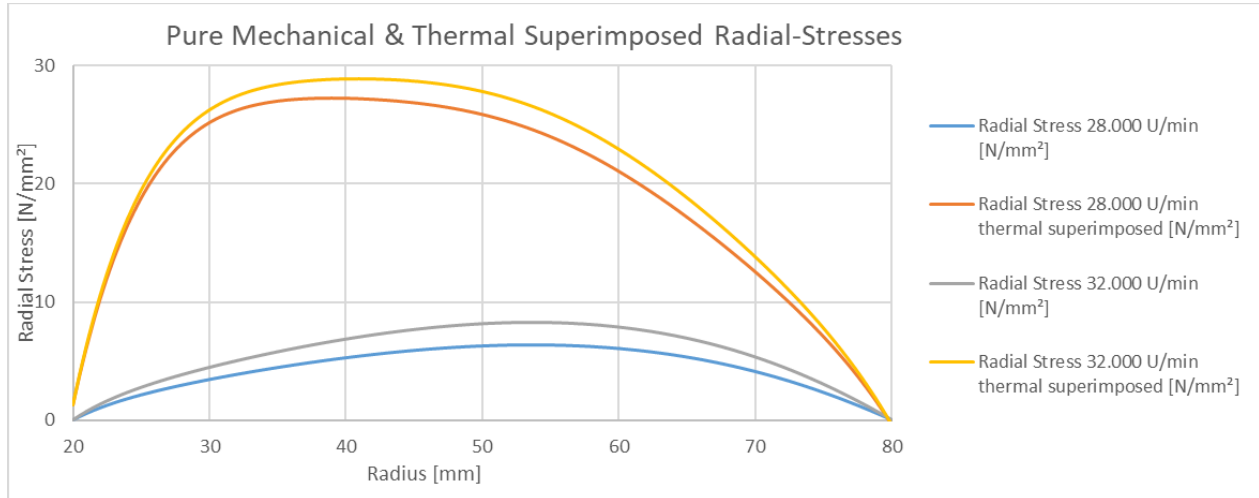


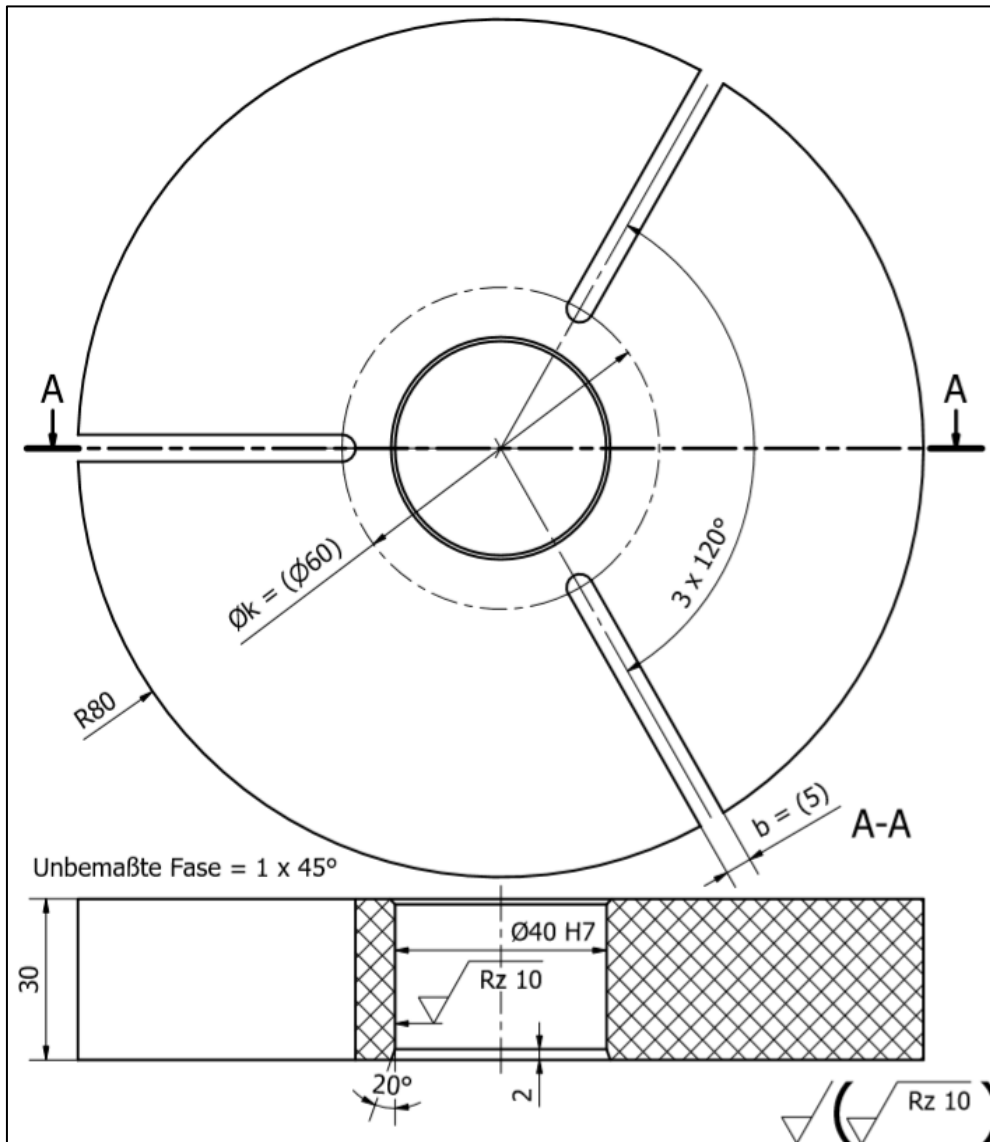
Figure 50: Calculated mechanical and thermal superimposed radial stresses of the CFRP burst rotor

To allow rotor failure at lower rpms, two different types of rotor notching were implemented. Radial slots, which eliminate the influence of the high tensile strength of the fibers and circular notches to reduce the loaded area.

6.3.2 Radially Notched CFRP Burst Rotor

The radially notched design relies on three radial slots equally distributed over the circumference. According to simple analytic calculations of pure mechanical stresses which were explained in Chapter 5.3.1 (Equation (10)), different notch ground diameters $\varnothing k$ will lead to different burst speeds. This calculation neglects thermal residual stresses and was used as a first estimation of the burst speed.

Table 1 lists the manufactured samples with different notch ground diameters $\varnothing k$, compared to Figure 51, and the estimated speed limits.



$\varnothing k$ [mm]	Burst Speed [rpm]
50	~16,000
60	~16,500
70	~17,000

Table 1: Estimated burst speeds

Figure 51: Geometry of the radially notched rotor design

Further investigation of the more complex influence of the notch was carried out using *COMSOL Multiphysics*. The results of a finite element model (FEM) are illustrated in Figure 52. The visualization

shows the occurring von Mises stresses caused by static centrifugal forces at 17,000 rpm with a notch ground diameter of 60 mm.

The radial stress distributions from Figure 52 (left side) are located near the radial notch and the other with 30° offset. It can be seen that the notch causes extreme stress peaks, which should lead to an initial crack and, consequently, to interlaminar crack propagation. Further superimposing of a thermal residual stress curve will not result in accurate conclusions. It is assumed that radial residual stresses are linked to circular compression of the composite. If the circular structure is separated due to one of the slots, the compression at the radial notch surface has to disappear. Therefore, a great part of the residual stresses is released and the critical stress peak shown in Figure 52 cannot be superimposed by the thermal stresses.

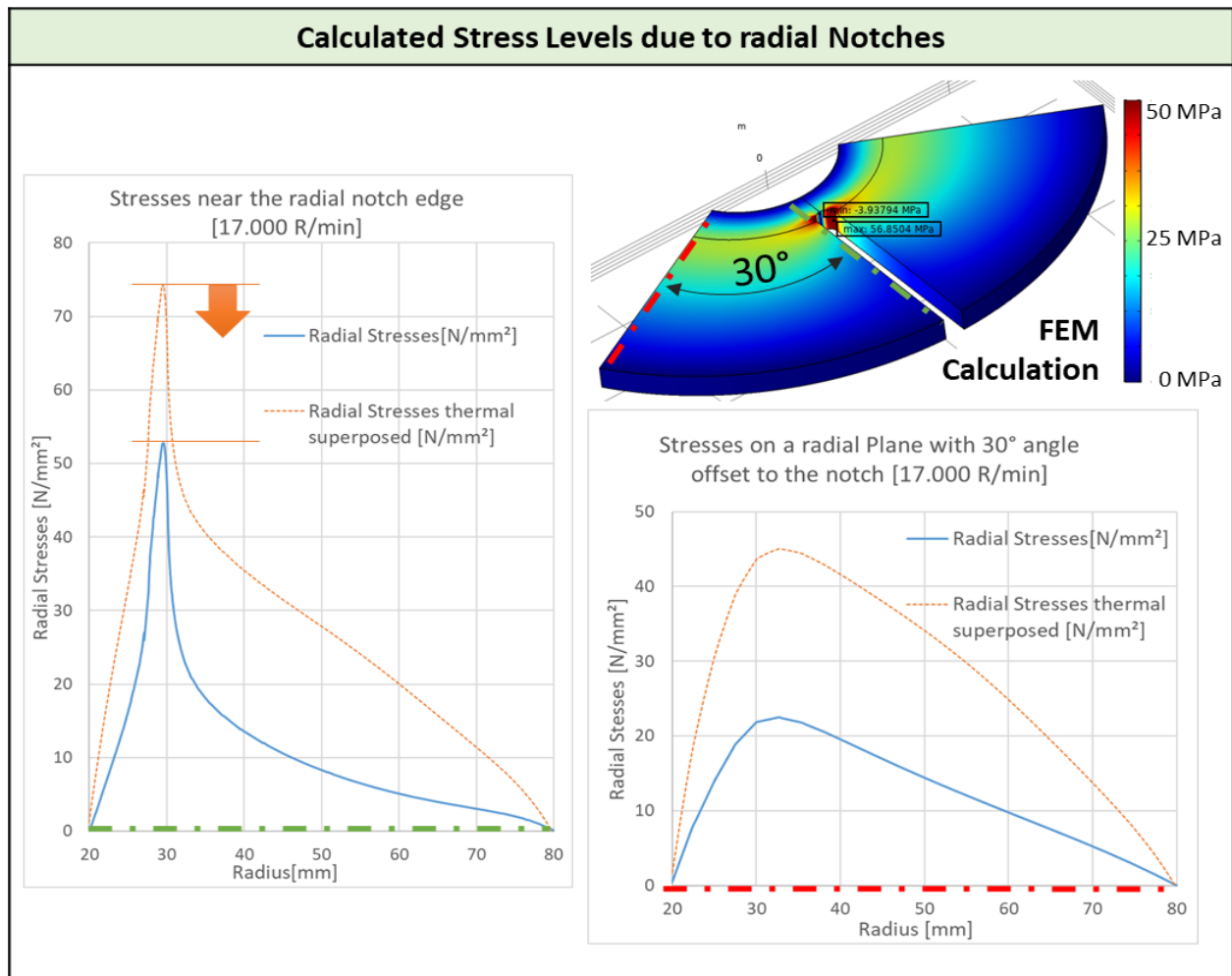


Figure 52: Evaluated radial stresses at 17.000 rpm and a notch depth diameter of 60 mm

6.3.3 Circularly Notched CFRP Burst Rotor

Based on the idea of reducing the radially loaded circular cross-section at $\varnothing k = 100$ mm, the rotor structure was weakened by two circular notches. As illustrated in Figure 53, the notches lead to a symmetric design with a remaining bar thickness of 10 mm. The simulation results graphed in Figure 54 show the stress

peaks, which are caused by adding a mechanical load by rotational speeds of 28,000 rpm to the structure. The thermal residual stresses are directly superimposed and lead to a radial notch edge tensile stress of over 46 MPa. It is assumed that in this case the released residual stresses will further increase the stress peaks. This can be explained by the circular separation of the inner and outer ring section. Due to the milling process, radially pre-tensioned material is removed. This circumstance induces further tension in the remaining "bar structure" and may cause interlaminar cracks without external loads.

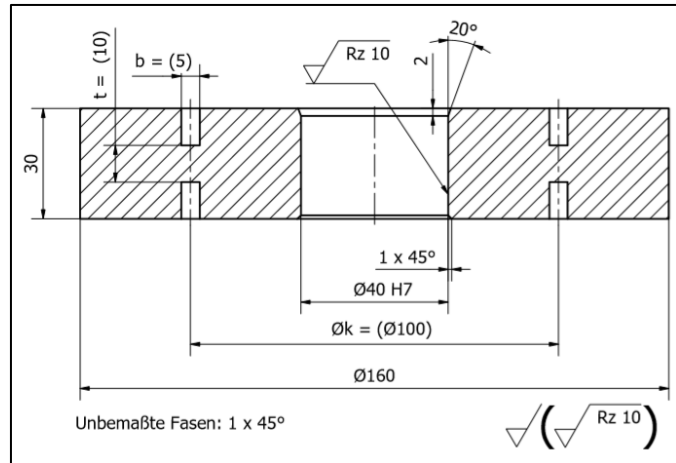


Figure 53: Geometry of the circularly notched rotor

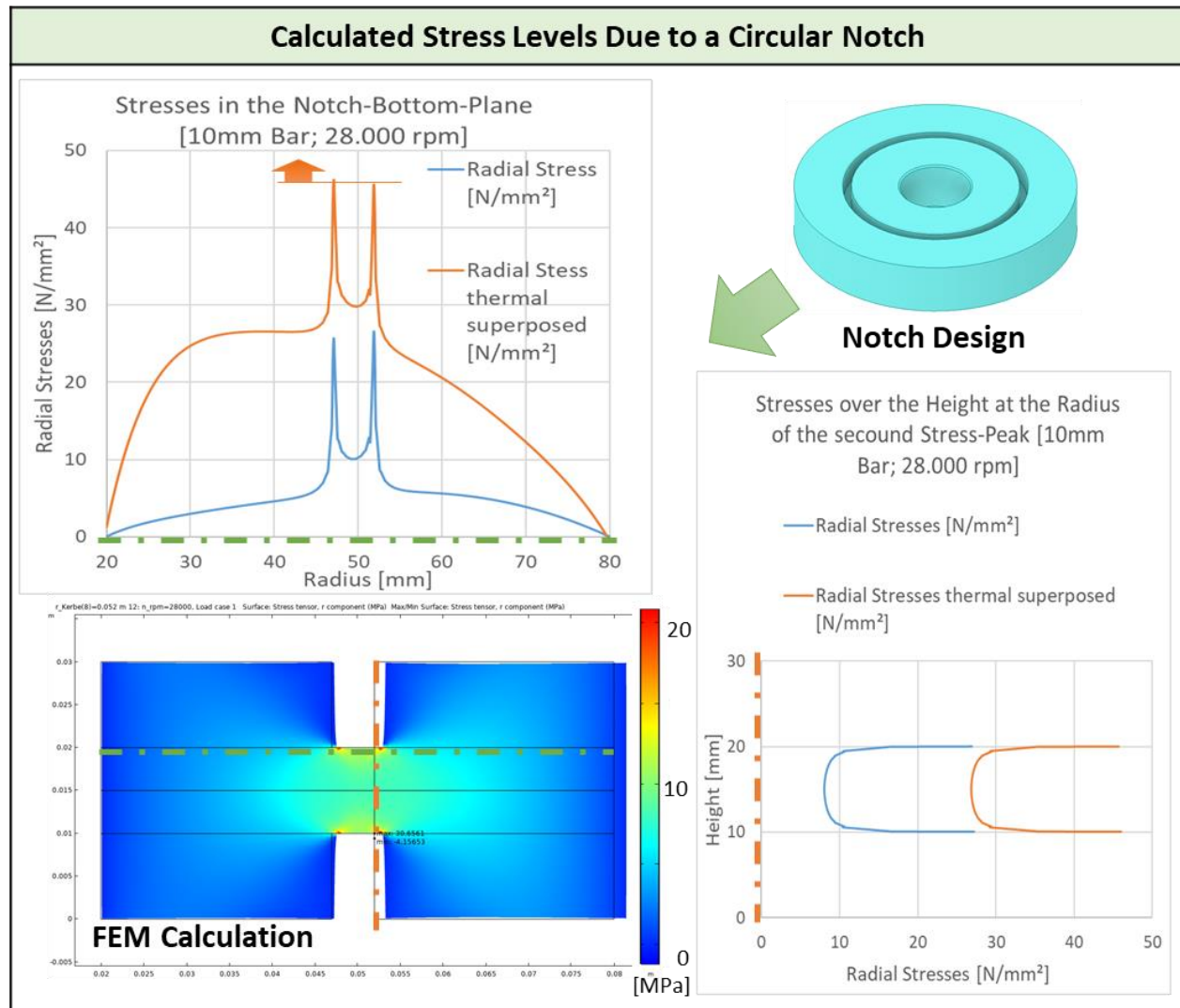


Figure 54: Evaluated radial stresses at 28,000 rpm with a notch diameter ϕ_k of 100 mm and a remaining bar height of 10 mm

6.3.4 Circularly and Radially Notched CFRP Rotor

The circularly and radially notched rotor was based on the previously shown circularly notched rotor design with six additionally milled radial grooves (Figure 55). The specific rotor had one already existing crack along the circular groove, shown in Figure 74. To avoid further propagation of this crack, the three radial notches on each side have an offset of 60° . In contrast to an axial mirrored layout, this measure should strengthen the remaining bar structure and may enable higher rotational speeds. The main idea was to force a horizontal interlaminar shear failure, which releases the six separated segments.

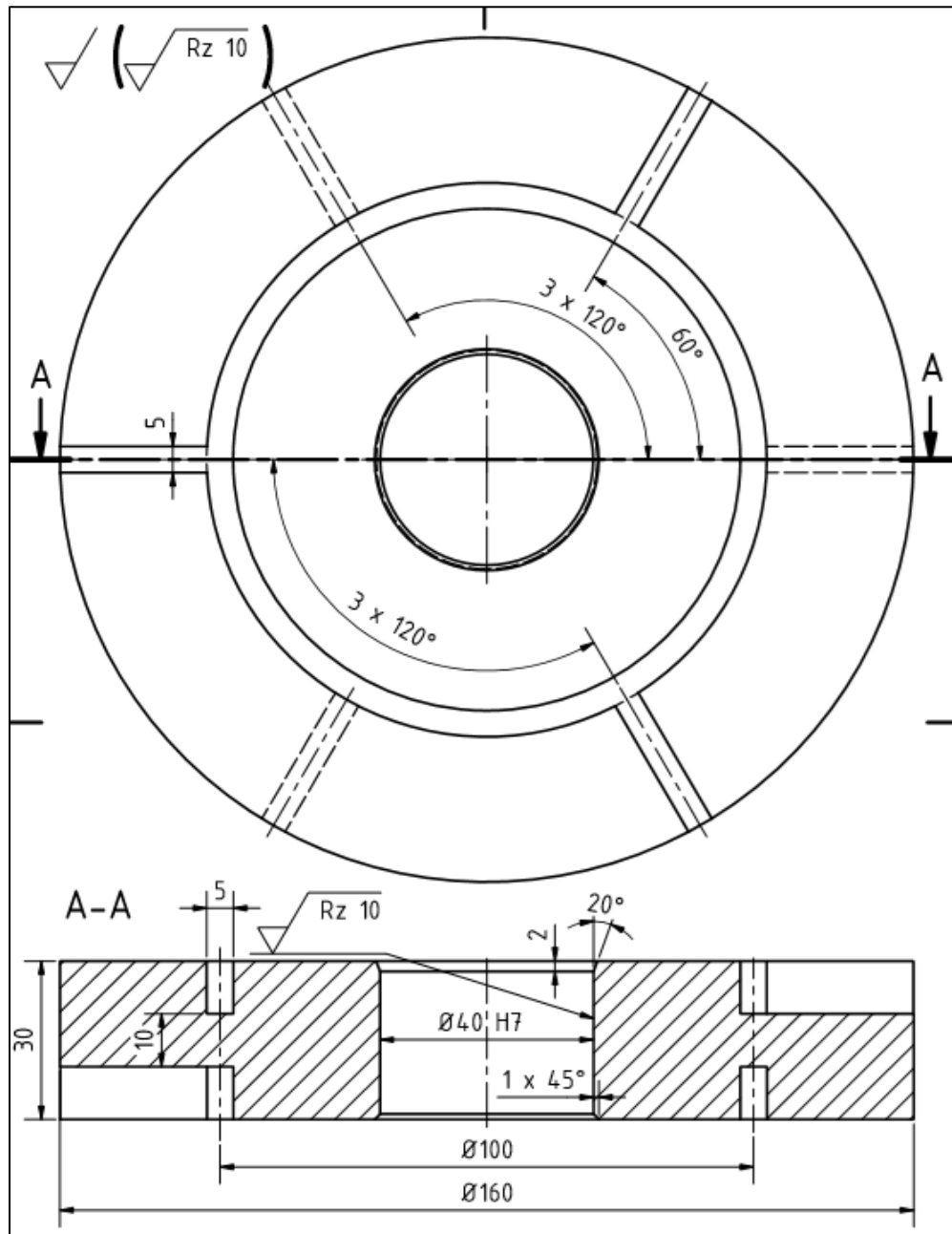


Figure 55: Geometry of the circularly and radially notched rotor

7 Results

7.1 Results of the Empirical Steel Rotor Burst Tests

The goal, as mentioned before, was to find out and establish a relation between the kinetic energy of the rotor fragments and the ability of the containment to absorb this energy [1]. Due to 22 successfully executed burst tests and the previously described observation and measurement methods, it was possible to define the related energy distributions. The following sections a) & b) list the generated results compared to their respective process variations, as is illustrated in Figure 56.

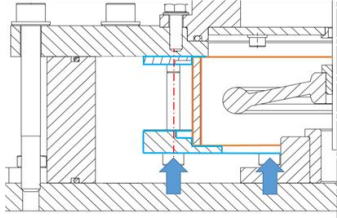
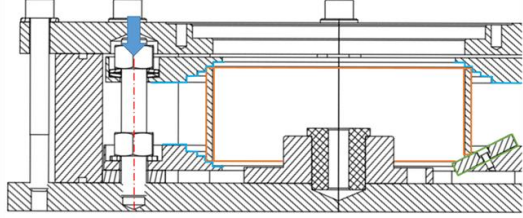


Containment	a)	Containment	b)	
Clamping:	<ul style="list-style-type: none"> Undefined axial pre-stressing Clearance fit on the upper and lower front edge Without anti twist prevention 	Clamping:	<ul style="list-style-type: none"> Defined axial pre-stressing Clearance fit on the upper and lower front edge With anti twist prevention 	
				
Material:	S235JRH	Material:	<ul style="list-style-type: none"> P235GH } → Steel E355 } → Steel S235JRH } → Steel AlMg4.5Mn0.7 → Aluminum X5CrNi18-10 → Stainless Steel 	
Geometry: Cylindrical Ring	<ul style="list-style-type: none"> ∅ 174/180 x 3/4/5/6 x 68 	Geometry: Cylindrical Ring	<ul style="list-style-type: none"> ∅ 168.3/170 x 4/4.5/5/6.3/7/10 x 60 	
Manufacturing:	<ul style="list-style-type: none"> Cut plane sheets Round rolled Welded Turned Clearance fit 	Manufacturing:	Purchased tubes with and without weld <ul style="list-style-type: none"> Cut to length Turned Clearance fit 	
Rotor	Rotor	Rotor	Rotor	
Design:	<ul style="list-style-type: none"> Turned-Milled Structure 		Design:	<ul style="list-style-type: none"> Cast Iron Hand-wheel
Burst Speed:	<ul style="list-style-type: none"> ~ 28,600 rpm 		Burst Speed:	<ul style="list-style-type: none"> 22,300 – 30,700 rpm
				

Figure 56: Variation overview classified by the test series 1-13 a) and 14 -22 b)

a) Test Series 1 to 13

Measured Values:

- Burst speed: Recorded by a revolution counter positioned at the drive shaft (Figure 41)
- Fragment mass: To obtain the angular burst fragment size (Explained in Chapter 5.3.2)
- Fracture Energy: By counting the generated fracture surface, using the notch impact energy
- Analytically measured deformation: As explained in Section 5.4

Clamping:

As shown in Figure 57, the tested containments were positioned by a stepped clamping ring and pressed against the top plate of the burst chamber. During the deformation process, the height of the burst ring changes. The design a) was very stiff and the clamping force was not defined. To avoid this problem, several enhancements were made, as shown in Figure 60.

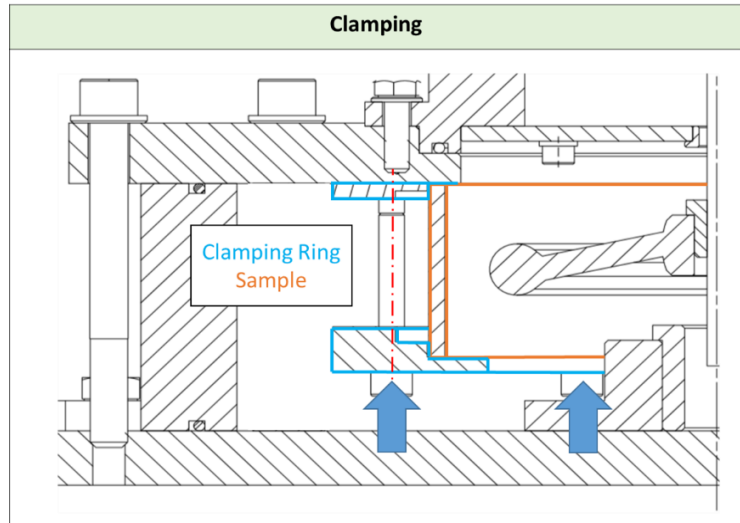


Figure 57: Clamping situation used for the first 13 samples

Containment Sample Design:

The first 13 containment samples were made of rolled metal sheets with an axial weld. Due to inaccurate welding quality, some of the deformed containment exhibited cracks in the heat affected zone, which often led to complete housing failures (Figure 58). As a consequence, seamless tubes were used instead of the welded samples.

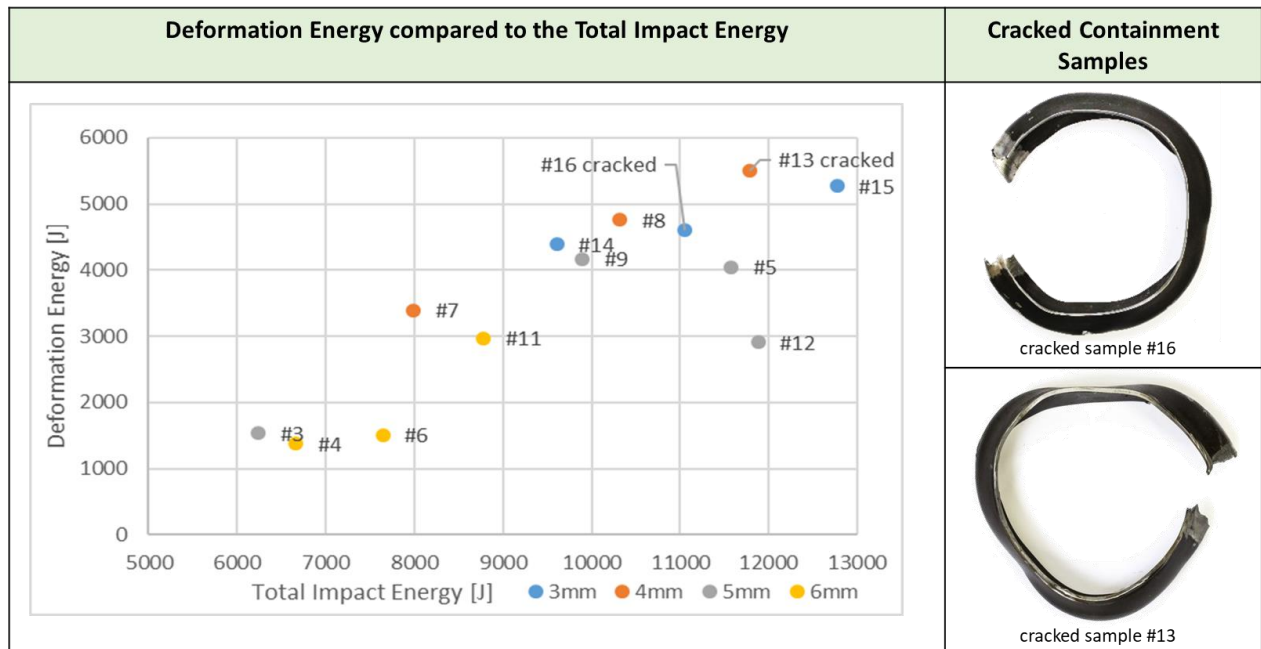
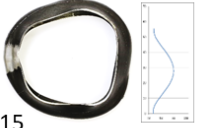
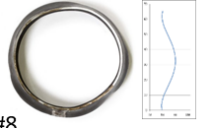
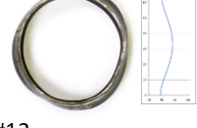



Figure 58: Overview of the measured deformation Energy (left) and two cracked samples (right)

Table 2: Measured and calculated Energies of the first 13 samples

No.:	Docum. Assignment	Containment [mm]	Flywheel type	Burst-speed [rpm]	Kinatic Energy of the Fragments [J]				Fracture Energy [J]	Impact Energy [J]	De-formation Energy [J]	Illustration
					Translatic		Rotational	Total				
					Radial	Tangential						
1	#14	ø174 x 3 x 68 S235JRH	HW ¹	26479	2824	4974	1972	9770	159	9611	4391	
2	#16			28644	3404	6249	1576	11229	175	11054	4612	
3	#15			30739	3728	6553	2648	12929	159	12770	5272	
4	#7	ø180 x 4 x 68 S235JRH	HW ¹	24811	2710	4269	1212	8191	207	7984	3393	
5	#8			28210	3707	6139	680	10526	207	10319	4758	
6	#13		T&MFW ²	28615	3655	4107	4025	11787		11787	5507	
7	#3	ø180 x 5 x 68 S235JRH	HW ¹	22338	2037	3434	978	6449	207	6242	1530	
8	#9			27682	3389	5998	748	10135	239	9896	4172	
9	#12		T&MFW ²	28761	3544	4280	4057	11881		11881	2908	
10	#5		HW ¹	29431	3743	6351	1687	11781	207	11574	4043	
11	#4	ø180 x 6 x 68 S235JRH	HW ¹	22630	2077	3790	1034	6901	239	6662	1378	
12	#6			24460	2234	3875	1773	7882	239	7643	1507	
13	#11		T&MFW ²	28638	368	4390	4022	8780		8780	2968	

1... Cast Iron Handwheel

2... Turned and Milled Flywheel

Table 2 shows the measured burst speeds and the calculated energy values of the first 13 tests, which were used to generate average energy balances according to the respective containment thicknesses, as is illustrated in Figure 59. Therefore, the kinetic energy of the flywheel fragments was used as 100% impact input. Depending on the previously explained observations, this impact splits up into three main parts of the kinematic behavior. These energies are based on a radial and tangential translation relative to the containment and a rotational share. Due to the system boundaries, the whole kinetic energy input has to be absorbed by plastic/elastic deformation, crack propagation and must be transformed into heat, based on friction. To specify the energy share dissipated in heat, the containments of the further test series were equipped with temperature sensors.

Observations (Figure 59):

The share of fracture energy of the cast iron hand-wheel increases with the thickness of the containment. This phenomenon can be described by a lack of deformation capacity due to a stiffer containment behavior. That means that a thin 3 mm housing reduces the speed of the impacting pieces by a much larger deformation. It then absorbs the kinetic energy without forcing the fragment dissipating its energy through additional fractures during rotor impact.

The proportionately reduced deformation energy share of a thicker containment is related to an increased internal stress state of the structure. It is assumed that in each deformed steel ring, (due to the three-dimensional stress state) a certain residual stress remains after impact. This depends strongly on the wall thickness. The thicker the wall of the containment, the more residual tension occurs. As a first

approximation, recommended by experienced researchers in the field of *Strength-of-Material* at the *Technical University of Graz*, this share is about ten percent of the entire deformation energy. Maybe a explicit numerical simulation can solve this problem as it has been made comparing to section 7.3. Within this thesis, these simulations were not used to answer energy related questions, but rather to recreate the visual appearance of the conducted tests.

The different proportions of translational (tangential and radial) to rotatory energy can be described by the different fragment kinematics. Observing the milled turned rotor, the segments have a large section angle and a higher radial extent. According to Figure 70 (Chapter 7.4), this signifies a greater amount of rotational energy. In comparison, the released handwheel debris have a smaller angular size and, therefore, contain a higher amount of translational energy. As shown in Figure 68 (Chapter 7.4), higher speeds force the middle section between two spokes to crack in a free moving stage before the actual impact, due to the acting centrifugal forces. This circumstance reduces the rotatory energy at higher burst speeds.

The proportions of translational to rotatory energy further illustrate the connection between the radial energy entry and the deformation work of the containment. As mentioned in Figure 56, the clamping situation does not prevent slippage of the ring, which enables the containment to reduce the tangential energy component by an induced spin of the entire structure. This advantage can be used for special safety housing designs (called Rotating Liner), but in this case it is an additional variable that influences the measurement.

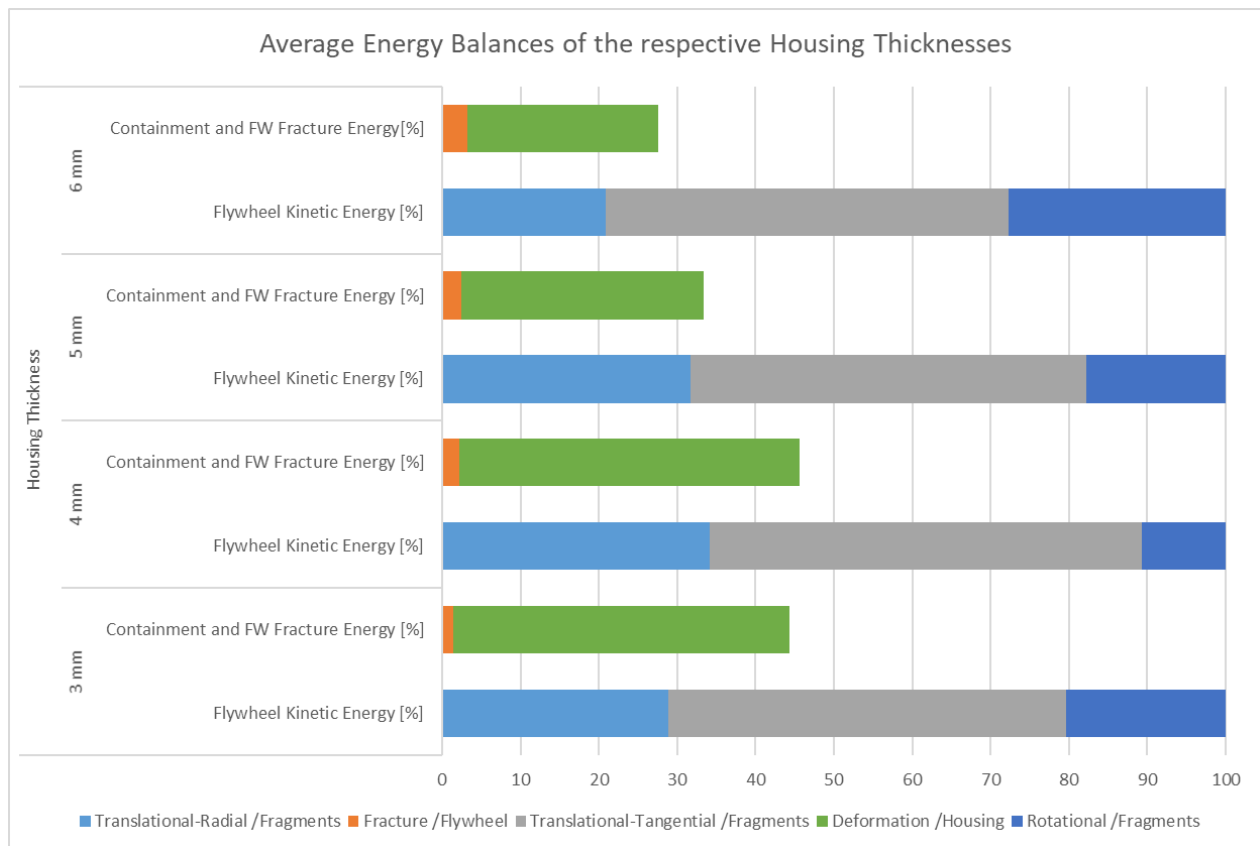


Figure 59: Average energy balance based on the first 13 intact containment samples

b) Test Series 14 to 22

Measured Values:

- Burst speed: Recorded by a revolution counter positioned at the drive shaft (Figure 41) to obtain the rotor's kinetic energy at the moment of failure
- Fracture Energy: By counting the generated fracture surfaces, using the notch impact energy
- Numeric evaluated deformation: As explained in Section 5.4 / 1.
- Containment temperature to determine the thermal energy: Compare Section 5.4 / 2.

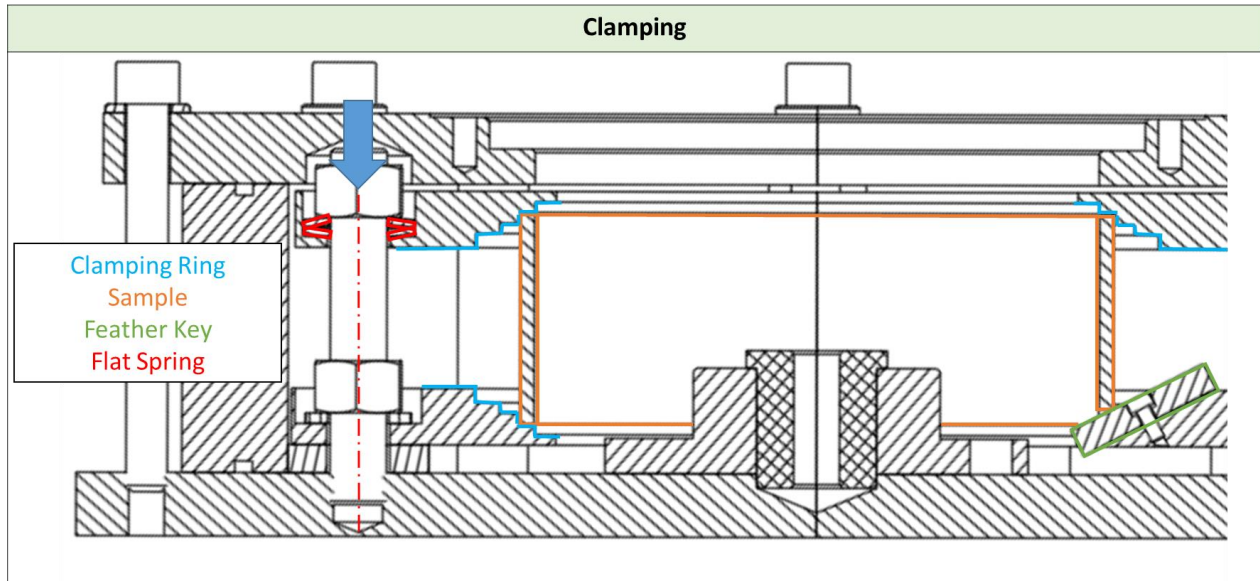


Figure 60: Improved clamping design used for the samples 16 to 24

Clamping:

To realize a more defined clamping situation, two main design changes were implemented:

The first precaution relies on a possible axial movement of the fixture by a flat spring pre-stressed situation by two guide pins and four threaded bars with an adjustable nut, shown in Figure 60. This design allows the tested ring to extend and reduce its height during the deformation process, without loss of axial pressure.




The second change is based on a twist-prevention, realized by two feather keys mounted to the lower clamping ring. This layout also permits the implementation of various temperature sensors at the outer circumference of the tested ring, to detect the generated heat dissipation. Rotation of the tested ring must be prevented as too much angular displacement could destroy the installed wiring harness of the sensors.

Containment Sample Design:

To avoid further containment errors due to poorly made welds (compared to Figure 58), the ring production was replaced by off-the-shelf tubes. During the following test series, three different materials (Aluminum, Stainless Steel and Steel) with variable thicknesses were tested.

Table 3 lists the evaluated and measured values, which were generated by implementing the previously explained changes to the burst chamber. The burst tests are assigned to the tested material and to the increase of containment thickness.

Table 3: Measured and calculated values of the test series 14 to 22

No.:	Docum. Assignment:	Containment [mm]	Flywheel	Burst-speed [rpm]	Kinatic Energy of the Fragments [J]	Fracture Energy [J]	Thermal Energy [J]	De-formation Energy [J]	Illustartion
14	#003	ø168.3 x 4 x 60 S235JRH	HW ¹	25700	9384	175	3729	5452	
15	#001	ø168.3 x 4,5 x 60 P235GH		27500	10740	143	5721	655	
16	#002	ø168.3 x 6,3 x 60 S355J2H		29680	11600	239	5930	3373	
17	#004	ø168.3 x 4 x 60 X5CrNi18-10	HW ¹	27450	10710	159	5129	1187	
18	#005	ø168.3 x 5 x 60 X5CrNi18-10		27720	10920	175	4413	-1364	
19	#006	ø168.3 x 7 x 60 X5CrNi18-10		31050	13650	254	7732	-380	
20	#009	ø170 x 4.7 x 60 AlMg4.5Mn0.7	HW ¹	30680	13370	239			
21	#007	ø170 x 10 x 60 AlMg4.5Mn0.7		30520	13230	191	6284	-751	
22	#008	ø170 x 10 x 60 AlMg4.5Mn0.7		27525	10770	223	4629	-835	

1... Cast Iron Handwheel

The energy balances, shown in Figure 61, represent the perceptually allocated shares of energy. Therefore, the deformation and the thermal energy are connected to the containment and the fracture energy is connected to the brittleness of the burst rotor.

Test #009 has not been evaluated due to its complete destruction that damaged the mounted temperature sensors at the circumference. This test served for further material parametrizations and failure mode evaluations of the explicit simulations, which are described in section 7.3.2.

Observations Figure 61:

Compared to the test series 1 – 13 (Figure 59), the generated values for the deformation energy of the test series 14 - 22 (Figure 61) vary extremely. These results can be caused by two main evaluation inaccuracies of the 3D scans.

- 1) In contrast to the analytical method, there was a lack of distinction between the elongated and the compressed zones of the deformed ring. The measurement was based on surface enlargement. Due to compressed zones, the evaluated surface adds a negative value to the

observed surface and causes a reduction of the average elongation. Adding this distinction to the simplification to describe the three-dimensional stress state by a one-dimensional tension test, the values will increase.

- 2) The numerical examination was supposed to be more accurate than the analytical one, but the results, compared to #005 to #009, show a “negative deformation”. This may be because the resolution of the scans was too low, or the assumption of the generated face fragments led to incorrect results.

The thermal dissipation, as shown in Figure 61 obtains the greatest amount of induced energy. Every occurring temperature rise relies on friction processes. Most of the heat will be generated due to surface-to-surface friction between the moving fragments and the containment. The second part is linked to internal atomic friction, a characteristic to every occurring deformation process. Based on the brittle fracture behavior of the hand wheel compared to the ductile material behavior of the tested containments, the biggest amount of this heat is assigned to the ring deformation.

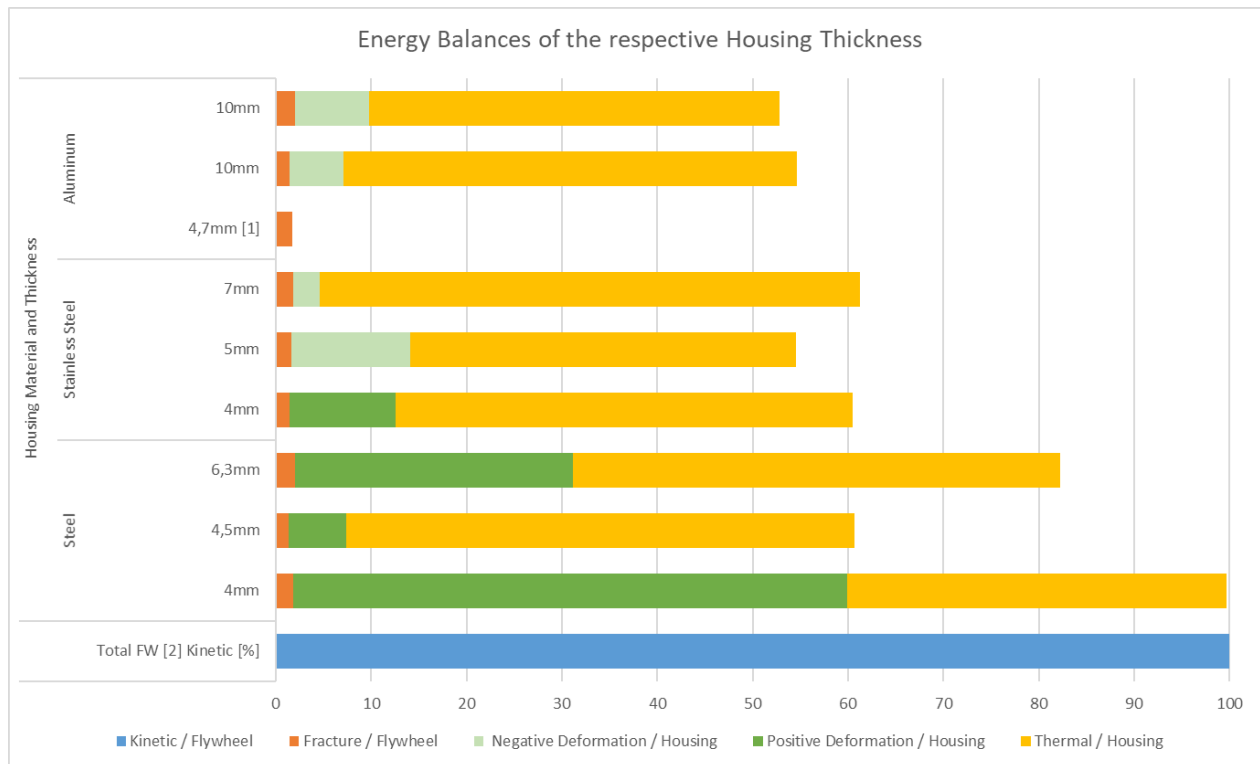


Figure 61: Energy balances of the tested containments No. 14 - 22 compared to 100% of kinetic input of the rotor

[1]... Completely destroyed

[2]... Flywheel

7.2 Results of the Analytical Calculation Method for Steel Burst Containments

Impulse method by *Genta*:

The consideration refers to a detaching fragment and its effect on the containment ring. The calculation assumes an inelastic radial impact between the fragment and the containment wall segment. The resulting impulse is calculated from the geometric relation, which is shown in Figure 62. It is further assumed that the tangential translation of the fragments produces a centrifugal pressure distributed over the circumference of the containment.

The resulting force of the impulse and the centrifugal pressure deforms the housing. This radial displacement induces a tangential stress in the containment, which needs to withstand the used material [17].

All assumptions require idealized rigid bodies. This means that the calculation does not consider an uneven structured deformation. The calculated stress must not exceed the tensile strength of the containment ring material.

Compared to the real world tests, this method leads to a highly conservative layout. According to the calculation, every tested containment should have failed. The boundary conditions and simplifications assumed by *Genta* would lead to enormous **under sizing of the containment rings by factors of 17 to 28**.

“Impact Time” Method by *NASA*:

The design is related to the total stored energy of the fragments. Therefore, the whole kinetic energy of the flywheel is calculated and subsequently the fragment energy is identified by the angular fracture size. Each released fragment has a certain amount of translational and rotational energy (Relations shown in Figure 70). According to *NASA*, these shares are not taken in account. It is assumed that the total kinetic energy is transformed into translational energy. Based on this simplification, fictive speeds of the fragments are calculated. This movement is oriented in radial direction to the inner containment wall. Using an assumed “impact time”, in which the containment needs to adsorb the virtual translation of the fragment, an impact force is calculated. The resulting wall pressure and the induced containment stresses are then compared to the material properties [25].

Based on the test series, it was possible to replace the assumptions for the impact time by evaluated values. Figure 63 shows a tangential cross section of a deformed containment. The measured radial displacement compared to the real radial translation of the fragment leads to a simplified “impact time”, the time a fragment needs to decelerate when hitting the containment wall.

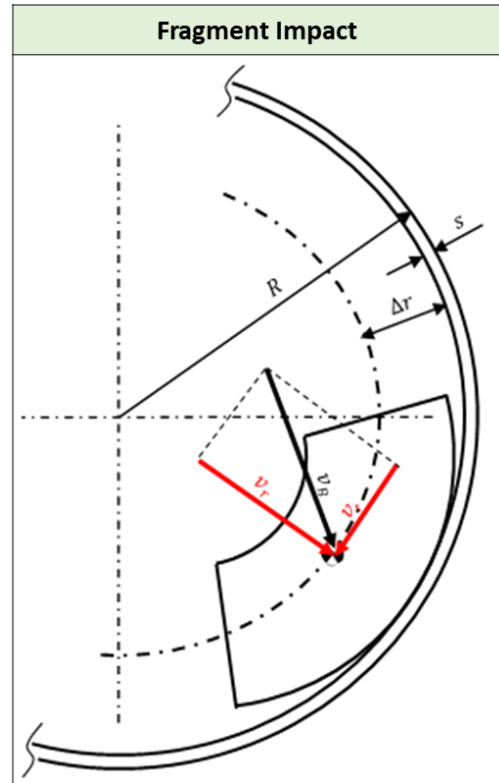


Figure 62: Radial and tangential velocity at the fragment impact

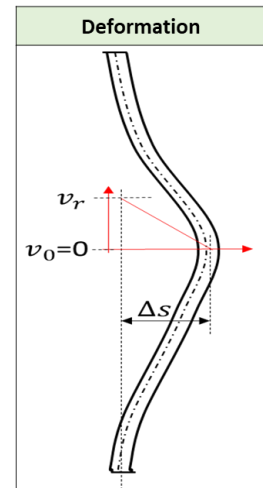


Figure 63: Deformation of the containment and the simplified distribution of the radial speed

To obtain these values it was important to allocate the fractures to a certain impact. This was done so by color coded burst rotors. For this purpose, a color point was set every 120 degrees on the circumference of the rotor. After the bursting process, an abrasion analysis was carried out to assign the color abrasion to the individual fracture segments and the related deformation Δs .

Following the calculation by implementing the measured values of fragment sizes and deformations would mean an **under sizing of the tested containments by factors of 11 to 32.**

The simplifications, which are made by *NASA*, differ from the actual complex physical behavior of the structure and result in similar oversizing as the method by *Genta*.

7.3 Simulation Results of the Steel Rotor Burst Containments

The simulations serve to map the observations numerically and, furthermore, to calculate more complicated structures. The goal is to find appropriate material data and failure modes to describe the used materials, which are relevant to design and test a layout of a proper safety containment for the planned *FlyGrid* prototype.

All simulations were executed with *ABAQUS Explicit Dynamics*. The following chapters describe two implemented failure modes, the *Johnson Cook* and the Shear Failure, that led to satisfying results. At this stage of the investigation, no stress-related results were considered, which would complement the observations in section 7.1.

7.3.1 Johnson Cook Results

In industrial practice, the *Johnson Cook* material and damage model is extensively incorporated into most of the available finite element tools to conduct metal forming simulations because of its ability to predict the model parameters with “less” effort [26]. The inclusion of high velocity impact dynamics in engineering practice allows analysts to account for the effects of penetration fragments, accidental loads, and collisions. Moreover, it allows for a more thorough design of lightweight protective structures for civil and military use [27].

The constitutive model used in the simulations account for the effects of strain, strain rate and temperature on the material behavior [27]. Related to generally valid fast forming processes for most metallic materials, a high strain rate causes a strain hardening, which results in a positive offset of the load-elongation curve to higher stress levels. In contrast to occurring thermal dissipation, induced by fast deformation processes and caused by face-to-face friction, which reduces the stress levels by temperature softening.

Figure 64 schematically illustrates the influence of induced temperature and rising strain rates, according to a quasi-static stress strain curve for ductile materials. Actually, the real behavior is not that simple. Therefore, material characterization is a highly experimental procedure and strongly depends on the application. In other words, the parameters, compared to the literature in Table 4 are specifically trimmed to the respective problems of the according research.

The applied flow stress model can be expressed as:

$$\sigma = (A + B\varepsilon^n)(1 + C * \ln\dot{\varepsilon}^*) * (1 - T^{*m}) \quad (15)$$

where σ is the equivalent stress and A, B, n, C and m are explicit tested material specific parameters.

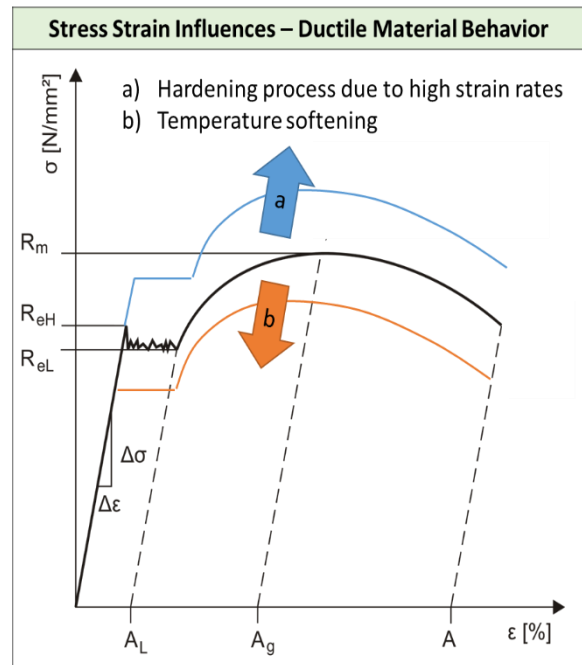


Figure 64: Schematic influence of high strain rates and rised temperatures

Due to an implemented failure model, which is related to the iteratively adjusted “fracture strain constants” (D_{1-5}), the executed simulation enables the stressed and deformed elements to erase their boundaries. Based on according theories, the adapted constants led to different failure behaviors [28]. As a first attempt, the executed tests were reconstructed simulatively by implementing existing parameters, which are illustrated in Table 4.

Table 4: Johnson Cook parameterization of different materials

Material:		Mild Steel [29]	IN718 - solution annealed [28]	Aluminum [30]	C45 (AISI 1045) [26]	Aluminum 6061 - T6 [27]	C30 (Steel 4340) [27]
Modulus of elasticity	E [N/m ²]	203 x 10 ⁹	206 x 10 ⁹	70 x 10 ⁹	210 x 10 ⁹	70 x 10 ⁹	210 x 10 ⁹
Poisson's ratio	ν	0.33	0.29	0.3	0.3	0.3	0.3
Density	ρ [kg/m ³]	7850	8220	2700	7850	2700	7830
Yield stress constant	A [N/m ²]	304.330 x 10 ⁶	450 x 10 ⁶	324 x 10 ⁶	50.103 x 10 ⁶	324.1 x 10 ⁶	792 x 10 ⁶
Strain hardening constant	B [N/m ²]	422.007 x 10 ⁶	1700 x 10 ⁶	114 x 10 ⁶	176.091 x 10 ⁶	113.8 x 10 ⁶	510 x 10 ⁶
	n	0.345	0.65	0.42	0.5176	0.42	0.26
Viscous effect	C	0.0156	0.017	0.0026	0.1056 / 0.095*	0.002	0.014
Thermal softening constant	m	0.87	1.30	0	0.5655 / 0.6622*	1.34	1.03
Reference strain rate	ϵ_{Dot_0} [1/s]	0.0001	0.001	1	1	1	1
Melting temperature	θ_{melt} [K]	1800	1570	930	1720	925	1793
Transition temperature	$\theta_{transition}$ [K]	293	300	293	300	293.2	293.2
Fracture strain constant	D ₁	0.1152	0	-0.77	0.025 / 0.04**	-0.77	0.05
	D ₂	1.0116	0.66	1.45	16.93 / 1.519**	1.45	3.44
	D ₃	-1.7684	-0.4	0.47	-14.8 / - 6.905**	0.47	2.12
	D ₄	-0.05279	-0.017	0.001	0.0214 / - 0.023**	0	0.002
	D ₅	0.5262	0	0	0 / 1.302**	1.6	0.61
* optimized; ** Round Bar - / Flat - and Notched Specimens							

Figure 65 shows a fitting *Johnson Cook* model, with an almost matching visual appearance to the real deformation. Particular attention must be paid to the accurately matching deformation of the feather key recess.

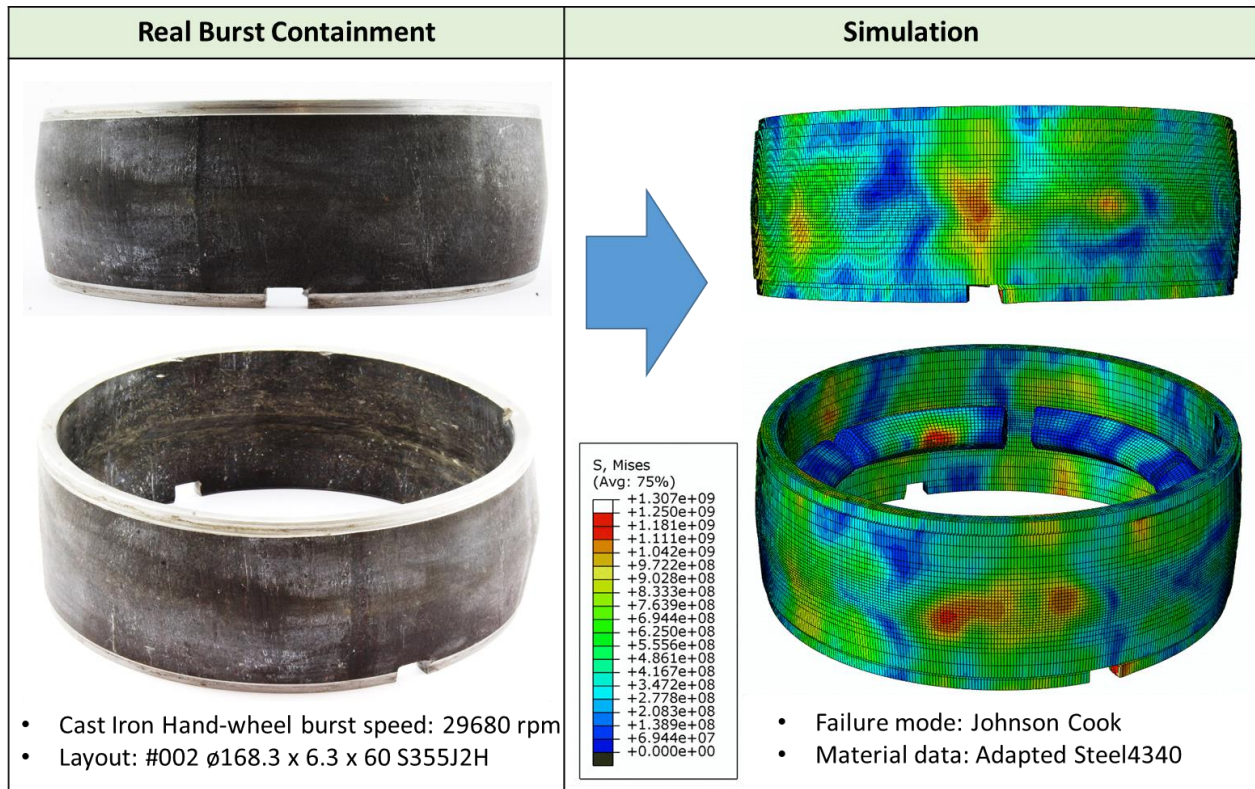


Figure 65: Reproduction of a burst containment by simulation with a *Johnson Cook* failure model

7.3.2 Shear Failure Results

For the reconstruction of highly destroyed containments, the *Johnson Cook* model has not yet performed with accurate outputs. To reduce the complexity of the characterization, a fairly simple “shear failure mode” was implemented. As described previously in section 7.4, this failure mode follows a determined stress-strain curve, as shown in Figure 66. Therefore, general material parameters (e.g. Density 2700 kg/m³, Elastic Young’s Modulus 70,000 MPa, Poisson’s Rate 0.3) for the deformed aluminum ring were determined. A simplified plastic material behavior, compared to Figure 66, in combination with a programmed failure strain, defines the occurring deformation of the elements, until it erases their boundaries.

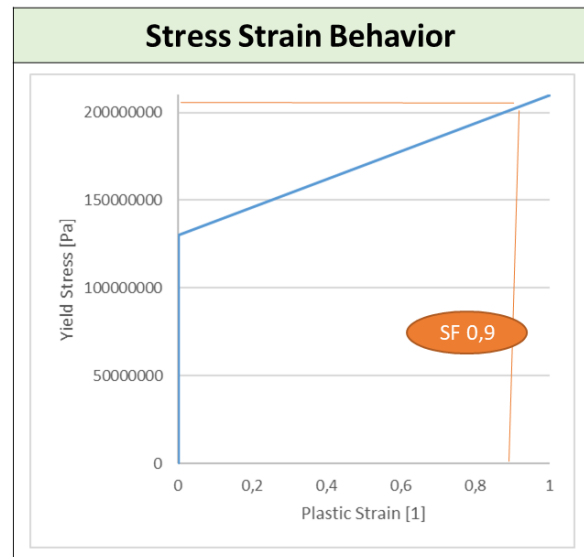


Figure 66: Implemented Stress Strain Curve of Aluminum

Iterations of the plastic behavior and the strain limitations led to an accurate visual appearance, demonstrated in Figure 67. In this case, the relatively thin aluminum containment did not resist the impact of the burst-rotor.

For future considerations, the bursting speed of the rotor and thus the kinetic energy input, should be reduced until the structure can withstand the load. A comparison with a further test series would contribute to a better verification of the parameters.

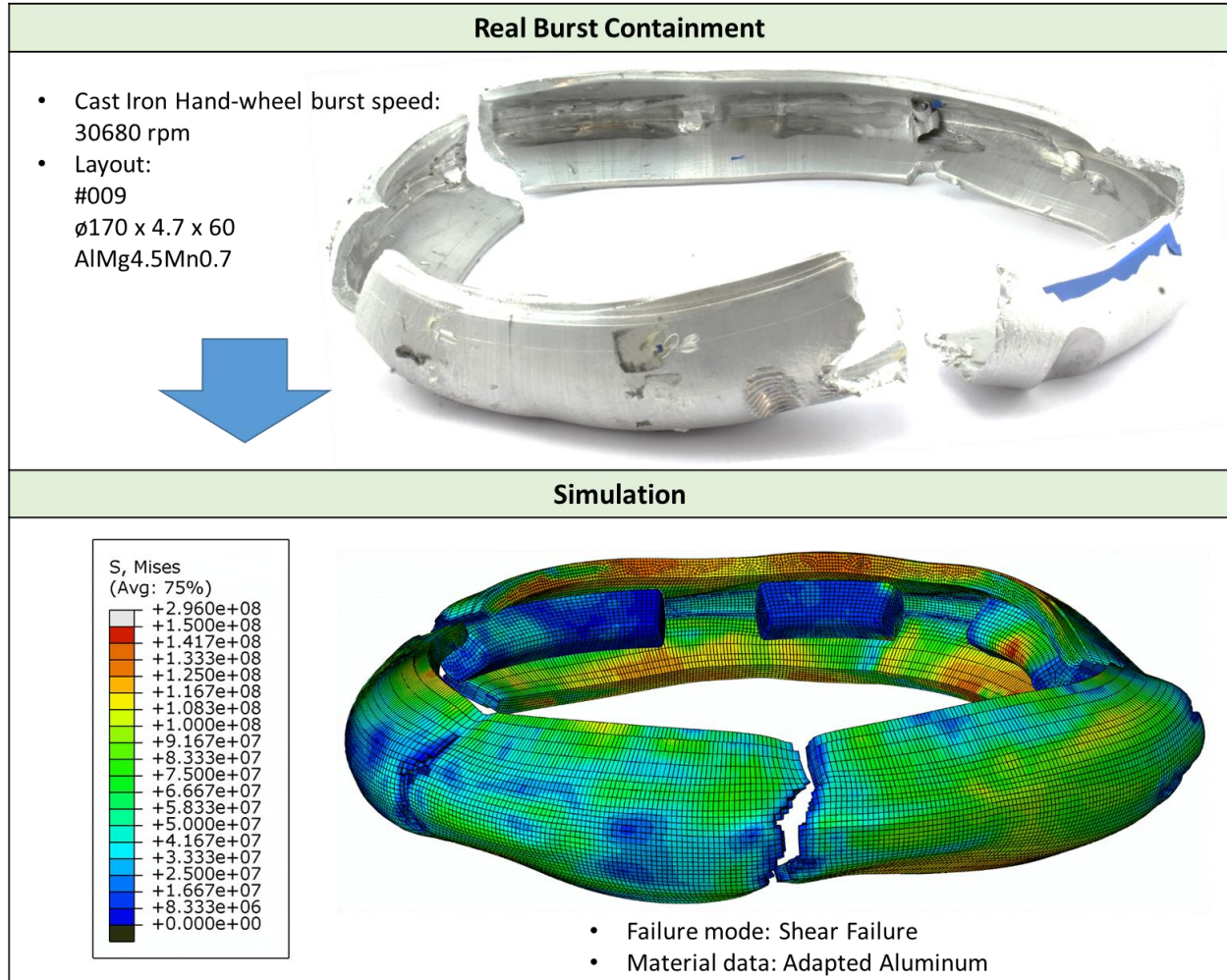


Figure 67: Reconstruction of a completely destroyed containment by implementing a shear failure

7.4 Simulation Results of the Cast Iron Handwheel Burst Behavior

Due to a great amount of generated data and observations relying on the cast iron handwheel burst behavior it was possible to parametrize an explicit numeric simulation. The target was a visualization of the occurring failure mechanism for a better understanding of the dynamic movement of the fractures and the resulting kinetic energy impact on the containment.

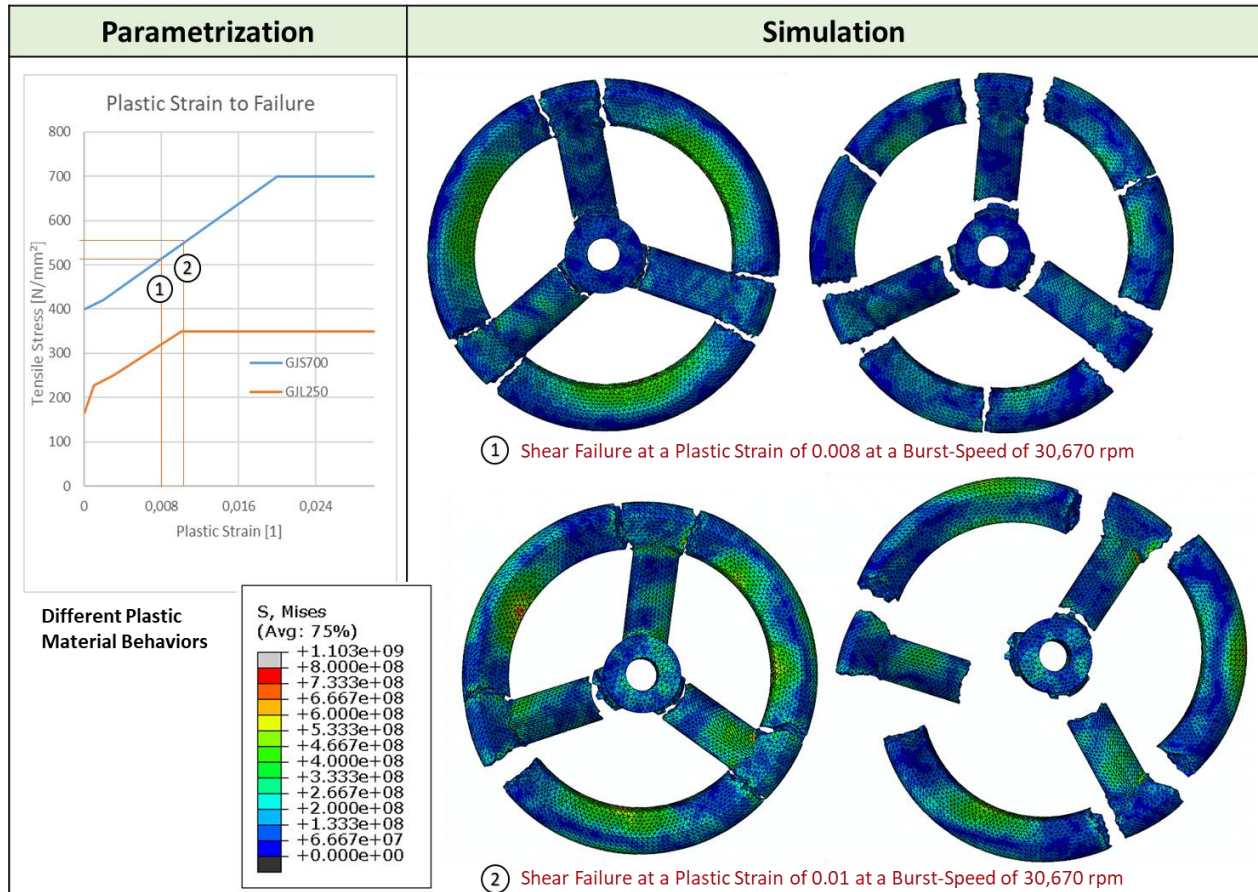


Figure 68: Simulation process of a cast iron hand wheel burst behavior (ABAQUS)

Figure 68 illustrates the simulation results acquired in *ABAQUS*. For a reproduction of the burst behavior at different burst speeds, the used material has to be identified properly. Therefore, the known material properties like the density, the young's modulus and the Poisson's ratio were defined. To obtain a failure mechanism of the meshed structure, which terminates the boundary of overstressed elements, a shear failure was implemented. In combination with an estimated plastic strain behavior of the material, the element deformation follows the elastic and plastic stress-strain curve. The programmed shear failure determines the element boundaries at a defined plastic strain.

The diagram of Figure 68 shows two attempts of plastic deformation behaviors for different cast irons and the generated results at a shear failure at a plastic strain of 0.008 and 0.01.

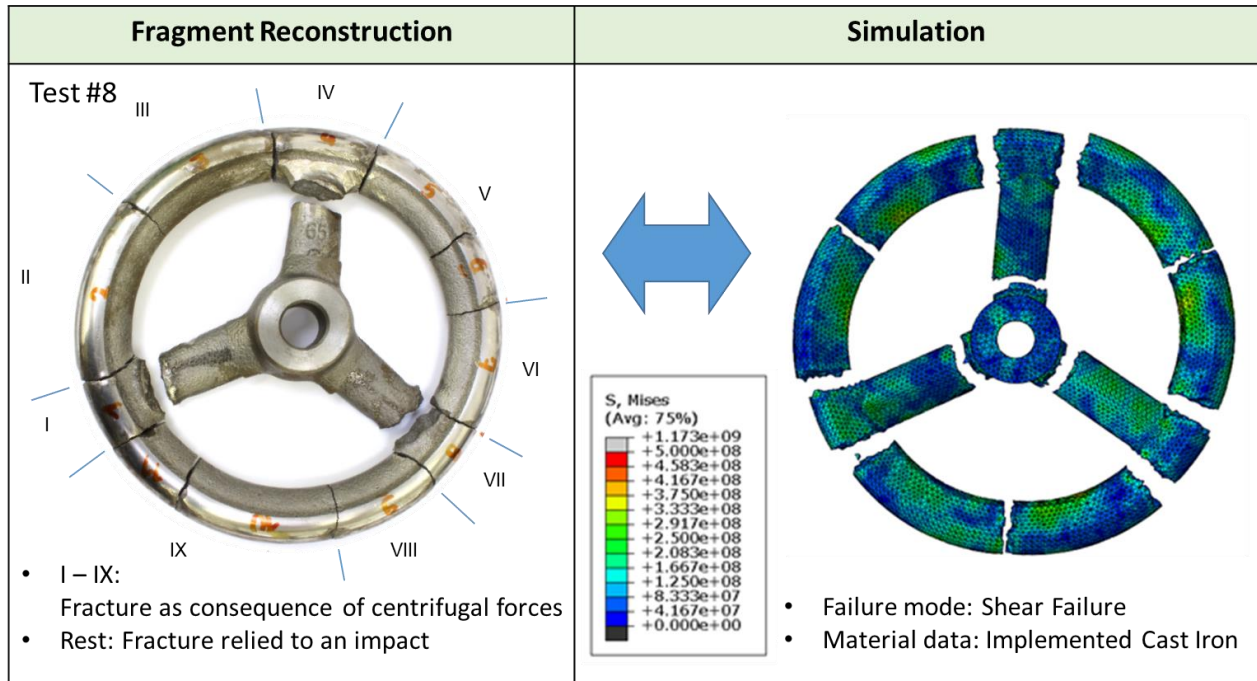


Figure 69: Result of the simulation with the plastic strain behavior of GJS 700 and a plastic strain fail at 0.008 compared to observed fragment sectors

The simulation result shown in Figure 69 illustrates the brittle material behavior of the cast iron structure at higher speeds. The examination of the hand wheel fractures, which are formed at rotation speeds up to 30,600 rpm, verified the simulated output.

After the initial burst, left and right to the spoke, a ring-segment of nearly 120° is released. Depending on the fragment size, the stored energy split up in a translation and rotation part. A 120° segment has an energy ratio (translation- to kinetic-energy) of nearly 65 percent (Figure 70). This means the remaining rotational energy is about one third of the total kinetic energy of the fragment, which is sufficient to induce a second break.

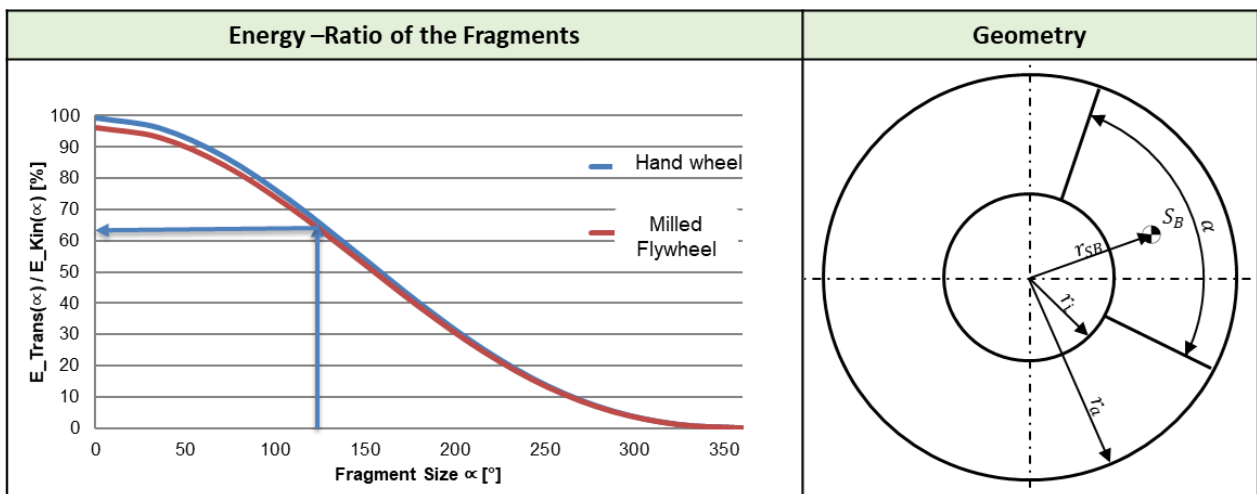



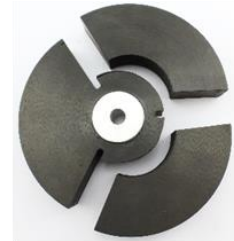
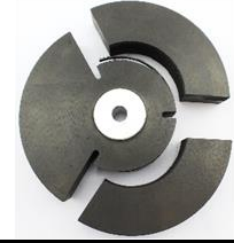

Figure 70: Energy ratio of the fragments depending on the released segment size (left), Geometry of the circular ring (right)

The further breaks of the rotor fragments occur due to the impact with the containment. The test series has shown that a thinner, more ductile housing reduces the post breakages, which seems logical as the rotor fragments experience a softer “landing” in the burst containment and hence remain intact. This constructive measure slows down the fragments and absorbs the kinetic energy by a greater deformation.

7.5 Results of the Empirical CFRP Burst Tests


Five burst tests were executed. The resulting bursting speeds of the radially notched rotors, illustrated in Table 5 and Table 6, are far below the calculated speeds. This behavior may be explained by already existing circular cracks, due to thermal residual stresses. Further observation of the rotor structures leads to the conclusion that the manufacturing process showed various issues related to filament winding and the quality of the *PrePreg* conditioning. Therefore, the estimated burst speed values are not comparable with the actual test results.

Table 5: Executed CFRP burst tests (Part 1)

No.:	Docum. Assignment:	Containment [mm]	Rotor Description [mm]	Burst-speed [rpm]	Estimated Burst-speed [rpm]	Kinetic Energy [J]	Photo
23	#01	219.1 x 20 x 56 S355 J2H	ø160 x 30 radial notched; three notches; notch ground diameter øk: 50	2453	16000	101	
24	#02		ø160 x 30 radial notched; three notches; notch ground diameter øk: 60	1435	16500	35	
25	#03		ø160 x 30 radial notched; three notches; notch ground diameter øk: 70	2064	17000	72	
26	#04		ø160 x 30 circular notched; notch diameter øk: 100; remaining bar depth t: 10	35635*	28000	21339	

* not destroyed

Table 6: Executed CFRP burst tests (Part 2)

No.:	Docum. Assignment:	Containment [mm]	Rotor Description [mm]	Burst-speed [rpm]	Estimated Burst-speed [rpm]	Kinetic Energy [J]	Photo
27	#05	219.1 x 20 x 56 S355 J2H	∅160 x 30 circular and radial notched; notch diameter ∅k: 100; remaining bar depth t: 10	20340	-	6997	

7.5.1 Results of the Radially Notched CFRP Burst Rotor

Every observed burst rotor showed already opened circular cracks, as shown in Figure 71. As illustrated, there were two visible cracks, one at a diameter of 70 mm and the other at a diameter of 118 mm. Both occurred at calculated high levels of thermal residual stresses during the manufacturing process. If the structure is properly manufactured, the matrix should withstand the occurring stress levels. However, even small inconsistencies likely cause initial failures, which can lead to an interlaminar crack propagation. The observed circular crack expansion often did not continue a full cycle of 360°. This could be explained by the assumption that an already opened interlaminar crack loses almost its entire ability to absorb radial tensile stresses. This leads to a coaxial displacement of the inner to the outer ring (separated by the crack), reducing the radial stress on the opposite side of the crack. By segmenting the circular wound composite, the interlaminar cracks are radially separated and thus prevented from further propagation. In summary, thermal cracks with different radial positions and different circular expansion could have led to the variable fragment sizes of the first test. The other two tests (#02 & #03) showed a comparable behavior with the main difference of only one visibly appearing crack. In both tests, one segment remained on the hub (Table 5). As previously mentioned, this part may not have been influenced by the occurring thermal crack and even resisted the burst impact.

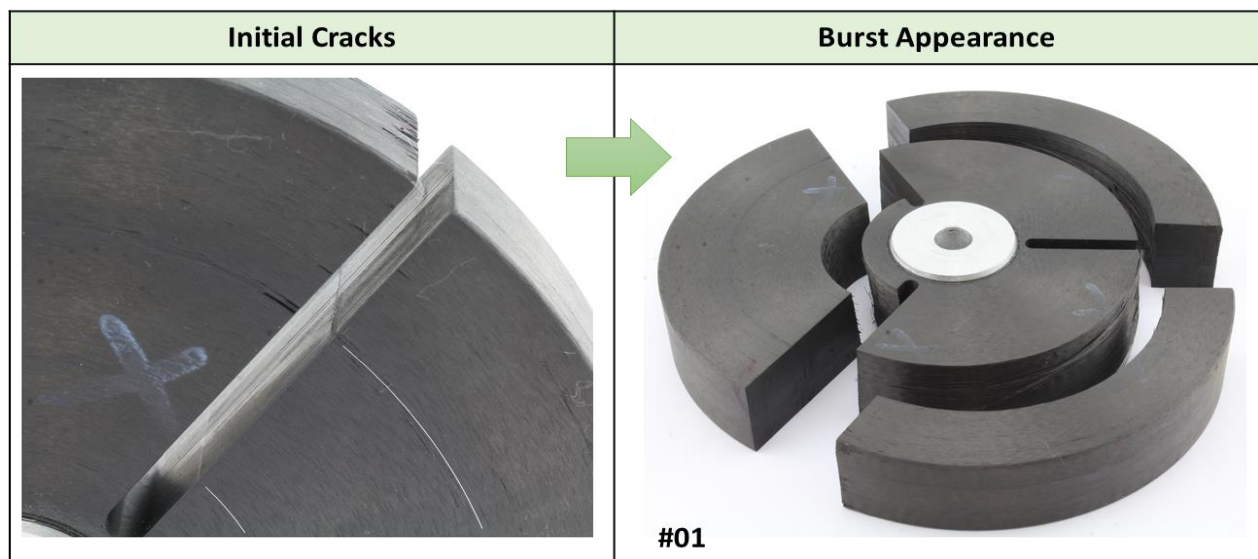


Figure 71: Thermal residual cracks (left) and the resulting burst appearance (right)

Furthermore, every fracture surface showed a certain “waviness” of the wound fiber (Figure 72).

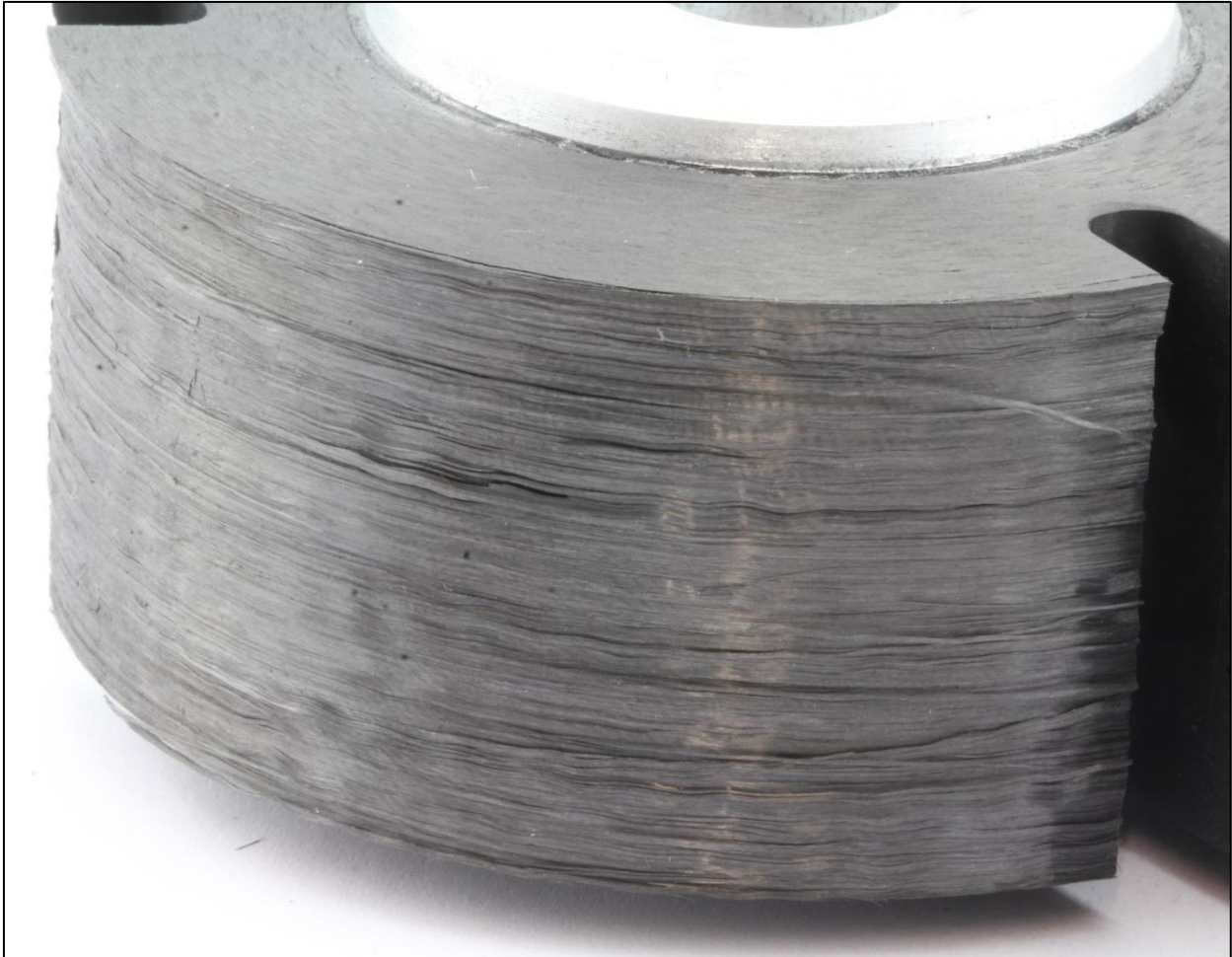


Figure 72: Close-up of the wavy carbon fiber structure (One fracture surface of the CFRP burst rotor #02)

This phenomenon of circular fiber buckling can be caused by various influences. The buckling is a possible reaction to the resulting bending stresses over the *PrePreg* thickness or the thermal residual stresses.

- **Bending:**

Observations, as illustrated in Figure 73, indicate that certain existing cracks propagate along the contact surface of the wound *PrePregs*. This assumption is based on the different appearance of corresponding fracture surfaces. The outer one shows a high degree of buckled fibers, in contrast to the inner surface without or with a lower degree of waviness. This behavior can be explained by the occurring tension situation, also demonstrated in Figure 73 on the left side. If we examine the winding process, the *PrePregs* are bent over a round surface. Due to the thickness of 0.25 mm of the band shaped unidirectional composite, the fibers near the outer surface are stretched and the inner fibers are compressed. If the pre-tension of the *PrePregs* is less than the magnitude of the compression that occurs, it is likely that the still loose fibers will buckle. It also can be determined that that the occurring magnitude of the waves depends on the radius where they appear. According to bending tensions, a small winding diameter leads to greater preloads, or in our case, to greater waviness of the fibers.

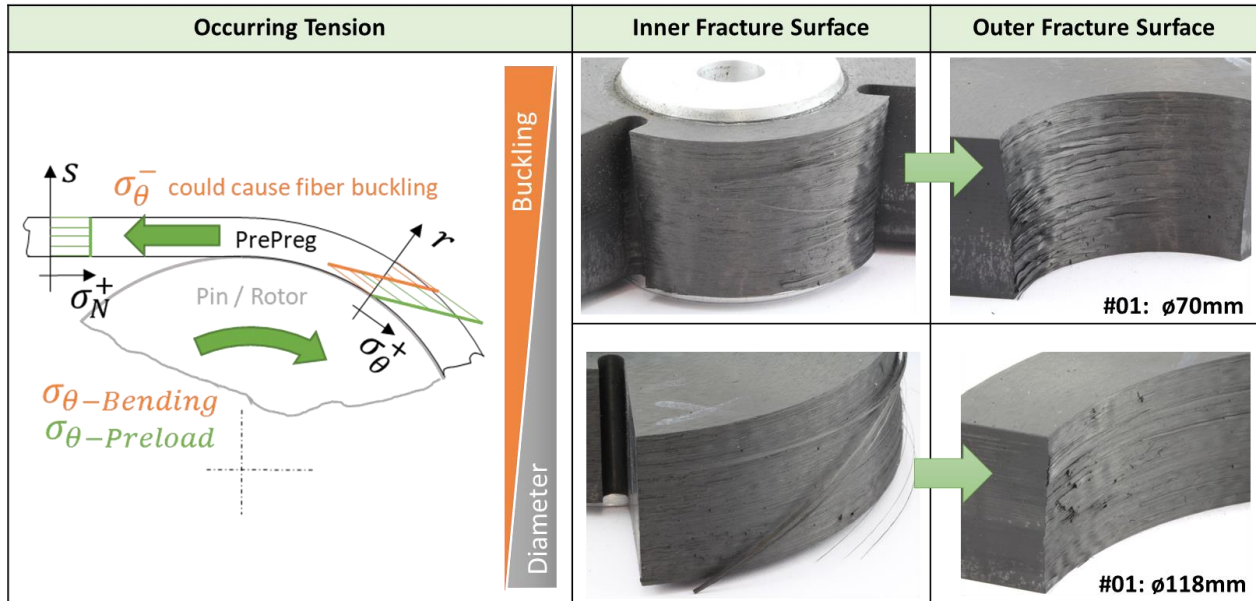


Figure 73: Schematic influence of the preload and the winding diameter on buckling appearance

According to this theory, the projected *FlyGrid* rotor with its much larger diameter will lead to lower required preloads. The winding device used records the pre-tensioning forces. We have to take into account that these monitored forces for each *PrePreg* band are important values to detect quality issues.

- **Adhesive Bonding:**

Another theory is that the adhesive bonding of the coiled *PrePregs* could also cause buckling effects. In contrast to a liquid winding process, in which the pure carbon fibers are impregnated by guiding through a dip of liquid resin, the pre-impregnated laminates have a much higher adhesive bound due to a lower viscosity of the uncured matrix material. This effect inhibits the gliding of the layer and can create additional circular pressure.

- **Thermal Residual Stresses:**

The thermal expansion of the composite in the longitudinal direction of the fiber, driven by the cooling process during the curing procedure, generates radial tensile stresses. These tensile stresses are based on a circular fiber tension in the inner rotor layers and fiber compression in the outer layers. This effect can also cause fiber buckling in the outer ring zones.

It can be assumed that the entire structure is subject to a variation of influences, which can lead to waviness of fibers. At this stage of the research, it cannot be estimated whether the observed waviness has a strong negative influence on the function of the finished flywheel rotor. This aspect results from a microscopic observation of the composite structure. In this case, the embedded corrugated fiber bundles produce an anisotropic material behavior, which reinforces the axial and/or radial composite structure by a certain σ proportion of angularly oriented fibers. In principle, this effect could have a positive impact on the overall material behavior. The downside would be an inhomogeneity which is difficult to determine and which would affect the transverse-isotropic rotor calculations.

7.5.2 Results of the Circularly Notched CFRP Burst Rotor

It was expected, that the circular notch might already lead to an interlaminar crack without adding any mechanical load. This assumption relies on the removed tensioned material, which induces higher residual tension in the remaining bar structure (explained in the Chapter 6.3.3). As shown in Figure 74, the outcome of this estimation was approved. According the manufacturer's statement, the crack occurred during the groove milling process.



Figure 74: Circular crack on the groove bottom

The executed over-speed test showed that the structure resisted centrifugal loads even at high rotational speeds of over 35,600 rpm. It was demonstrated that the highly uneven crack-surface did not affect the spinning burst-rotor. This observation is in contrast with the expectation that the outer ring would fall off and cause further unwinding delamination or a rotor crash due to a strong imbalance. It can be assumed that the generated imbalance did not show any discernible influence during test operation, because the test rig layout allows operation at high degrees of rotor imbalance.

The only additional damage of the rotor was a small release of material at the outer circumference, as illustrated in Figure 75. Due to the final turning process, some of the outer fiber bundles were cut. In combination with a slightly radial waved structure, this may have led to a composite separation. If the mass of the separated material is great enough and/or the conditioning of the *PrePregs* is not appropriate, it can cause a partial delamination of material from the outer rotor surface.



Figure 75: Rotor damage due to released circumferential material (left) and remaining debris after the test (right)

In terms of the further manufactured *FlyGrid* rotor, such composite inconsistencies have to be avoided, especially because even higher circumferential speeds occur and possible imbalances can cause much greater damage.

7.5.3 Results of the Circularly and Radially Notched CFRP Burst Rotor

Figure 76 illustrates the test results. It shows that only three partial segments were released. This behavior was the result of another circular crack near the outer circumference. Compared to the previous burst rotors, the generated fragments show a much greater degree of disintegration, caused by higher tangential speeds, which exceeded 170 m/s.

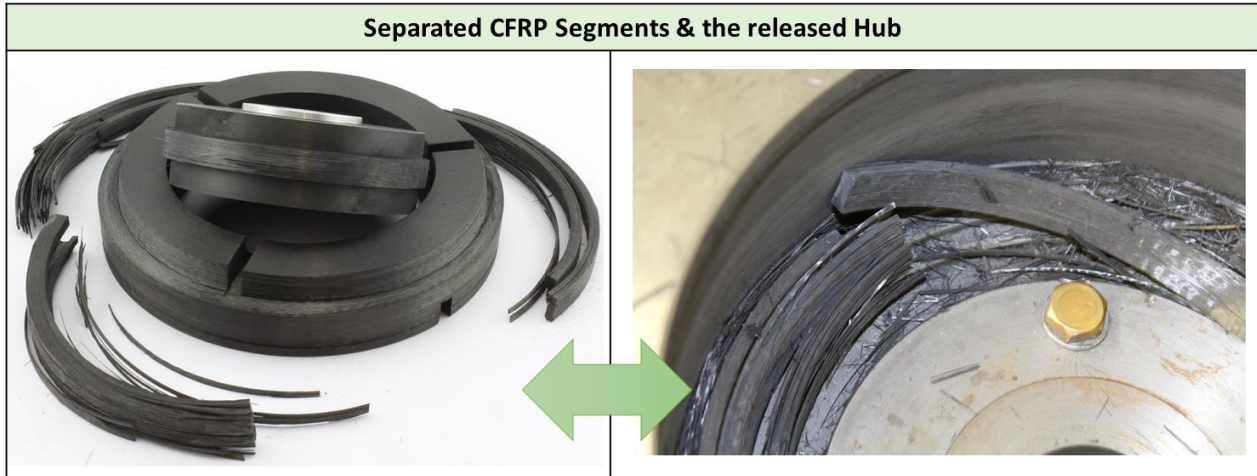


Figure 76: Destroyed rotor structure (left), and the remaining fragments in the burst chamber (right)

One theory is that the estimated post-fractures, caused by a containment impact, are based on disintegrated chemical boundaries of the carbon fiber composite. This fracture occurrence can be classified by the underlying failure mode. Detailed observations showed that the segment structures were mainly delaminated by interlaminar crack propagation circularly as well as horizontally orientated. The created split fiber bundles can hardly absorb bending loads, which could lead to increased breakage of fibers. As advantage of this behavior can be mentioned, that every created fracture surface needs a certain amount of energy, which reduces the impact force on the containment. On the other hand, both of these failure modes force a particle contamination of the burst chamber and can generate an axial deviated particle stream, which cause additional pressure on the top and bottom surfaces of the housing.

Furthermore, the crack within the circular notch (Figure 77) was completely opened after the test. Due to a remaining tangential fiber connection and a slightly conical shape of the crack surfaces (with an upwards decreasing diameter), the outer ring held its place during the burst test.

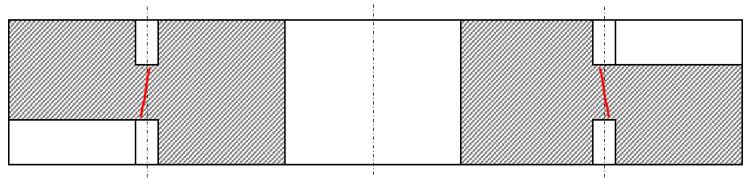


Figure 77: Conical shape of the fracture surface (red)

Based on these observations, an initial crack has to be strictly avoided, to prevent further crack opening processes during the flywheel operation.

8 Summary and Outlook

This thesis presents a strategy for an empirical and simulative investigation of rotor burst and containment behavior with respect to high-speed Flywheel Energy Storage Systems (FESS). The target was to generate experiences in order to design safer, lighter and cheaper housing.

Different analytical impact models, related to composite rotor bursts, enable an initial design of the safety containment. However, these existing and established models do not provide any information about the underlying research and the required input values. This unpublished knowledge forces further efforts to gain more experience in the field of empirical over-speed testing of Carbon Fiber Reinforced Polymer (CFRP) rotors.

Within this work, empirical observations of steel rotor bursts were made to describe the ductile containment deformation to absorb the released kinetic energy. Further test series provided the validation of implemented failure modes and material data for numeric analysis. With this simulation, suitable safety layouts for the intended *FlyGrid* prototype of a stationary fast rotating FESS are to be created. By using a wound carbon fiber rotor, the manufacturing related composite structure was further tested. This was realized by especially notched flywheel designs that provided failure occurrences within the restrictions of the used burst test rig. These observations identified various manufacturing process related issues, which will need to be eliminated in terms of the planned *FlyGrid* prototype.

In order to specify the carbon fiber composite used for the *FlyGrid* rotor more precisely, the material parameters are determined empirically. Ring and flat tensile specimens, which contain the geometries and manufacturing processes of the planned rotor, serve for this purpose. The samples are used to determine the directionally depending young's modulus and the tensile strengths. These parameters are required for the analytical and simulative layouts and limits of the rotor.

For findings regarding the rotor burst behavior of unweakened CFRP rotor structures and the resulting impact forces on the safety housing a new burst test rig as development tool would have to be built. A new layout will be needed because of the already reached system limitations of the existing test rig. Such implementation of carbon fiber rotor burst tests during the development and test phase of the *FlyGrid* prototype could lead to highly relevant observations for a better understanding of the failure behavior and safety of modern flywheel energy storage systems.

9 Bibliography

- [1] A. Buchroithner, P. Haidl, C. Birgel, T. Zarl, H. Wegleitner, „Design and Experimental Evaluation of a Low-Cost Test Rig for Flywheel Energy Storage Burst Containment Investigation,“ *MDPI Applied Sciences*, p. 1, 30 10 2018.
- [2] A. Buchroithner, H. Wegleiter, B. Schweighofer, „Flywheel Energy Storage Systems Compared to Competing Technologies for Grid Load Mitigation in EV Fast-Charging Applications,“ in *27th International Symposium on Industrial Electronics (ISIE)*, Cairns, Australia, 12–15 June 2018.
- [3] T. Mento und B. Ruth, „Injuries Reported in Explosion at Poway Business; KPBS public broadcasting,“ 10 June 2015. [Online]. Available: <https://www.kpbs.org/news/2015/jun/10/explosion-quantum-energy-poway/>. [Zugriff am 19 November 07].
- [4] S. Burgholzer, *Entwicklung und Inbetriebnahme eines Prüfstandes für die versuchsgestützte Untersuchung von Flywheel-Berstgehäusen*, Graz: Technische Universität, 2014.
- [5] T. Atzlinger, „Konstruktion eines Ersatzprüfkörpers, der das Bersten einer Vollscheibe aus isotropem Material repräsentativ und reproduzierbar nachbildet,“ Technische Universität Graz, Graz, 2014.
- [6] M. Jungreithmair, „Konzeption und Konstruktion von Berstschutzgehäusen für Schwungscheiben aus isotropem Material,“ Technische Universität Graz, Graz, 2013.
- [7] N. Mind, *The Mechanical Battery*, 2019.
- [8] H. Schürmann, *Konstruieren mit Fase-Kunststoff-Verbunden*, Darmstadt: Springer, 2007.
- [9] T. Kampf, *High Speed Flywheel Design*, Universität Uppsala, 2012.
- [10] M. Strasik, P. E. Johnson, A. C. Day, J. Middleider, M. D. Higgins, J. Edwards, J. R. Schindler, K. E. McCrary, C.R. Mclver, D. Carlson, J. F. Gonder, and J. R. Hull, *Design, Fabrication, and Test of a 5-kWh/100-kW Flywheel Energy Storage Utilizing a High-Temperature Superconducting Bearing*, UK: University of Cambridge, 2007.
- [11] B. Peter, *Schnelldrehendes Schwungrad aus faserverstärktem Kunststoff*, Zürich: ETH, 1996.
- [12] J. Lenza, B.R.K. Blackmana, A.C. Taylora, R. Morganb, C. Crua, *SELECTION OF TEST METHODS TO EXAMINE THE FRACTURE MECHANICS OF CARBON FIBRE COMPOSITE FLYWHEELS*, 2014.
- [13] F. Täubner, „Schwungradspeicher in Vision und Realität,“ Derenburg, Deutschland, 2016.
- [14] EAST-4D GMBH LIGHTWEIGHT STRUCTURES, „Safe and high cycle recharging electromechanical battery, EU-Projekt, Grant agreement ID: ERK6-CT-1999-35003,“ Chemnitz, Germany, 1999.
- [15] R. F. Grisworld, E. S. Zorzi, „Energy-Absorbing Housing for High-Speed Flywheels,“ Pheonix, Ballston, US, 2004.

- [16] F. Strössenreuther, *Machbarkeitsstudie und Konzept einer stationären Schwungradanlage zur dezentralen, verbraucherorientierten Energiespeicherung*, Diplomarbeit: Rheinisch-Westfälische Technische Hochschule Aachen, 1996.
- [17] G. Genta, *Kinetic Energy Storage Theory and practice of advanced flywheel systems*, Butterwoths, 1985.
- [18] K. Grote, J. Feldhusen, *Dubbel - Taschenbuch für Maschinenbau*, Springer, 2007.
- [19] Alexander Wiegant SE & Co.KG, „WIKA Bourden Tube Pressure Gauge,“ [Online]. Available: https://en.wika.com/landingpage_bourdon_tube_pressure_gauge_en_co.WIKA. [Zugriff am 29 November 2019].
- [20] Elsevier B.V., „Science Direct / Capacitive Accelerometer,“ [Online]. Available: <https://www.sciencedirect.com/topics/engineering/capacitive-accelerometer>. [Zugriff am 29 November 2019].
- [21] Elsevier B.V., „ScienceDirect, Brinell Hardness,“ [Online]. Available: <https://www.sciencedirect.com/topics/engineering/brinell-hardness>. [Zugriff am 10 11 2019].
- [22] Robosop.com, „CZL635, Datasheet - 3135 - Micro Load Cell (0-50kg),“ 13 May 2011. [Online]. Available: <https://www.robotshop.com/media/files/pdf/datasheet-3135.pdf>. [Zugriff am 30 November 2019].
- [23] Phidgets Inc., „Phidgets / Buttom Load Cells,“ 27 November 2018. [Online]. Available: https://www.phidgets.com/docs/Load_Cell_Primer#How_they_work. [Zugriff am 30 November 2019].
- [24] E. Schrüfer, L. Reindl, B. Zagar, *Elektrische Messtechnik - Messung elektrischer und nichtelektrischer Größen*, München: Carl Halser Verlag, 2014.
- [25] A. J. Colozza, „High Energy Flywheel Containment Evaluation,“ NASA: Brook park, OH,USA, 2000.
- [26] D. W. J. Mohanraj Murugesan, „Johnson Cook Material and Failure Model Parameters Estimation of AISI-1045 Medium Carbon Steel for Metal Forming Applications,“ MDPI, Jeju National University, Jeju-Do 63243, Korea, 2018.
- [27] Dassault Systemes, *Simulation of the ballistic perforation of aluminum plates with Abaqus/Explicit*. D. Systemes, Hrsg.
- [28] K. N. Singh, R. Clos, U. Schreppel, P. Veit, A. Hamann, D. Klingbeil, R. Sievert, G. Künecke, „Versagenssimulation dynamisch belasteter Proben mit unterschiedlichen Mehrachsigekeitszuständen unter Verwendung des Johnson-Cook-Versagensmodells für eine Nickelbasislegierung,“ *Technische Mechanik*, Bd. 23, 2003.
- [29] K. Senthil, „Procedia Engineering 173“.
- [30] Acumen, *Charpy Impact tutorial - Johnson-cook material + Damage*.

[31] R. Gilbert, *Flywheel Drive Systems Study Final Report*, Research Thesis: Lockheed Missiles and Space Company, 1972.

[32] Research Councils UK/Innovate, „FlySafe—Flywheel-Hybrid Safety Engineering,“ United Kingdom.